PREPARATION AND CHARACTERIZATION OF SURFACE FUNCTIONALIZED BORON NANOPARTICLES FOR FUEL AND PROPELLANT APPLICATIONS

by

Jesus Paulo L. Perez

A dissertation submitted to the faculty of
The University of Utah
in partial fulfillment of the requirements for the degree of

Doctor of Philosophy

Department of Chemistry

The University of Utah

December 2013

The University of Utah Graduate School

STATEMENT OF DISSERTATION APPROVAL

The dissertation of **Jesus Paulo L. Perez**

has been approved by the following supervisory committee members:

Scott L. Anderson	, Chair	**04/24/2013** Date Approved
Jennifer Shumaker-Parry	, Member	**04/24/2013** Date Approved
Marc D. Porter	, Member	**04/24/2013** Date Approved
Charles A. Wight	, Member	**04/24/2013** Date Approved
Wlodzimierz W. Zmierczak	, Member	**04/24/2013** Date Approved

and by **Cynthia J. Burrows**, Chair of

the Department of **Chemistry**

and by David B. Kieda, Dean of The Graduate School.

ABSTRACT

Boron's energy potential as a combustion fuel can be harnessed by using nanosize solid particulates. In this study, functionalized boron nanoparticles were produced through high-yield ball milling techniques. The organic surface coating protected oxide-free boron nanoparticles from air oxidation and at the same time promoted dispersion in polar and nonpolar liquid fuels. For dispersion in hydrophobic fuels, oleic acid was used as ligand, and its interaction with boron nanoparticles was studied using XPS, FTIR, ^{13}C-NMR and TGA. Results show that oleate species bonded to boron nanoparticles through a bridging bidentate interaction. Furthermore, undissociated oleic acid molecules persisted on the surface which may be anchored through intercalation with covalently bonded oleate species.

Hydrogenation of boron through H_2 gas milling provides an alternative pathway of increasing ignitability and specific impulse of boron nanoparticles. It was also used to alkylate boron nanoparticles for dispersion in liquid hydrocarbon fuels. Boron nanoparticles were also milled with hypergolic ionic liquids to increase their energy density. Spectroscopic experiments that probed interactions of boron with 1-methyl-4-amino-1,2,4-triazolium dicyanamide([MAT][DCA]) and 1-butyl-3-methyl-imidazolium dicyanamide([BMIM][DCA]) suggest that a possible B–N binding exist between the amino substituent of [MAT][DCA] and the dicyanamide anion of both ILs.

TABLE OF CONTENTS

ACKNOWLEDGMENTS

There are several people that should go into this list. People who have touched my life, and have been part of it even for a moment. Somehow, I believe they have molded me into what I am today, got me to where I am, and will guide to where I still have to go. However, there are specific individuals that I would like to acknowledge for their great contribution in making this dissertation possible and my doctorate a reality:

My professor, Scott Law Anderson, for giving me the opportunity to work in his laboratory, and providing me the guidance throughout my graduate career. I treasure all those energetic discussions especially during those times when we revise our papers or when a presentation or a symposium is nearing.

The whole Anderson research group, past and present members whom I had the chance to work with. They have provided a hospitable atmosphere that makes working in the lab less punishing, especially if the instrument does not cooperate.

Our research collaborators, the University of Alabama and the Air Force Office for Scientific Research (AFSOR), for working with us and sharing their expertise in the ionic liquid research.

My friends here in Salt Lake City, especially my two roommates, for bringing the homely environment of our foreign country, the Philippines, whenever we go out for a Friday dinner or out hiking in the mountains.

My family back home. My mom and my dad, they give me strength, and my brother and my sister, they give me inspiration and the will to pursue my dreams. This one's for them.

And finally, my Creator. Every single one of us has a purpose and a place in this ever expanding universe. I believe I now found mine. Thank You.

CHAPTER 1

INTRODUCTION

High-energy additives have been studied for use in commercial fuels such as diesel and gasoline in order to increase the heat of combustion of these fuels.[1-3] Various research focuses on metals such as Li, Mg, Al, and B, and their compounds and alloys because of their increased reactivity with oxygen, and more significantly their highly exothermic combustion.[4] Metalized fuel slurries (homogenized mixtures of metal or alloy powders and liquid fuels) were studied to gain insights on the ignition and energetic properties of such materials.[5-6] Boron in particular is highly attractive for fuel applications because of its high heat of combustion – both volumetric and gravimetric (137.8 kJ/mL; 59.0 kJ/g).[7] Its gravimetric energy density is higher than most combustible materials and fuels, with the exception of Be and H_2.[7] The toxicity of Be and its combustion products poses significant hazards on handling and storage, making them unfavorable for fuel applications. On the other hand, liquid hydrogen, although popularly used as fuel in large rockets and space shuttle missions, is hindered by its extremely low volumetric heat of combustion (8.6 kJ/mL),[7-8] which is not practical for volume-limited high-speed systems.

Research of boronated fuels began in the 1950s when the U.S. military was actively searching for high energy fuels for their rocket development programs.[9] Popularly known as "zip fuels," these fuels are proprietary mixtures of liquid hydrocarbon jet fuels and micron-sized elemental boron powders or boron compounds designed to provide greater range, speed, and payload capacity to jet planes and air-breathing missiles.[10] Theoretical and experimental studies conducted by Peleg[11-12] on mixtures of boron in kerosene (up to 70 wt%), indeed showed an increase in volumetric specific impulse of the mixture as compared to pure kerosene when burned in a dump combustor. Other studies involved the use of metallic boron as solid fuel in hybrid propellants.[4,13-14] For this application, powdered boron was mixed with a polymeric binder, usually hydroxy-terminated polybutadiene (HTPB), and then molded into

the walls of the combustion chamber. In hybrid propellant systems gaseous or liquid oxidizers were used to enhance ignition of the solid state fuel. Despite these advances, harnessing the full energy potential of elemental boron through combustion still proved to be challenging. Part of the difficulty is due to boron's high melting and vaporization temperatures (2200 °C and 3900 °C, respectively),[8] which make it difficult to atomize in a spray combustion system. Furthermore, unoxidized boron particles react immediately with oxygen when exposed to air, producing a refractory boron oxide (B_2O_3) layer on the surface. When this occurs, particle combustion becomes a slow process of heterogeneous surface reactions between boron[15] and oxygen[16] atoms diffusing through the oxide layer. Once a significantly thick layer is formed, diffusion becomes energetically hindered and further oxidation/combustion of the boron-rich core is terminated. Nevertheless, ignition and continuous combustion of a particle can still be achieved at suitable conditions (i.e., at temperatures of 1600 – 1700 °C, when the oxide starts to vaporize), as suggested by experiments conducted by Macek et al.[17] on single boron particles 35 – 44 μm in diameter. Unfortunately, combustion engines of jet and rocket systems do not always reach such conditions. As a consequence, unburned boron fuel and unwanted sludge buildup are often observed in turbines.[18-20] To mitigate this problem, sophisticated engine designs were developed improving the introduction of oxidizers and extending residence times of solid boron particles in the combustion chamber, thereby enhancing the interaction of boron with the oxidizer in the combustion process.[21] Even though a number of these prototype engines noted significant increase in the heat of combustion with the use of boron-containing fuels, only a few were used in actual operation.

Another approach that could be explored to increase the efficiency of boron combustion is nanosizing of microparticulate boron fuels. Ignition and flame propagation of nanothermites at this size regime have been observed to increase considerably in orders of

magnitude beyond the theoretical "d-square law" where the burning rate, as measured through the mass-loss rate, shows that the square of the particle diameter decreases linearly with time during combustion.[22-23] The significant increase of low-coordinated surface atoms that are available for instantaneous oxidation contributes to the increased rate. Realizing the potential of nanosized metal additives, a number of studies focused on the preparation of energetic metal nanoparticles such as aluminum,[24] magnesium,[25] titanium,[26] and boron.[27-29] This gave rise to currently established methods of metal nanoparticle synthesis including solution phase reduction methods,[30] pulsed laser ablation,[31] sonoelectrochemistry,[25] and pyrolysis techniques.[28] Since these metals are highly reactive with air, it is desirable that the resulting nanoparticles are protected or passivated to prevent unwanted oxidation that may result in accidents in the laboratory. Also, surface oxidation of very small particles will convert a substantial portion of energetic material into unreactive oxide, thus lowering the energy content of the particles.

This dissertation presents work on the synthesis of oxide-free boron nanoparticles that were capped with organic ligands through the use of ball milling technique. The ligands acted as protective coating against air oxidation and also promoted dispersibility of boron nanoparticles in either polar or nonpolar liquid fuels.

Chapter 2 discusses characterization of oleic acid molecules bonded to the surface of boron nanoparticles. Previous studies done by our group have already established the capability of oleic acid molecules to protect boron nanoparticles from air oxidation and to allow stable suspensions in nonpolar hydrocarbon fuels such as hexane and JP-5.[32-33] In this chapter, we provide more detailed studies on the nature of the chemical bond between surface boron atoms and oleic acid through a series of spectroscopic experiments. In addition, a new approach on coating boron nanoparticles with aliphatic hydrocarbons is also presented.

Boron powder feedstocks were milled with hydrogen gas to form H-terminated boron surfaces. This B–H bond is expected to be as reactive as other borane and borohydride compounds with respect to alkenes.[34] The reaction would produce alkylated boron nanoparticles without the use of reactive functional groups such as carboxylic acids, amines, and thiols. This procedure may prove useful in introducing organic ligands that are not inherently reactive with unoxidized boron.

Chapter 3 presents studies on the binding of boron nanoparticles with ionic liquids (ILs). ILs are salts with low melting temperatures (generally less than 100 °C) which have found a number of applications in different fields due to their unique solvating properties, electrical conductivity, wide liquid range, and low vapor pressures.[35-37] In recent years, the discovery and development of ILs with *hypergolic* properties introduced the possibility of using them as hydrazine substitute and safer rocket propellants.[38-42] Hypergolicity pertains to a fuel's distinct property of spontaneously igniting and combusting once in contact with a strong oxidizing agent (i.e., white fuming nitric acid, perchloric acid, and hydrogen peroxide), and the ignition delay after contact of fuel and oxidizer characterizes an important property of liquid propellants. In the preparation of these hypergolic ILs, imidazolium cations were initially selected because of their stability in air while dicyanamide was chosen as the anion to reduce the IL viscosity,[43-44] an important factor for liquid propellants. A variety of substituents on the imidazolium cation were also examined for their effects on hypergolic ignition delays, but it was later determined that reaction of the dicyanamide anion with the oxidizer had a dominant effect on the ILs' hypergolic ignition.[38,45] Furthermore, dicyanamide-based ILs were also found to ignite faster than other ILs with the same imidazolium cation but a different anion such as nitrocyanamide and dinitramide. Still, measured ignition delays for the imidazolium dicyanamide ILs were longer (15 ms for 1-propargyl-3-methylimidazolium

dicyanamide) than hydrazine's (5 ms under similar conditions).[41] To improve ignition delay, Zhang[46] studied a new class of ILs composed of strongly reducing anions such as borohydride and dicyanoborate. Unfortunately, these ILs possess low gravimetric density which results in lower impulse delivered per volume of propellant used. [43]

Shreeve et al. studied ILs composed of multiple nitrogen atoms.[44,47-53] Calculations of these ILs' condensed phase standard heat of formation ($\Delta H°_f$), showed that 5-membered heterocyclic structures with more nitrogen–nitrogen bonds possess higher $\Delta H°_f$[54] ($\Delta H°_f$ has been shown to be an important thermodynamic parameter in determining the energy content of heterocyclic molecules).[55-58] Addition of substituent groups was determined to have either a positive or negative effect depending on the chemical nature of the group and the atom it is bonded to. For example, an azido or amino group resulted in increased heat of formation, with the amino group contributing more when it is bonded to ring nitrogen atoms rather than to carbon atoms. In contrast, methyl, ethyl, and nitro groups were found to decrease the heat of formation.[54] In a different set of calculations, Gao[59] studied counter anions paired with 1,2,4-triazolium derivatives, particularly on known energetic inorganic anions such as dicyanamide, dinitramide, perchlorate, and nitrate. Again, it was determined that the dicyanamide anion gave the most positive $\Delta H°_f$. All these studies therefore suggested that substituted triazolium dicyanamide ILs are the best candidate for propellant applications.

The Air Force Research Lab (AFRL) has demonstrated hypergolic ignition of triazolium dicyanamide ILs, including 1-methyl-4-amino-1,2,4-triazolium dicyanamide ([MAT][DCA]) and 1-butyl-3-methylimidazolium dicyanamide ([BMIM][DCA]).[39,41] Several groups also studied azolium azolate salts, where both cation and anion are composed of heterocyclic organic ions.[60-64] Although hypergolicity is yet to be observed on these ILs, their high thermal stability makes them promising candidates for propellant applications.

Chapter 3 discusses studies on boron nanoparticles that were milled and dispersed in the ILs, [MAT][DCA] and [BMIM][DCA], to increase energy density. The interactions of these hypergolic ILs with boron nanoparticles were investigated using *ab initio* calculations, gravimetric analysis, and spectroscopic techniques, which has never been done before. Results show that both ILs can passivate boron nanoparticles through binding with the amino substituent in [MAT][DCA] and with the dicyanamide anion in [BMIM][DCA]. Calculation of the relative thickness of the IL layers from TGA and XPS data showed that there is a thicker layer of [MAT][DCA] than [BMIM][DCA] on the boron surface supporting the hypothesis that [MAT][DCA] interacts stronger than [BMIM][DCA], thus resulting in better passivation of boron nanoparticles. This is the first time that hypergolic ionic liquids were utilized and studied as passivating ligands for boron nanoparticles.

Chapter 4 presents a more detailed study on the hydrogenation of boron nanoparticles by dry milling with H_2. Hydrogenation was initially utilized as a step to bind alkenes on the surfaces of boron nanoparticles (see Chapter 2). In Chapter 4, the mechanism of hydrogen binding and desorption was probed through a series of mass spectroscopy, thermogravimetry analysis, infrared spectroscopy, and isotope labelling. Hydrogen itself is an energy dense fuel with high specific impulse. Incorporation of hydrogen either as trapped H_2 or as "surface boranes" may improve the combustibility and specific impulse of boron nanoparticles. Furthermore, boron nanoparticles loaded with hydrogen that can be stably contained within its structures is interesting for hydrogen storage applications.

1.1 References

(1) Mulic, R. Manufacture and Use of Methyl Esters of Fatty Acids, Glycerol, and Lecithin. *Tehnika (Belgrade)* **1997,** *52*, 174-176.

(2) Orr, W. C. *Substitute Fuels and Propellants with Enhanced Vapor Phase Combustion Containing Cyclopentadienylmanganese Tricarbonyl and Additives.* U.S. Patent 2003252892, Nov 20, **2003.**

(3) Zaweski, E. F.; Niebylski, L. M. *Fuel Compositions.* A 1985-793624 4623363, Nov 18, **1986.**

(4) Risha, G. A.; Evans, B. J.; Boyer, E.; Kuo, K. K. Metals, Energetic Additives, and Special Binders Used in Solid Fuels for Hybrid Rockets. *Prog. Astronaut. Aeronaut.* **2007,** *218*, 413-456.

(5) Beloni, E.; Hoffmann, V. K.; Dreizin, E. L. Combustion of Decane-Based Slurries with Metallic Fuel Additives. *J. Propul. Power* **2008,** *24*, 1403-1411.

(6) Liehmann, W. *Combustion of Boron-Based Slurries in a Ramburner*, International Annual Conference of ICT, Pfinztal, Germany, 1991; pp 97/1-97/8.

(7) Cox, J. D.; Wagman, D. D.; Medvedev, V. A. *Codata Key Values for Thermodynamics.* Hemisphere Publishing Corp: New York, 1984.

(8) Linstrom, P. J.; Mallard, W. G. *Nist Chemistry Webbook, Nist Standard Reference Database Number 69*. National Institute of Standards and Technology: Gaithersburg MD, 20899, 2011.

(9) Cracknell, J. R., High-Energy Fuels. *Flight International* March 15, 1956, pp 332-334.

(10) Griswold, W. S., *Popular Science* 1957, pp 86-89.

(11) Peleg, I.; Timnat, Y. M. Investigation of Slurry Fuel Performance for Use in Ramjet Propulsors. *Israel J. Technol.* **1982,** *20*, 206-2013.

(12) Peleg, I.; Timnat, Y. M. *Combustion of Aluminum and Boron Slurry Fuels in a Dump Combustor.* Symposium (International) on Combustion, 1982; Vol. 19, pp 557-563.

(13) Kuo, K. K.; Risha, G. A.; Evans, B. J.; Boyer, E. *Potential Usage of Energetic Nano-Sized Powders for Combustion and Rocket Propulsion*, Mat. Res. Soc. Symp. Proc., 2003; pp AA1.1.1-AA1.1.12.

(14) Risha, G. A.; Boyer, E.; Evans, B.; Kuo, K. K.; Malek, R. *Characterization of Nano-Sized Particles for Propulsion Applications.* Mat. Res. Soc. Symp. Proc. **2003,** *800*, 243-254.

(15) Glassman, I.; Williams, F. A.; Antaki, P. *A Physical and Chemical Interpretation of Boron Particle Combustion*, 20th Symposium (International) on Combustion, The Combustion Institute: Pittsburgh, 1984; pp 2057-2064.

(16) King, M. K. Boron Particle Ignition in Hot Gas Streams. *Combust. Sci. Technol.* **1986,** *8*, 255-273.

(17) Mačeik, A.; Semple, J. M. Combustion of Boron Particles at Atmospheric Pressure. *Combust. Sci. Technol.* **1969,** *1*, 181-189.

(18) Besser, H. L.; Strecker, R. *Overview of Boron Ducted Rocket Development During the Last Two Decades. Combustion of Boron-Based Solid Propellants and Solid Fuels*, Kuo, K. K., Ed. CRC Press: Boca Raton, 1993.

(19) Natan, B.; Gany, A. Combustion Characteristics of a Boron-Fueled Solid Fuel Ramjet with Aft-Burner. *J. Propul. Power* **1993,** *9*, 694-701.

(20) Natan, B.; Gany, A. Effects of Bypass Air on Boron Combustion in Solid Fuel Ramjets. *J. Propul. Power* **1993,** *9*, 155-157.

(21) Vigot, C.; Cochet, A.; Guin, C. *Combustion Behavior of Boron-Based Solid Propellants in a Ducted Rocket. Combustion of Boron-Based Solid Propellants and Solid Fuels*, Kuo, K. K., Ed. CRC Press: Boca Raton, 1993.

(22) Plantier, K. B.; Pantoya, M. L.; Gash, A. E. Combustion Wave Speeds of Nanocomposite Al/Fe_2O_3: The Effects of Fe_2O_3 Particle Synthesis Technique *Combust. Flame* **2005,** *140*, 299-309.

(23) Bockmon, B. S.; Pantoya, M. L.; Son, S. F.; Asay, B. W.; Mang, J. T. Combustion Velocities and Propagation Mechanisms of Metastable Interstitial Composites. *J. Appl. Phys.* **2005,** *98*, 064903.

(24) Chandra, S.; Kumar, A.; Tomar, P. K. Synthesis of Al Nanoparticles: Transmission Electron Microscopy, Thermal and Spectral Studies. *Spectrochim. Acta, Part A* **2012,** *92*, 392-397.

(25) Haas, I.; Gedanken, A. Synthesis of Metallic Magnesium Nanoparticles by Sonoelectrochemistry. *Chemical Communications (Cambridge)* **2008**, 1795-1797.

(26) Axelbaum, R. L.; Defaux, D. P.; Frey, C. A.; Sastry, S. M. L. A Flame Process for Synthesis of Unagglomerated, Low-Oxygen Nanoparticles: Application to Ti and TiB_2. *Metall. Mater. Trans. B* **1997,** *28B*, 1199-1211.

(27) Pickering, A. L.; Mitterbauer, C.; Browning, N. D.; Kauzlarich, S. M.; Power, P. P. Room Temperature Synthesis of Surface-Functionalized Boron Nanoparticles. *Chem. Commun.* **2007**, 580-582.

(28) Shin, W. G.; Calder, S.; Ugurlu, O.; Girshick, S. L. Production and Characterization of Boron Nanoparticles Synthesized with a Thermal Plasma System. *J. Nanopart. Res.* **2011,** *13*, 7187-7191.

(29) Van Devener, B.; Perez, J. P. L.; Jankovich, J.; Anderson, S. L. Oxide-Free, Catalyst-Coated, Fuel-Soluble, Air-Stable Boron Nanopowder as Combined Combustion Catalyst and High Energy Density Fuel. *Energy Fuels* **2009,** *23*, 6111-6120.

(30) Manikam, V. R.; Cheong, K. Y.; Razak, K. A. Chemical Reduction Methods for Synthesizing Ag and Al Nanoparticles and Their Respective Nanoalloys. *Mater. Sci. Eng., B* **2011,** *176*, 187-203.

(31) Kumar, B.; Thareja, R. K. Synthesis of Nanoparticles in Laser Ablation of Aluminum in Liquid. *J. Appl. Phys.* **2010,** *108*, 064906/1-069406/6.

(32) Van Devener, B.; Perez, J. P. L.; Anderson, S. L. Air-Stable, Unoxidized, Hydrocarbon-Dispersible Boron Nanoparticles. *J. Mater. Res.* **2009,** *24*, 3462-3464.

(33) Van Devener, B.; Perez, J. P. L.; Jankovich, J.; Anderson, S. L. Oxide-Free, Catalyst-Coated, Fuel-Soluble, Air-Stable Boron Nanopowder as Combined Combustion Catalyst and High Energy Density Fuel. *Energy Fuels* **2009,** *23*, 6111-6120.

(34) Tran, A. T.; Huynh, V. A.; Friz, E. M.; Whitney, S. K.; Cordes, D. B. A General Method for the Rapid Reduction of Alkenes and Alkynes Using Sodium Borohydride, Acetic Acid, and Palladium. *Tetrahedron Lett.* **2009,** *50*, 1817-1819.

(35) Magee, J. W.; Kabo, G. J.; Frenkel, M. *Physical Property Measurements and a Comprehensive Data Retrieval System for Ionic Liquids*, 226th ACS National Meeting, New York, NY, 2003.

(36) Visser, A. E.; Swatloski, R. P.; Reichert, W. M.; Mayton, R.; Sheff, S.; Wierzbicki, A.; Davis, J. H.; Rogers, R. D. Task-Specific Ionic Liquids Incorporating Novel Cations for the Coordination and Extraction of Hg^{2+} and Cd^{2+}: Synthesis, Characterization, and Extraction Studies. *Environ. Sci. Technol.* **2002,** *36*, 2523-2529.

(37) Ngo, H. L.; LeCompte, K.; Hargens, L.; McEwen, A. B. Thermal Properties of Imidazolium Ionic Liquids. *Thermochim. Acta* **2000,** *357-358*, 97-102.

(38) Chambreau, S. D.; Schneider, S.; Rosander, M.; Hawkins, T. W.; Gallegos, C. J.; Pastewait, M. F.; Vaghjiani, G. L. Fourier Transform Infrared Studies in Hypergolic Ignition of Ionic Liquids. *J. Phys. Chem. A* **2008,** *112*, 7816-7824.

(39) Hawkins, T. W.; Schneider, S.; Drake, G. W.; Vaghjiani, G.; Chambreau, S. *Hypergolic Fuels.* 11/973,978 US Patent 8,034,202 B1, Oct 11, **2011**.

(40) Schneider, S.; Hawkins, T.; Ahmed, Y.; Rosander, M.; Hudgens, L.; Mills, J. Green Bipropellants: Hydrogen-Rich Ionic Liquids That Are Hypergolic with Hydrogen Peroxide. *Angew. Chem. Int. Ed.* **2011,** *50*, 5886 –5888.

(41) Schneider, S.; Hawkins, T.; Rosander, M.; Vaghjiani, G.; Chambreau, S.; Drake, G. Ionic Liquids as Hypergolic Fuels. *Energy Fuels* **2008,** *22*, 2871-2872.

(42) Zhang, Y.; Gao, H.; Joo, Y.-H.; Shreeve, J. M. Ionic Liquids as Hypergolic Fuels. *Angew. Chem. Int. Ed.* **2011,** *50*, 9554-9562.

(43) Huzel, D. K.; Huang, D. H. *Modern Engineering for Design of Liquid-Propellant Rocket Engines.* American Institute of Aeronautics and Astronautics, Inc.: Washington, D.C., 1992.

(44) Xue, H.; Gao, Y.; Twamley, B.; Shreeve, J. M. *Chem. Mater.* **2005,** *17*, 191-198.

(45) Catoire, L.; Chambreau, S. D.; Vaghjiani, G. L. Chemical Kinetics and Interpretation of Hypergolicity of Dicyanamide Ionic Liquid-Based Systems. *Combustion Flame* **2012,** *159*, 1759-1768.

(46) Zhang, Y.; Shreeve, J. M. Dicyanoborate-Based Ionic Liquids as Hypergolic Fluids. *Angew. Chem. Int. Ed.* **2011,** *50*, 935-937.

(47) Xue, H.; Arritt, S. W.; Twamley, B.; Shreeve, J. M. *Inorg. Chem.* **2004,** *43*, 7972-7977.

(48) Gao, Y.; Arritt, S. W.; Twamley, B.; Shreeve, J. M. Guanidinium-Based Ionic Liquids. *Inorg. Chem.* **2005,** *44*, 1704-1712.

(49) Jin, C.-M.; Ye, C. F.; Piekarski, C.; Twamley, B.; Shreeve, J. M. Mono and Bridged Azolium Picrates as Energetic Salts. *Euro. J. Inorg. Chem.* **2005,** *2005*, 3760-3767.

(50) Xue, H.; Gao, Y.; Twamley, B.; Shreeve, J. M. *Inorg. Chem.* **2005,** *44*, 5068-5072.

(51) Xue, H.; Gao, Y.; Twamley, B.; Shreeve, J. M. Energetic Azolium Azolate Salts. *Inorg. Chem.* **2005,** *44*, 5068-5072.

(52) Xue, H.; Twamley, B.; Shreeve, J. M. *Adv. Mater.* **2005,** *17*, 2142-2146.

(53) Ye, C.; Xiao, J.-C.; Twamley, B.; Shreeve, J. M. *Chem. Commun.* **2005**, 2750-2752.

(54) Gao, H.; Ye, C.; Piekarski, C. M.; Shreeve, J. n. M. Computational Characterization of Energetic Salts. *J. Phys. Chem. C* **2007,** *111*, 10718-10731.

(55) *Energetic Materials: Part 1. Decomposition, Crystal and Molecular Properties*. Elsevier: Amsterdam, The Netherlands, 2003.

(56) Fried, L. E.; Manaa, M. R.; Pagoria, P. F.; Simpson, R. L. Design and Synthesis of Energetic Materials *Annu. Rev. Mater. Res.* **2001,** *31*, 291-321.

(57) Politzer, P.; Murray, J. S.; Seminario, J. M.; Lane, P.; Grice, M. E.; Concha, M. C. Computational Characterization of Energetic Materials. *J. Molec. Struc. (Theochem)* **2001,** *573*, 1-10.

(58) Rice, B. M.; Pai, S. V.; Hare, J. Predicting Heats of Formation of Energetic Materials Using Quantum Mechanical Calculations. *Combustion Flame* **1999,** *118*, 445-458.

(59) Gao, Y.; Gao, H.; Piekarski, C.; Shreeve, J. n. M. Azolium Salts Functionalized with Cyanomethyl, Vinyl, or Propargyl Substituents and Dicyanamide, Dinitramide, Perchlorate and Nitrate Anions. *Eur. J. Inorg. Chem.* **2007,** *2007*, 4965-4972.

(60) Hammerl, A.; Hiskey, M. A.; Holl, G.; Klapötke, T. M.; Polborn, K.; Stierstorfer, J.; Weigand, J. J. Azidoformamidinium and Guanidinium 5,5'-Azotetrazolate Salts. *Chem. Mater.* **2005,** *17*, 3784-3793.

(61) Katritzky, A. R.; Singh, S.; Kirichenko, K.; Holbrey, J. D.; Smiglak, M.; Reichert, W. M.; Rogers, R. D. 1-Butyl-3-Methylimidazolium 3,5-Dinitro-1,2,4-Triazolate: A Novel Ionic Liquid Containing a Rigid, Planar Energetic Anion. *Chem. Commun.* **2005**, 868-870.

(62) Katritzky, A. R.; Singh, S.; Kirichenko, K.; Smiglak, M.; Holbrey, J. D.; Reichert, W. M.; Spear, S. K.; Rogers, R. D. In Search of Ionic Liquids Incorporating Azolate Anions. *Chem. Eur. J.* **2006,** *12*, 4630-4641.

(63) Xue, H.; Twamley, B.; Shreeve, J. M. *J. Mater. Chem.* **2005,** *15*, 3459-3465.

(64) Xue, H.; Twamley, B.; Shreeve, J. M. *Inorg. Chem.* **2005,** *44*, 7009-7013.

CHAPTER 2

STUDIES ON FUNCTIONALIZING BORON NANOPARTICLES WITH OLEIC ACID AND 1-OCTENE FOR SUSPENSION IN LIQUID HYDROCARBON FUELS

2.1 Overview

In previous studies, oleic acid was used both as a passivating and stabilizing ligand for the synthesis of boron nanoparticles using ball milling technique.[1] Here, the binding of oleic acid molecules to the surface of boron nanoparticles was studied by Fourier transform infrared spectroscopy (FTIR), ^{13}C-nuclear magnetic resonance spectroscopy (^{13}C-NMR), and thermogravimetric analysis (TGA). Results show that both oleic acid and oleate species were adsorbed strongly on the nanoparticle surface. Oleate species were found to bind through a bridging bidentate interaction, where the two oxygen atoms of a single molecule bind separately to two different boron atoms. For ligands like oleate, binding to the surface relies on reactions that oxidize some boron in the surface layer, which is potentially disadvantageous for particles developed for combustion applications. This chapter also examines an alternate approach where the boron particle surfaces are first functionalized with hydrogen atoms, and then reacted with an alkene (1-octene) to produce alkylated boron nanoparticles.

2.2 Introduction

Boron's complete oxidation to solid B_2O_3 is a highly exothermic reaction that releases 59 kJ of heat per gram of boron burned.[2] This value is significantly larger than that of commercial fuels and other known oxidizable metals such as aluminum (31 kJ/g) and magnesium (24 kJ/g).[2] It is for this reason that elemental boron and its compounds were considered viable candidates for fuel applications.[3] Hydrogenated compounds of boron (boron hydrides) such as diborane, pentaborane, and decaborane were among the first species studied due to their faster ignition as compared to other boron compounds.[4-10] However, the toxicity of these boron hydrides and their pyrophoric behavior in air presented difficulties in handling and storage, thereby making their large scale use problematic.

Elemental boron and other boron-based materials such as metal borides and boron carbide were also studied as potential propellant constituents.[11] Micron-sized boron particulates were mixed with liquid hydrocarbon fuels (i.e., liquid alkanes, kerosene, and jet propulsion or JP fuels) to make slurries. Ignition, combustion, and energetic properties of these mixtures were then investigated via open flame spectroscopic methods.[12-15] Powdered boron was also mixed with polymeric binders and cast as solid fuels in hybrid propulsion systems.[16-17] Results of particle combustion studies showed that boron particles undergo a two-step ignition process when burned. The first stage involves the melting of the native boron oxide layer at lower temperatures (~450 °C), which unfortunately promotes formation of larger particle aggregates, followed by ignition of elemental boron once the oxide has vaporized (~1800 °C).[18] In a study of boron compounds, Hsia[19] looked into the combustion and ignition behavior of aluminum, magnesium, and lithium borides using an optical burner system. This showed that MgB_{12} and LiB_2 oxidized completely with shorter ignition delays although their heats of combustion are relatively lower than elemental boron. Similarly, boron carbide combustion was also investigated in a number of theoretical[20] and experimental[21-24] studies. Nabity,[23] studied the effects of particle size, equivalence ratio, air mass flux, and inlet air temperatures in the combustion of micron-sized boron carbide particulates in a ramjet burner. Increased combustion efficiency was observed for smaller particles, higher inlet temperatures, and lower air flux. Despite these advances, harnessing the full energy potential of boron or its compounds remains complicated. Boron's high vaporizing temperatures (3500 – 4000 °C) confine the combustion of particles to a heterogeneous process where a diffusion-limited rate governs the reaction. Furthermore, most of these particles are coated with a refractory oxide layer on the surface due to exposure to air preventing immediate ignition of the particles when mixed with an oxidizer.

Using nanoparticulate boron fuel is one possible solution that can be utilized to augment the problem on combustion rate. A significant increase in the ignition and flame propagation of aluminum nanothermites was observed when the particle size was reduced to 50 – 200 nm.[25] Furthermore, ignition temperature of oxide-coated boron powders was shown to decrease with size in particles 50 – 300 μm in diameter.[26] These results demonstrated the potential of using nanoparticulate boron powder to completely burn solid boron as fuel.

In a previous study, we were able to synthesize boron nanoparticles 50 – 100 nm in diameter using optimized ball milling procedures.[1] Ball milling techniques have the advantage of producing large quantities of boron nanoparticles in a short period of time and at a lower cost as compared to currently existing synthetic methods.[27-30] Characterization of boron nanoparticles produced through our milling method showed that the surface was oxide-free. Furthermore, the presence of an added ligand, oleic acid, protected the particles from unwanted oxidation in air and promoted stable suspensions in hexane and jet fuels.[1]

In this chapter, I discuss the modification of the milling procedure to take advantage of a planetary mill to scale up the process. Boron nanoparticles were characterized for their size and oxidation state. Furthermore, we characterized the nature of the binding between oleic acid and the boron nanoparticles. Fourier transform infrared (FTIR) and ^{13}C-nuclear magnetic resonance (^{13}C-NMR) spectroscopies were used to determine the structure of ligand molecules on the surface, and thermogravimetric analysis (TGA) was done to quantify the amount of oleic acid bound to the particle.

Finally, a new milling procedure is discussed in this chapter where boron is milled with H_2 gas in a dry milling process. This method yielded a more activated H-terminated boron surface, which was then allowed to react with an alkene resulting in alkylated boron nanoparticles.

2.3 Methodology

2.3.1 Boron nanoparticle synthesis. Boron feedstock (95 % ~2 μm) used for this experiment was purchased from C.R. Supply Co. (West Hills, CA). Oleic acid was purchased from Sigma-Aldrich (St. Louis, MO), and used as received. The procedure that we developed and published previously[1] was modified for use with a larger mill (Retsch, Inc. PM 400 model) to scale up the process. This planetary mill can accommodate four 500-mL tungsten carbide-lined milling jars effectively increasing the capacity 50-fold than when using the smaller shaker/mixer mill (Certiprep 8000M model). Because the larger planetary mill generates lower collision forces[31] than the shaker mill used in previous work, the milling process was modified accordingly. Milling time was increased to compensate for lower collision forces, and a three-stage milling process was employed composed of dry milling, ligand milling, and solvent milling stages. The dry milling stage serves to initially reduce particle sized and expose unoxidized boron surfaces. In this stage, 5 g of boron feedstock was milled with 400 g of ⅛ inch tungsten carbide milling media (an 80:1 charge ratio for milling media and boron powder) for 12 hours under nitrogen atmosphere without any surfactant or wetting agent. The mill was operated at 300 revolutions per minute (rpm), and its rotation reversed every 30 minutes with a 5-minute cooling/rest interval in between each 30 minute cycle. Five mL of oleic acid was then added to the dry-milled boron and the mixture was remilled for an additional 3 hours. This "ligand milling" stage allows for interaction between unoxidized boron surfaces and oleic acid molecules. Finally, in the solvent-milling stage, hexane (150 mL) was added to the mixture and milled for 6 hours to allow further size reduction of the particles and promote better suspension. Handling of the milling jar for addition of ligand and solvent was done inside a N_2-filled glovebox to ensure that the boron nanoparticles produced through the different stages would not be oxidized

by O_2 from air. In addition, unpassivated boron nanoparticles are highly pyrophoric and exposure to air may lead to spontaneous ignition of the dry milled particles. The use of the glovebox prevented accidents while doing this procedure.

For the hydrogenation reaction, dry milling was done in an H_2 atmosphere. One g of boron powder was charged with 160 g of tungsten carbide media and sealed inside the milling jar. With the use of a port valve fabricated on the cap of the milling jar, the jar was purged with argon gas by evacuation and pumping argon in to a pressure of 20 psi above atmosphere. Purging was done three times to effectively remove O_2 and N_2 gases coming from air exposure. H_2 gas was then pumped in at a pressure of 20 psi above atmosphere, and milled for 12 hours. The pressure of H_2 inside the jar was monitored every 3 hours and then charged back to 20 psi with H_2. After the dry milling stage, the jar was opened inside the glovebox and 5 mL of 1-octene (Sigma-Aldrich, St. Louis, MO) was added. The jar was again purged and charged with 20 psi of argon, and then further milled for 12 hours at 100 rpm. The goal for this step was to mix the hydrogenated boron nanoparticles with octene, allowing reaction. The lower mill rotation rate was used to minimize crushing and size reduction of the particles, because this would expose additional, unhydrogenated boron surfaces that might not be passivated by interaction with octene. Boron nanoparticles produced through both milling processes were characterized for their size, oxidation state, and chemical composition.

2.3.2 Size characterization. Individual particle size was determined using scanning electron microscopy (SEM) imaging. Nanoparticles were centrifuged out of the suspension and washed with ethanol through sonication. This washing process was performed three times to remove excess organic ligands which cause unwanted charging artifacts in SEM imaging. The particles were then suspended in ethanol and drop cast on a transmission

electron microscopy (TEM) grid (Ted Pella, Inc., Redding, CA) coated with a 3-nm thick lacey formvar. Size distribution was analyzed by dynamic light scattering (DLS) method using a Particle Sizing System Nicomp 380 instrument (PSS, Inc., Port Richey, FL). Washed samples were diluted and dispersed in hexane for DLS analysis.

2.3.3 X-ray photoelectron spectroscopy (XPS). A Kratos Axis Ultra instrument (Chestnut Ridge, NY) was used for XPS analysis. Spectra were taken using a monochromatic Al Kα source (1486.7 eV kinetic energy) at a 300 x 700 μm spot size. Samples were prepared by washing them with ethanol, as mentioned above and drying them in air. The particles were then pressed on a carbon tape atop a copper shim. Samples were placed inside the ultrahigh vacuum (UHV) chamber of the XPS overnight to further remove volatile species before analysis. Low resolution survey and high resolution region scans were taken for each sample. During analysis, samples were flooded with low energy electrons from the instrument's charge neutralizer to minimize the charging. All spectra were analyzed using CASA XPS software with binding energies corrected by referencing adventitious C 1s peak to 284.5 eV.

2.3.4 Fourier transform infrared (FTIR) analysis. A Nicolet iS5 FTIR spectrometer (Thermo Fisher Scientific, Waltham, MA) was used to collect infrared (IR) spectra using an attenuated total reflectance (ATR) set-up. The samples were washed with ethanol to remove excess ligand molecules, then air-dried and pressed on a diamond crystal of the FTIR sampling module. Fifteen independent spectra were taken with 1 cm^{-1} resolution and then averaged.

2.3.5 ^{13}C-nuclear magnetic resonance (^{13}C-NMR) analysis. Solid state NMR spectrum was recorded using a ^{13}C CP/MAS experiment (cross-polarization/magic-angle spinning) in a Varian VXR 500 Spectrometer (Varian, Palo Alto, CA). Resonances

frequencies for ^{13}C (observed) and ^{1}H (match/decouple) were 25.152 MHz and 100.0196 MHz, respectively. The matching condition was established using ^{13}C and ^{1}H pulse widths of 4.1 microseconds. The spectrum was recorded using 300,000 transients, and digitized using a dwell time of 50 microseconds (spectral width of 20 kHz) into 1024 complex points (50 millisecond acquisition time). The sample spinning rate was 820 Hz and the rotational axis was set at 54.7356° with respect to the static field axis, (e.g., the standard magic angle).

2.3.6 Thermogravimetric analysis (TGA). TGA experiments were done using a TGA 2950 Thermogravimetric Analyzer (TA Instruments, New Castle, DE) under an argon atmosphere. Mass changes were monitored from 35 – 800 °C at a ramp rate of 10 °C/min. TGA data were analyzed using TA Universal Analysis Software.

2.4 Results and Discussion

2.4.1 Particle size characterization. Previously, we have shown that oleic acid-passivated, oxide-free boron nanoparticles can be produced through mechanical milling. In that study, a 50-mL capacity tungsten carbide-lined milling jar and a bench top shaker/mixer mill (SPEX 8000M model) were used for the preparation of boron nanoparticles from oxide-coated boron powder feedstock. As mentioned previously, one major advantage of developing ball milling techniques for sample preparation is the ease of adapting the method for industrial-scale production, where large quantities of samples are produced. However, different ball milling machines operate under different mechanisms prompting modifications in milling parameters and procedures. Milling time, rotational speed, milling media charge ratio, use of wetting agents, jar atmosphere, and temperature are a few factors that can be varied and optimized.[32] In this study, we modified our previous milling procedure for the newly acquired planetary ball mill. Since the planetary ball mill is less powerful than the shaker mill, several milling methods were tested. We optimized a three-step milling process

comprised of dry milling, ligand milling, and solvent milling for sample preparation. A major modification was to implement a longer milling time to achieve the desired size of boron particles. SEM images of the product (Figure 2.1) showed that irregularly shaped particles as small as 50 nm can be produced through the new procedure, although aggregation was also observed due to the drying of the solvent on the grid. A typical mass weighted size distribution of the nanoparticles is displayed in Figure 2.2. Figure 2.2a shows 30 % of the particles have an average diameter of about 150 nm while the remaining 70 % is composed of larger 500 nm particles. The large particles can be separated by allowing them to settle from the suspension, leaving the small particles dispersed in the solvent (Figure 2.2b). For industrial applications and economic considerations, the large particles can be replaced back into the jar and remilled. These results indicate that by simply modifying milling procedures and adapting them to a particular milling instrument, boron particles as small as 50 nm can still be produced, strengthening our initial claim that this synthetic method is easily scalable to industrial size.

2.4.2 Characterization of oxidation state of boron nanoparticles. The oxidation state of boron nanoparticles was analyzed using X-ray photoelectron spectroscopy (XPS). XPS is a surface sensitive technique that probes the upper layer of a sample (up to 10 nm depending on the material). The sample is bombarded by monochromatic radiation from an aluminum source with a kinetic energy of 1486.7 eV, which interacts with the core electrons of the atom, ejecting them from their orbitals as photoelectrons with distinct kinetic energies. From the measured kinetic energies, the binding energies of the ejected photoelectrons are calculated, and information about the chemical environment of the boron atom where the photoelectrons originated is obtained. In general, electrons situated closer to the nucleus have higher binding energies due to electrostatic attraction to the positively charged nucleus.

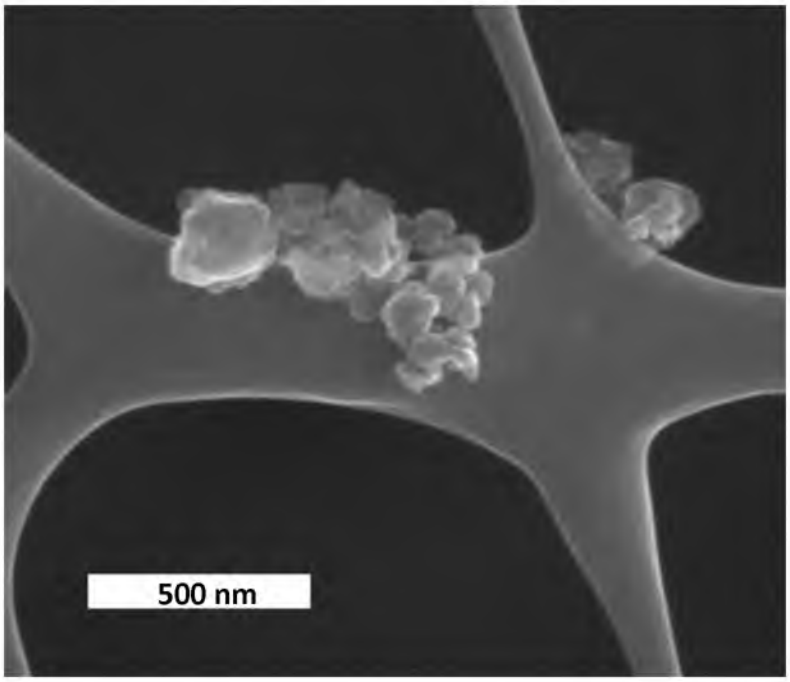

Figure 2.1 Scanning electron micrograph (SEM) image of boron nanoparticles produced through the three-stage milling process using Retsch PM 400 planetary ball mill. Image shows aggregated particles as small as 50 nm in diameter. The gray band stretching through the image is the lacey formvar carbon on the TEM grid.

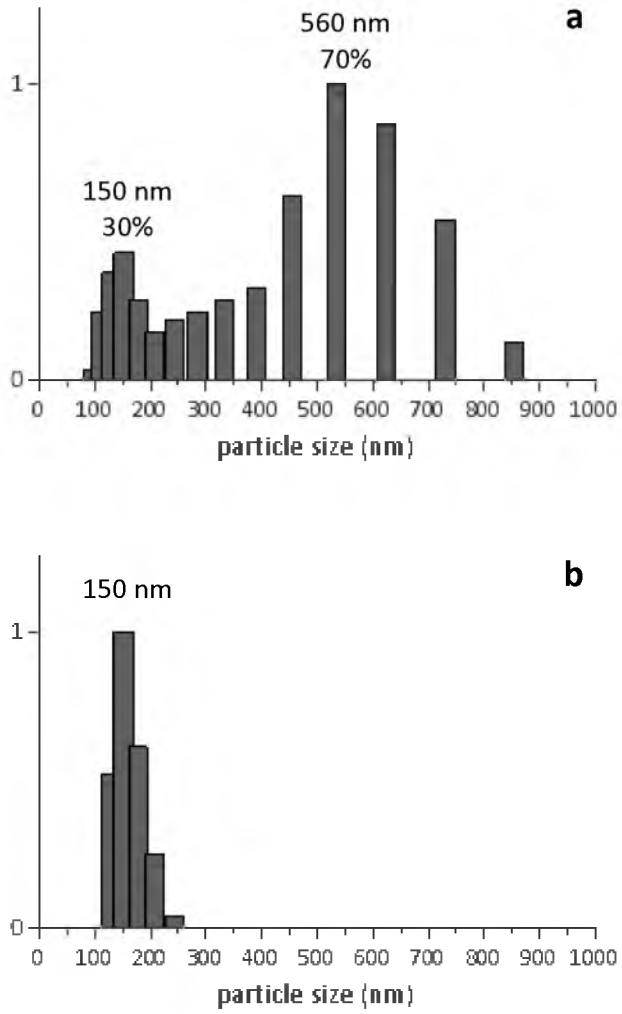

Figure 2.2 Mass weighted size distribution of boron nanoparticles produced through the modified three-stage procedure using the planetary ball mill (Retsch PM 400 model) showing **(a)** both small and large particles in the as milled sample and **(b)** small particles remaining after the large particles were separated by allowing it to settle.

For elemental boron, B^0, the binding energy of the core 1s electron has a value of 188 eV.[33] When boron binds to a more electronegative atom (essentially oxidizing boron in the process), valence electrons are pulled favorably towards the other atom resulting in an increase in the binding energies of boron's core electrons. Fully oxidized boron, B^{3+}, for example, has a measured binding energy of 193 eV,[33] hence any oxidation of the nanoparticles resulting from air exposure can be detected through the binding energy shift of the B 1s signal. Figure 2.3 compares high resolution B 1s spectrum of boron nanoparticles produced using the procedure mentioned in section 2.3.1, milled with and without oleic acid, and unmilled boron feedstock. The feedstock is typically coated with a native oxide layer which can be observed as a small peak at 193 eV (Figure 2.3a). This oxide peak is more clearly seen in the blown up spectrum shown in the inset. When boron was dry milled and then milled in hexane without oleic acid as a ligand, and then exposed to air, boron atoms were also oxidized to B_2O_3 (Figure 2.3b). Hexane did not react with boron and did not provide a protective layer against oxidation. It only served as a wetting agent to prevent caking of dried boron on the walls of the jar, thereby allowing efficient milling of the powder. A large increase in intensity of the 193 eV peak compared to the unmilled boron feedstock was observed due to oxidation of much smaller particles exposing a larger surface area. However, when ligand milling was introduced in the process, the particles produced were protected from air oxidation. Figure 2.3c (inset) shows no significant increase in the oxide peak. Furthermore, a peak between 193 and 188 eV (for fully oxidized and unoxidized boron, respectively) appeared in the deconvoluted spectrum. This can be attributed to the binding of oleic acid to the surface of the boron nanoparticles, the mode of which will be further discussed later. Together, these findings corroborate our previous results obtained

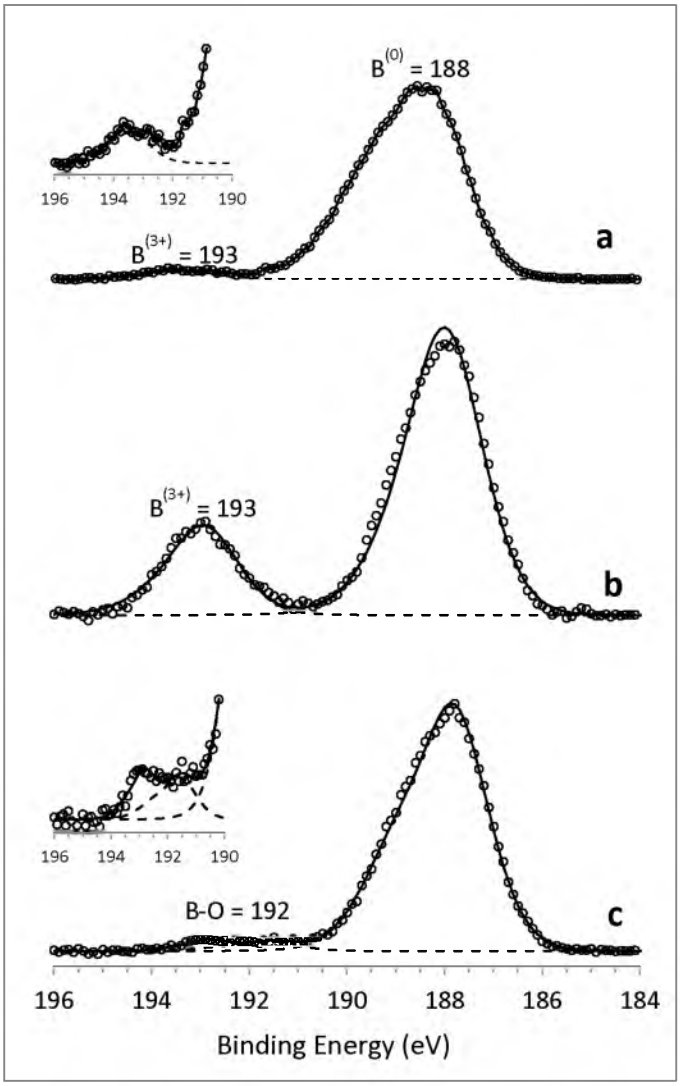

Figure 2.3 B 1s X-ray photoelectron spectra of **(a)** boron feedstock, **(b)** samples milled in hexane without oleic acid, and **(c)** boron samples milled in hexane with oleic acid ligand.

using small-scale milling. More importantly, they demonstrate that passivated boron nanoparticles can also be obtained through this modified process for large-scale milling.

2.4.3 Interaction of oleic acid with boron nanoparticles. Oleic acid is generally used as a ligand molecule in the synthesis of metal nanoparticles such as iron,[34] cobalt,[35-36] and gold.[37] In solution-phase reduction methods where nanoparticles are synthesized from metallic complexes, oleic acid forms micellar structures in nonpolar solvents (i.e., hexane, toluene, chloroform) with the polar carboxylic acid moiety confined in the center. These micelles act as nanoreactors where the hydrophilic complexes may dissolve. Addition of a reducing agent consequently produces metallic nanoparticles inside the oleic acid micelles. The size of nanoparticles produced was found to depend on the size of micelles, which in turn varied with the concentration of oleic acid in the mixture.[38-40] Although ball milling is a top-down approach for nanoparticle synthesis (as compared to the bottom-up approach for solution-phase reduction methods), oleic acid was also found to be effective in stabilizing and protecting boron nanoparticles from reactive environments.

FTIR spectroscopy was used to analyze the binding of oleic acid molecules on the surface of boron nanoparticles. Figure 2.4 displays FTIR spectra of neat oleic acid and boron samples milled with oleic acid and hexane, washed with ethanol and dried in air. For oleic acid, distinct peaks at 2927 cm^{-1} and 2855 cm^{-1} (asymmetric and symmetric νCH_2), 1711 cm^{-1} ($\nu C{=}O$), 1464 cm^{-1} ($\delta O{-}H$), and 1285 cm^{-1}($\nu C{-}O$) were observed in the spectrum.[35] Upon examining the boron milled spectrum, we observed that the CH_2 stretching bands were shifted to lower frequency (2920 and 2852 cm^{-1} for asymmetric and symmetric stretches, respectively). This can be attributed to the interaction of the hydrocarbon chain with the particle surface which perturbs the vibration of the C–H bond.[35,41-42] IR peaks at 1709 cm^{-1} and 1590 cm^{-1} were also observed in the spectrum. These peaks correspond to

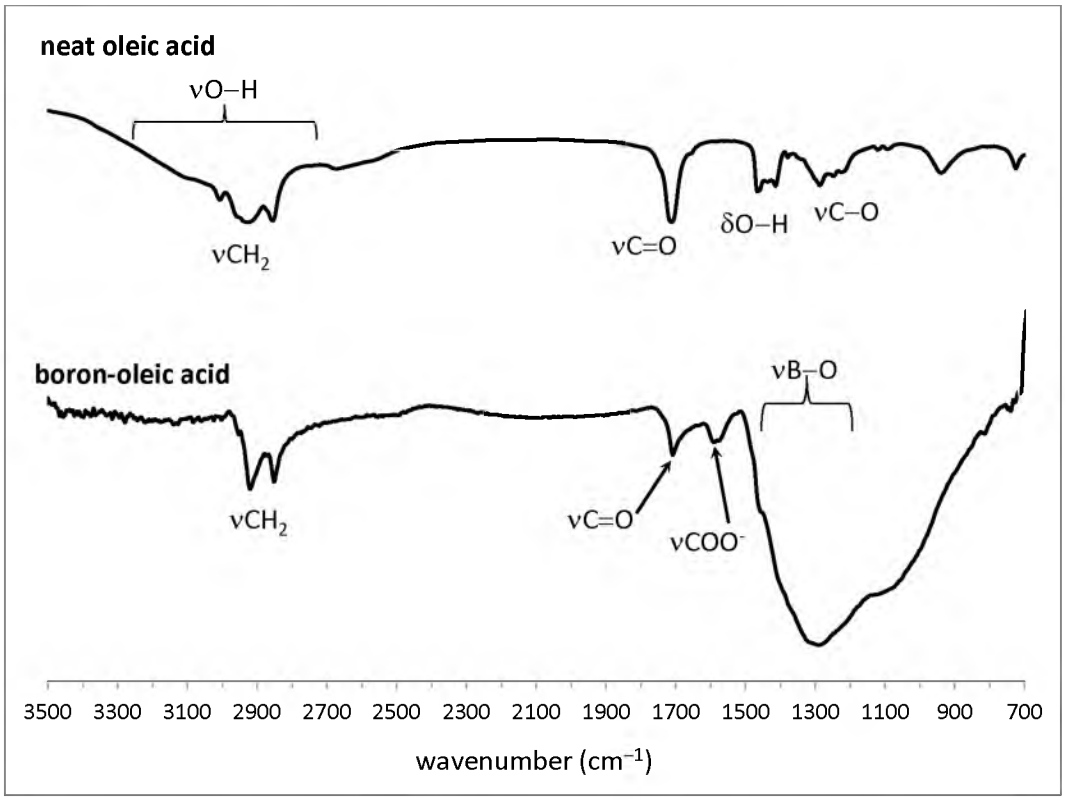

Figure 2.4 Fourier transform infrared (FTIR) spectra of oleic acid and boron milled with oleic acid showing significant IR peaks.

the stretching vibrations of the carboxylic group of oleic acid. Also noticeable was the decrease in intensity of the broad O–H stretch at 3000 – 3300 cm^{-1} region which suggests that carboxylic acid must have dissociated to carboxylate upon interaction with boron. This was confirmed by the presence of a huge, broad band at 1350 cm^{-1} which is attributed to the B–O stretching vibration. Interestingly, we observed a band at 1709 cm^{-1} which can be attributed to C=O stretching in free COOH (as seen in neat oleic acid). The band observed at 1590 cm^{-1} is attributed to COO^- species (asymmetric stretch), together with a symmetric stretch at 1450 cm^{-1}, which was observed as a small shoulder on the broad B–O stretching band in this spectrum. Oxygen atoms on the oleic acid molecule may bind with the boron atoms through three different modes: (1) monodentate, where the carboxyl group remains

unchanged and the negatively charged oxygen covalently binds to a boron atom; (2) chelating bidentate, where two oxygen atoms bind to a single boron atom; and (3) bridging bidentate where the two oxygen atoms covalently bind to two separate boron atoms on the surface. Figure 2.5 shows a cartoon diagram describing these binding interactions. The wavenumber separation, Δ, between the asymmetric and symmetric stretching vibrations of the COO^- group gives information on the specific mode of binding of the carboxylate with boron atoms on the surface of the nanoparticles.[43-45] Values for Δ are largest for monodentate interactions (200 – 300 cm^{-1}) and smallest for chelating bidentate interactions (<110 cm^{-1}),[44-45] whereas intermediate Δ values can be attributed to bridging bidentate interactions which is more likely the case for boron–oleic acid system (1590 – 1463 = 127 cm^{-1}). However, the presence of the C=O band at 1709 cm^{-1} despite five thorough washings with ethanol using a series of sonication and centrifuging, suggests that undissociated oleic acid molecules may have adsorbed strongly on the particles. Further discussion on this interaction is presented later. Nevertheless, the FTIR results confirm our initial hypothesis that boron nanoparticles could interact with the carboxylic group of oleic acid via formation of a B–O–C bond.[1]

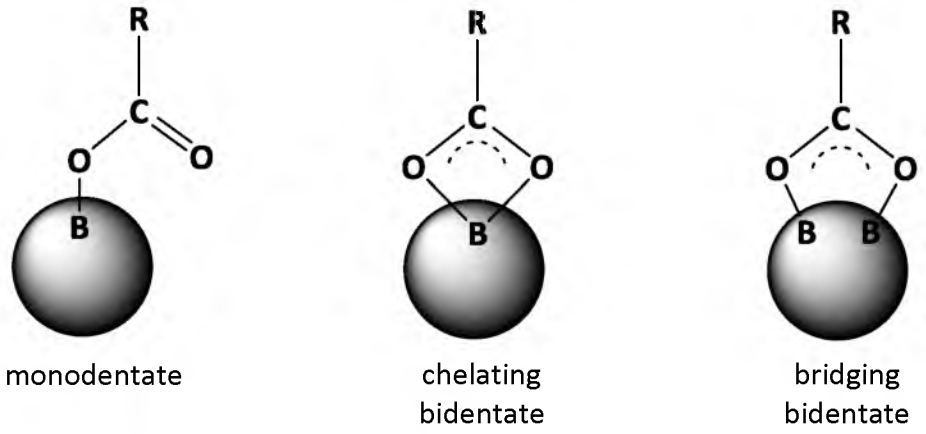

Figure 2.5 Possible binding interactions between an oleate and boron atoms on the surface of the nanoparticles.

^{13}C-NMR was also performed to confirm the carboxylate interaction with boron. Figure 2.6 displays the solid state ^{13}C-NMR spectrum of oleic acid functionalized boron nanoparticles after washing with ethanol. Resonance peaks typical of oleic acid molecules[46] are observed at 179 ppm (C=O), 132 ppm (C=C), 24 – 30 ppm (CH_2), and 15 ppm (CH_3) as shown in the figure. Interestingly, these peaks were noticeably broadened presumably due to interaction of oleic acid molecules with the nanoparticle surface.[47-49] Specifically, the resonance peak of the C=O carbon was broadened and shifted by ~28 ppm downfield to 207 ppm. A larger peak remains unchanged at 179 ppm, possibly due to strongly adsorbed free oleic acid. These results corroborate our FTIR data and further strengthen our argument that oleic acid molecules interact with boron nanoparticles via the carboxylate group and

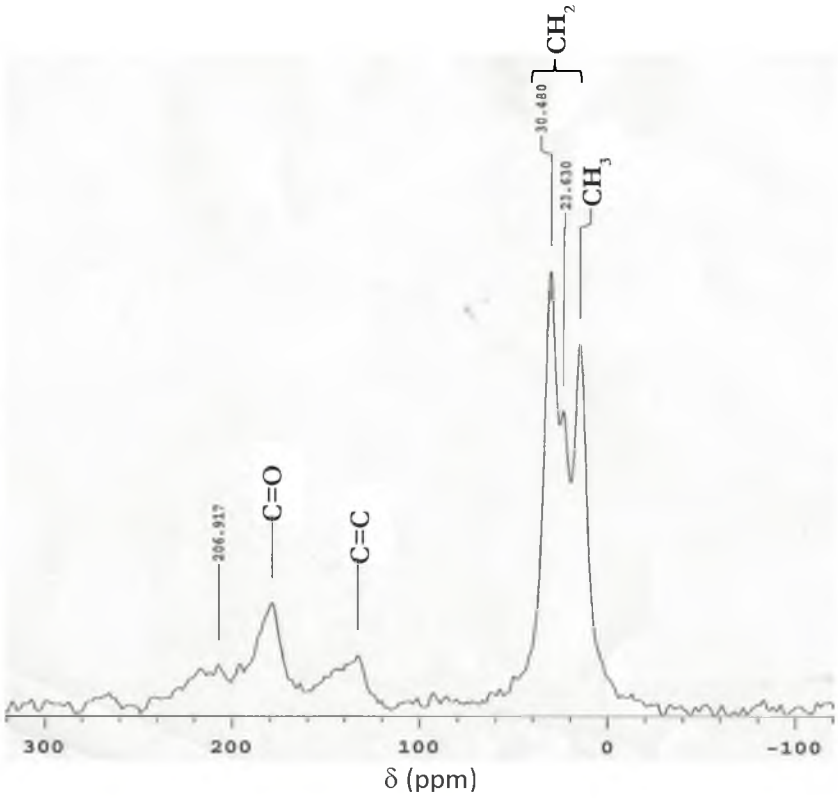

Figure 2.6 ^{13}C-NMR spectrum of boron nanoparticles coated with oleic acid.

form a B–O bond. The downfield shift has also been seen in the esterification of oleic acid with starch molecule to form a starch oleate.[46] The same downfield shifts were also detected in carbon atoms bonded to sulfur in alkanethiol functionalized gold nanoparticles.[48-49] Furthermore, in the cysteine–gold nanoparticle interaction where the carboxylate group does not bind with the nanoparticle, there was no evidence of a downfield shift or broadening of the C=O resonance peak. Instead, broadening and chemical shifts were observed on low-frequency resonance peaks assigned to the carbon atom bonded to sulfur.[47,50]

2.4.4 Oleate desorption and ligand coverage analysis. Thermogravimetric analysis was used to quantitate the amount of oleic acid bound to the boron nanoparticles. Prior to analysis samples were washed thoroughly with ethanol to remove excess, unbound oleic acid. Figure 2.7 displays a mass percent-temperature profile of boron nanoparticles heated from 35 – 800 °C. Initial mass loss observed at temperatures <100 °C can be attributed to volatile species that were not completely removed by air drying (i.e., ethanol and hexane solvents). This plot suggests that a two-stage decomposition process occured when the sample was heated to 500 °C. The low temperature dissociation (~300 °C) is attributed to weakly bound oleic acid molecules, while the higher temperature corresponds to covalently bound oleate species. Complete decomposition/dissociation of the organic ligand occurred at ~500 °C, after which a mass increase of about 8 % was observed, which is likely due to the partial leak of air into the TGA instrument's gas line causing the stripped boron nanoparticles to oxidize. The mass loss measured amounts to 25 % of the initial sample mass, which would correspond to 1.0×10^{-5} fg/nm^2 (22 oleic acid molecule/nm^2) of surface coverage assuming a minimum diameter of 80 nm for the particles (details of this calculation are presented in Appendix A). This would deposit ~5 monolayers of closely packed oleic acid molecules on the boron surface. The existence of a close-packed secondary layer like the one observed in

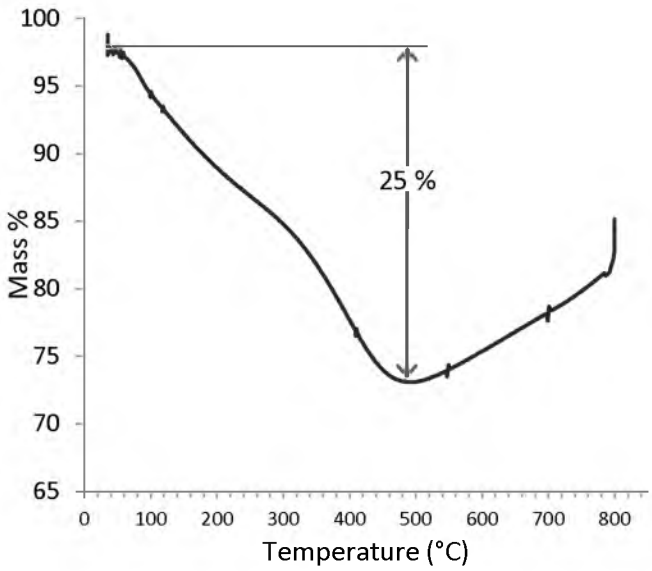

Figure 2.7 TGA spectrum of boron nanoparticles functionalized with oleic acid.

the cysteine–gold nanoparticle system is less likely to occur in a ligand such as oleic acid. This is because cysteine's zwitterionic character, which allows for better interaction of the amino end of a bonded molecule to the carboxylic end of a solvated molecule to form a distinct double layer,[47] is not present in oleic acid. However, intercalation of free oleic acid molecules between surface-bonded oleate is still probable. The same mechanism/structure was observed in the CdSe/ZnS–surfactant systems, and was justified by van der Waals interactions between the long hydrocarbon chain and hydrogen bonding between the polar head groups.[51-52]

2.4.5 Functionalizing boron nanoparticles with long chain alkyls. Oleic acid proved to be a suitable ligand for functionalizing boron nanoparticles intended to be dispersed in nonpolar solvents. Boron's high reactivity with oxygen allows it to bind with the carboxylate group's polar head while the nonpolar hydrocarbon chain extends outward providing steric repulsion between particles and preventing irreversible aggregation. However, the presence of reactive oxygen in the ligand contributes to a lowered energy

density that becomes significant as particles become much smaller. It is therefore desirable to use an alternative ligand that will introduce alkyl groups on the boron surface through a B–C bond. The problem with using these alternative ligands is that the reaction of boron and carbon containing compounds do not necessarily proceed through the attack of boron directly to carbon or vice versa. To solve this problem, we used hydroboration reaction which is popularly utilized in organic syntheses as an intermediate step in converting olefinic hydrocarbons to alcohols or alkyl halides.[53-56] In this reaction, borane (commonly diborane or pentaborane) reacts with an alkene through a concerted reaction forming a four-membered-ring transition state and an organoboron intermediate. It is this organoboron intermediate that we hope to stabilize and isolate in order to produce boron nanoparticles coated with organic alkyl groups.

Boron powder was milled with H_2 gas to produce hydrogenated boron particles and to substitute borane compounds as initial reactant. Figure 2.8 displays a plot showing H_2 pressure decrease for a 16-hour milling process. The measured pressure started to plateau after 12 hours of milling time suggesting that the reaction was already complete at that point. To serve as controls, boron was also milled with argon at the same initial charge pressure and H_2 gas was separately milled in a jar containing boron-free tungsten carbide media. This ensured that the pressure drop observed with milling in H_2 gas was due to H_2 adsorbing and reacting with solid boron. A more detailed discussion of the hydrogen loading on boron nanoparticles is presented in Chapter 4 of this manuscript.

Samples of H_2-milled boron were analyzed by FTIR to determine if the process produced boron particles bonded with terminal hydrogen. The spectrum in Figure 2.9a shows a sharp and intense band at 2520 cm^{-1} which is attributed to the B–H stretching vibration,[57] confirming the reaction of H_2 with powdered boron. Also, broad bands were observed at

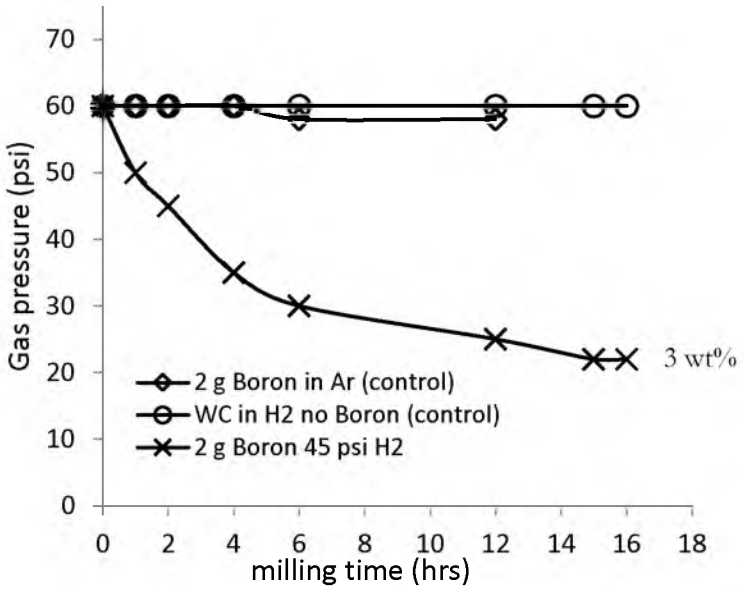

Figure 2.8 H_2 gas pressure drop inside WC jar measured throughout the milling process.

the 3000 – 3400 cm^{-1} and 1350 cm^{-1} for νO–H and νB–O vibrations, respectively. The presence of these IR bands indicates that the boron particles are susceptible to oxidation when exposed to air before and during IR analysis.

Dry milled boron in H_2 atmosphere was then milled with 1-octene to drive the reaction of the alkene and the "surface borane" producing an alkylated boron particle. A slower milling rate was used for the ligand milling stage to minimize further grinding and crushing of boron particles, which could result in exposure of more unoxidized boron atoms that will no longer be hydrogenated. These unoxidized boron atoms will not react with 1-octene during ligand milling and will only be susceptible to oxidation in air. After 12 hours of milling at 100 rpm, a thick mixture of boron particles in 1-octene was obtained. The particles were then suspended in hexane by sonication.

Figures 2.9b and c compare the IR spectra of neat 1-octene and H-terminated boron nanoparticles milled with 1-octene. For 1-octene, stretching bands were observed at 3078

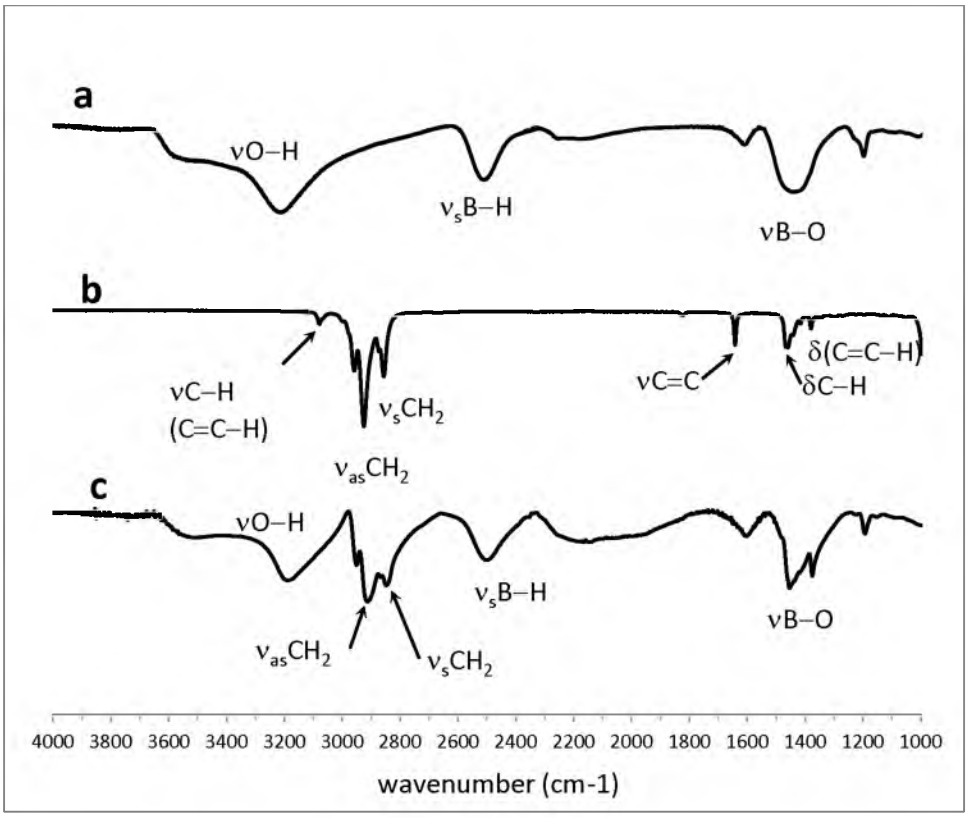

Figure 2.9 FTIR spectra of **(a)** boron milled with H_2, **(b)** neat 1-octene, and **(c)** H-terminated boron nanoparticles milled with 1-octene.

cm^{-1}, 2958 cm^{-1}, 2856 cm^{-1}, and 1641 cm^{-1} corresponding to alkenyl C–H, asymmetric and symmetric CH_2, and C=C vibrations, respectively. C–H bending modes were also observed for alkyl (1460 cm^{-1}) and alkenyl (906 cm^{-1}) groups. Interestingly, after milling with H-terminated boron, the C–H stretching and bending modes of the olefin group disappeared together with the C=C stretching band, suggesting interaction of octene with boron. Furthermore, the shift of the CH_2 asymmetric and symmetric stretches to a lower wavenumber indicate that the alkyl chain was adsorbed on the surface of the nanoparticle. The presence of the B–H stretching band after octene reaction indicates that the H-terminated boron surface did not react completely with octene. One possible explanation for this is the inability of 1-octene molecules to access these sites due to steric hindrance.

Nonetheless, we demonstrated that alkenes can be used to functionalize boron nanoparticles with long chain alkyl groups provided the boron surface was hydrogenated.

Oxidation state of the particles produced through hydrogenation and functionalization of octene was also analyzed using XPS. Figure 2.10 displays the B 1s spectra of boron particles dry milled in H_2 (top) and then milled with 1-octene (middle), compared with particles milled in Ar and then in octene (bottom). Boron milled with H_2 showed significant oxidation upon exposure to air which was also seen in the FTIR results. This is not surprising since surface hydrogenation has not been shown to protect metals from oxidation in air.[58-59] However, the

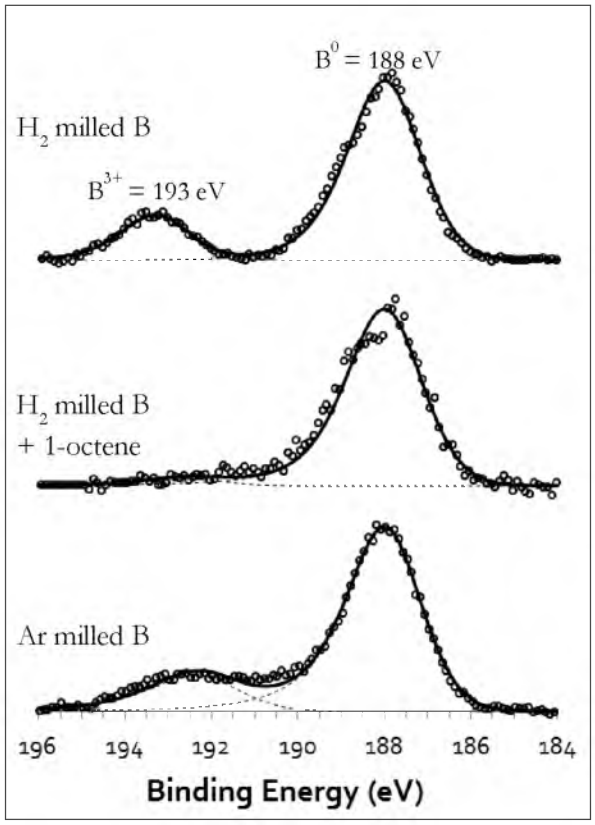

Figure 2.10 B 1s X-ray photoelectron spectra of boron milled with $H_{2(g)}$ (top) and then milled with 1-octene (middle) compared with boron milled in Ar and then in octene (bottom). Samples were exposed to air prior to analysis.

intensity of the oxide peak in this sample was significantly higher than the oxide typically observed for dry milled samples.[1] A possible explanation for this is that dry milling in reactive H_2 atmosphere produced smaller particles than milling in inert atmosphere (Ar or N_2), since the presence of hydrogen on the surface of the particles could prevent cold welding during the milling process. SEM micrograph of particles milled in H_2 showed more particles with smaller size and rougher, irregular surfaces are formed as compared to those milled in Ar (See Chapter 4). Interestingly, milling with 1-octene promoted protection against air oxidation of these particles. Figure 2.10 (middle spectrum) shows that the oxide was decreased from 20 % to 4 % with the presence of the octyl group on the particle surface, whereas a higher percentage of oxide is observed for boron sample milled in Ar and octene. This suggests that although octene interacts with boron, most likely through its double bond, the interaction is weak and octene is easily washed away when sonicated in hexane. Furthermore, these particles show a high tendency to aggregate and settle down in hexane suggesting that the particles are not effectively functionalized with the hydrophobic ligand (Appendix A).

2.5 Conclusion

Synthesis of boron nanoparticles coated with oleic acid ligand was successfully scaled up and modified to suit a large-capacity planetary ball mill. Boron nanoparticles were characterized for particle size and oxidation state. Results show that although the planetary ball mill is less powerful than the previously used shaker mill, sub-100 nm size particles can still be achieved by properly adjusting milling conditions and procedures. Here, a three-step milling process composed of dry milling, ligand milling, and solvent milling was developed. Similarly, XPS studies on nanoparticles produced through this procedure showed that boron was unoxidized and is protected from air oxidation. Characterization of the oleic acid ligand

using FTIR, and ^{13}C-NMR confirmed our initial hypothesis that oleic acid binds through the reactive oxygen of the carboxylate group as an oleate species. FTIR results suggest a bridging bidentate interaction where the two oxygen atoms of a single oleate ion bind to two separate boron atoms on the surface. Furthermore, the presence of undissociated oleic acid molecules despite thorough washing suggests that both oleic acid and oleate species were adsorbed on the surface of the particles with the free oleic acid molecules probably held strongly by intercalating between covalently bonded oleate through H-bonding of the polar heads and van der Waals interactions of the hydrophobic tails.

Milling boron powder in a H_2 atmosphere showed great promise as an intermediate step in functionalizing boron nanoparticles with alkyl groups. Hydrogenated boron surfaces were produced through milling which were then reacted with a terminal alkene. IR analysis confirmed the reaction of 1-octene while XPS showed that it can protect boron from air oxidation. This process has great potential in introducing organic ligands that are inherently unreactive to the boron surface, opening a wider range of possible applications for boron nanoparticles.

2.6 References

(1) Van Devener, B.; Perez, J. P. L.; Jankovich, J.; Anderson, S. L. Oxide-Free, Catalyst-Coated, Fuel-Soluble, Air-Stable Boron Nanopowder as Combined Combustion Catalyst and High Energy Density Fuel. *Energy Fuels* **2009,** *23*, 6111-6120.

(2) Linstrom, P. J.; Mallard, W. G. *Nist Chemistry Webbook, Nist Standard Reference Database Number 69*. National Institute of Standards and Technology: Gaithersburg MD, 20899, 2011.

(3) Shen, D.; Yu, X.; Guo, Y.; Wang, S.; Deng, T. Boron and Its Compounds in New Energy and Materials Fields. *App. Mech. Mat.* **2011,** *71-78*, 2594-2597.

(4) Nerad, A. J.; Hurd, D. T. *Fuel Compositions*. US 1948-62786 U.S. Patent 2894830, July 14, **1959**.

(5) Shore, S. G. *Story of the Diammoniate of Diborane and the Related Compound Ammonia Borane*. In *ACS National Meeting*, American Chemical Society: Washington, DC, 2009; Vol. Fuel, p 135.

(6) Sanders, R. N. *High-Energy Fuel Comprising Beryllium Hydride and Pentaborane*. US 1968-752731 U. S. Patent 3578516, May 11, **1971**.

(7) Kendrick, T. R., III; Eads, D. K.; Wagner, J. W. *Boron-Containing Fuels*. US 1958-716514 U.S. Patent 3135802, June 2, **1964**.

(8) Kurz, P. F. Selective Combustion in Propane-Diborane Flames. *Fuel* **1954,** *33*, 250-251.

(9) Parker, W. G.; Wolfhard, H. G. Properties of Diborane Flames. *Fuel* **1956,** *35*, 323-332.

(10) Shafirovich, E. Y.; Goldshleger, U. I. Comparison of Potential Fuels for Martian Rockets Using Co_2. *J. Propul. Power* **1997,** *13*, 395-397.

(11) Whittaker, M. L.; Cutler, R. A.; Anderson, P. E. *Boride-Based Materials for Energetic Applications*, MRS Online Proceedings Library, 2011.

(12) Wong, S. C.; Lin, A. C.; Wu, C. E. Microexplosions of Boron and Boron/Carbon Slurry Droplets. *Combust. Flame* **1994,** *96*, 304-310.

(13) Liehmann, W. *Combustion of Boron-Based Slurries in a Ramburner*, International Annual Conference of ICT, Pfinztal, Germany, 1991; pp 97/1-97/8.

(14) Takahashi, F.; Heilweil, I. J.; Dryer, F. L. Disruptive Burning Mechanism of Free Slurry Droplets. *Combust. Sci. Technol.* **1989,** *65*, 151-165.

(15) Glassman, I.; Dryer, F. L.; Williams, F. A. *Fuels Combustion Research*; Department of Mechanical and Aerospace Engineering, Princeton University, Princeton, NJ: 1988.

(16) Hensel, C.; Clezkl, H. *Spectroscopic Studies on the Combustion Behavior of Htpb and Gap Plates with Boron Additive in a Level Stage Combustion Chamber*, Fraunhofer-Institut fuer Chemische Technologie: 1995.

(17) Natan, B.; Gany, A. Combustion Characteristics of a Boron-Fueled Solid Fuel Ramjet with Aft-Burner. *J. Propul. Power* **1993,** *9*, 694-701.

(18) Glassman, I.; Williams, F. A.; Antaki, P. *A Physical and Chemical Interpretation of Boron Particle Combustion*, 20th Symposium (International) on Combustion, The Combustion Institute: 1985; pp 2057-2064.

(19) Hsia, H. T.-S. *Air-Augmented Combustion of Boron and Boron-Metal Alloys*; Air Force Rocket Propulsion Laboratory, Air Force Systems Command, United States Air Force: Edwards, CA, 1971.

(20) Natan, B.; Netzer, D. W. Boron Carbide Combustion in Solid-Fuel Ramjets Using Bypass Air. Part 2. Theoretical Analysis. *Propell. Explos. Pyrot.* **1997,** *22*, 6-10.

(21) Macek, A.; Semple, J. M. *Combustion of Boron Carbide Particles*; Atlantic Research Division: Alexandria, VA, 1971; p 23.

(22) Mota, J. M.; Abenojar, J.; Martinez, M. A.; Velasco, F.; Criado, A. J. Borides and Vitreous Compounds Sintered as High-Energy Fuels. *J. Solid State Chem.* **2004,** *177*, 619-627.

(23) Nabity, J. A.; Ho Lee, T.; Natan, B.; Netzer, D. W. *Combustion Behavior of Boron Carbide Fuel in Solid Ramjets*. In *Combustion of Boron-Based Solid Propellants and Solid Fuels*, Kuo, K. K., Ed. Boca Raton, Fla, 1993; pp 287-302.

(24) Natan, B.; Netzer, D. W. Boron Carbide Combustion in Solid-Fuel Ramjets Using Bypass Air. Part 1. Experimental Investigation. *Propell. Explos. Pyrot.* **1996,** *21*, 289-294.

(25) Plantier, K. B.; Pantoya, M. L.; Gash, A. E. Combustion Wave Speeds of Nanocomposite Al/Fe_2O_3: The Effects of Fe_2O_3 Particle Synthesis Technique *Combustion and Flame* **2005,** *140*, 299-309.

(26) Jain, A.; Anthonysamy, S.; Ananthasivan, K.; Gupta, G. S. Studies on the Ignition Behaviour of Boron Powder. *Thermochim. Acta* **2010,** *500*, 63-68.

(27) Bellott, B. J.; Noh, W.; Nuzzo, R. G.; Girolami, G. S. Nanoenergetic Materials: Boron Nanoparticles from the Pyrolysis of Decaborane and Their Functionalisation. *Chem. Commun.* **2009**, 3214-3215.

(28) Casey, J. D.; Haggerty, J. S. Laser-Induced Vapor-Phase Syntheses of Boron and Titanium Diboride Powders. *J. Mat. Sci.* **1987,** *22*, 737-744.

(29) Pickering, A. L.; Mitterbauer, C.; Browning, N. D.; Kauzlarich, S. M.; Power, P. P. Room Temperature Synthesis of Surface-Functionalized Boron Nanoparticles. *Chem. Commun.* **2007**, 580-582.

(30) Si, P. Z.; Zhang, M.; You, C. Y.; Geng, D. Y.; Du, J. H.; Zhao, X. G.; Ma, X. L.; Zhang, Z. D. Amorphous Boron Nanoparticles and Bn Encapsulating Boron Nano-Peanuts Prepared by Arc-Decomposing Diborane and Nitriding. *J. Mat. Sci.* **2003,** *38*, 689-692.

(31) Suryanarayana, C. *Mechanical Alloying and Milling*. Vol. 46, p 1-184 Marcel Dekker: New York, 2001.

(32) Suryanarayana, C. Mechanical Alloying and Milling. *Prog. Mater Sci.* **2001,** *46*, 1-184.

(33) Wagner, C. D.; Naumkin, A. V.; Kraut-Vass, A.; Allison, J. W.; Powell, C. J.; John R. Rumble, J. *Nist X-Ray Photoelectron Spectroscopy Database* June 6, 2000 ed.; Measurement Services Division of the National Institute of Standards and Technology (NIST) Material Measurement Laboratory (MML): 2007.

(34) Carpenter, E. E., Calvin, S., Stroud, R.M. and Harris, V.G. Passivated Iron as Core-Shell Nanoparticles. *Chem. Mater.* **2003,** *15*, 3245-3246.

(35) Wu, N.; Fu, L.; Su, M.; Aslam, M.; Wong, K. C.; Dravid, V. P. Interaction of Fatty Acid Monolayers with Cobalt Nanoparticles *Nano Lett.* **2004,** *4*, 383-386.

(36) Yang, H. T.; Shen., C. M.; Wang, Y. G.; Su, Y. K.; Yang, T. Z.; H.G., G. Stable Cobalt Nanoparticles Passivated with Oleic Acid and Triphenylphosphine. *Nanotechnology* **2004,** *15*, 70-74.

(37) De la Presa, P.; Multigner, M.; De la Venta, J.; Garcia, M. A.; Ruiz-Gonzalez, M. L. Structural and Magnetic Characterization of Oleic Acid and Oleylamine-Capped Gold Nanoparticles. *J. Appl. Phys.* **2006,** *100*, 123915/1- 123915/6.

(38) Xu, F.; Zhang, Q.; Gao, Z. Simple One-Step Synthesis of Gold Nanoparticles with Controlled Size Using Cationic Gemini Surfactants as Ligands: Effect of the Variations in Concentrations and Tail Lengths. *Colloids Surf., A* **2013,** *417*, 201-210.

(39) Husein, M. M.; Rodil, E.; Vera, J. H. Preparation of Agbr Nanoparticles in Microemulsions Via Reaction of Agno3 with Ctab Counterion. *J. Nanopart. Res.* **2007,** *9*, 787-796.

(40) Lisiecki, I. Size, Shape, and Structural Control of Metallic Nanocrystals. *J. Phys. Chem. B* **2005,** *109*, 12231-12244.

(41) Dubois, L. H.; Zegarski, B. R.; Nuzzo, R. G. Spontaneous Organization of Carboxylic Acid Monolayer Assembly Via Gas-Phase Adsorption Films in Ultrahigh Vacuum. Kinetic Constraints To. *Langmuir* **1986,** *2*, 412-417.

(42) Zhang, L.; He, R.; Gu, H.-C. Oleic Acid Coating on the Monodisperse Magnetite Nanoparticles. *Appl. Surf. Sci.* **2006,** *253*, 2611-2617.

(43) Nakamoto, K. *Infrared and Raman Spectra of Inorganic and Coordination Compounds*. Vol. p John Wiley and Sons: New York, 1997.

(44) Simon-Kutscher, J.; Gericke, A.; Hühnerfuss, H. Effect of Bivalent Ba, Cu, Ni, and Zn Cations on the Structure of Octadecanoic Acid Monolayers at the Air-Water Interface as Determined by External Infrared Reflection-Absorption Spectroscopy. *Langmuir* **1996,** *12*, 1027-1034.

(45) Ren, Y.; Iimura, K.-i.; Kato, T. Structure of Barium Stearate Films at the Air/Water Interface Investigated by Polarization Modulation Infrared Spectroscopy and *Π–a* Isotherms. *Langmuir* **2001,** *17*, 2688-2693.

(46) Horchani, H.; Chaâbouni, M.; Gargouri, Y.; Sayari, A. Solvent-Free Lipase-Catalyzed Synthesis of Long-Chain Starch Esters Using Microwave Heating: Optimization by Response Surface Methodology. *Carbohydr. Polym.* **2010,** *79*, 466-474.

(47) Abraham, A.; Mihaliuk, E.; Kumar, B.; Legleiter, J.; Gullion, T. Solid-State Nmr Study of Cysteine on Gold Nanoparticles. *Journal of Physical Chemistry C* **2010,** *114*, 18109.

(48) Badia, A.; Demers, L.; Dickinson, L.; Morin, F. G.; Lennox, R. B.; Reven, L. Gold-Sulfur Interactions in Alkylthiol Self-Assembled Monolayers Formed on Gold Nanoparticles Studied by Solid-State Nmr. *J. Am. Chem. Soc.* **1997,** *119*, 11104-11105.

(49) Badia, A.; Gao, W.; Singh, S.; Demers, L.; Cuccia, L.; Reven, L. Structure and Chain Dynamics of Alkanethiol-Capped Gold Colloids. *Langmuir* **1996,** *12*, 1262.

(50) Abraham, A.; Ilott, A. J.; Miller, J.; Gullion, T. (1)H Mas Nmr Study of Cysteine-Coated Gold Nanoparticles. *J. Phys. Chem. B* **2012**.

(51) Rubio, J.; Izquierdo, M. A.; Burguete, M. I.; Galindo, F.; Luis, S. V. Photoluminescence of Cdse/Zns Core-Shell Quantum Dots Stabilized in Water with a Pseudopeptidic Gemini Surfactant. *Nanoscale* **2011,** *3*, 3613-5.

(52) Sperling, R. A.; Parak, W. J. Surface Modification, Functionalization and Bioconjugation of Colloidal Inorganic Nanoparticles. *Philos Transact A Math Phys Eng Sci* **2010,** *368*, 1333-83.

(53) Renaud, P.; Beauseigneur, A.; Brecht-Forster, A.; Becattini, B.; Darmency, V.; Kandhasamy, S.; Montermini, F.; Ollivier, C.; Panchaud, P.; Pozzi, D.; Scanlan, E. M.; Schaffner, A.-P.; Weber, V. Boron: A Key Element in Radical Reactions. *Pure Appl. Chem.* **2007,** *79*, 223-233.

(54) Fu, G. C. Metal-Catalyzed Hydroboration Reactions. *Transition Metals for Organic Synthesis* **1998,** *2*, 141-146.

(55) Beckett, M. A. Boron. *Annu. Rep. Prog. Chem. Sect. A: Inorg. Chem.* **1994,** *90*, 3-24.

(56) Devaprabhakara, D.; Sethi, D. S. Recent Progress in the Hydroboration Reactions. *J. Sci. Ind. Res.* **1970,** *29*, 280-292.

(57) Chin, T. T.; Lovelace, S. R.; Geiger, W. E.; Davis, C. M.; Grimes, R. N. Infrared Spectroelectrochemistry of Boron-Hydrogen Stretches: A Tool for Diagnosis of

Delocalization in Mixed-Valent Metallacarborane Complexes. *J. Am. Chem. Soc.* **1994,** *116*, 9359-9360.

(58) Hattori, T.; Nohira, H. *Springer Series in Materials Science* **2001,** *46*, 61-88.

(59) Niwano, M.; Kageyama, J.-i.; Kinashi, K.; Sawahata, J.-i.; Miyamoto, N. Oxidation of Hydrogen-Terminated Si Surfaces Studied by Infrared Spectroscopy. *Surf. Sci.* **1994,** *301*, L245–L249.

CHAPTER 3

EXPLORING THE STRUCTURE OF NITROGEN-RICH IONIC LIQUIDS AND THEIR BINDING TO THE SURFACE OF OXIDE-FREE BORON NANOPARTICLES

THE JOURNAL OF PHYSICAL CHEMISTRY C

Article

pubs.acs.org/JPCC

Exploring the Structure of Nitrogen-Rich Ionic Liquids and Their Binding to the Surface of Oxide-Free Boron Nanoparticles

Jesus Paulo L. Perez,[†] Brandon W. McMahon,[†] Stefan Schneider,[‡,∥] Jerry A. Boatz,[‡,∥] Tom W. Hawkins,[‡,∥] Parker D. McCrary,[§] Preston A. Beasley,[§] Steven P. Kelley,[§] Robin D. Rogers,[§,∥] and Scott L. Anderson[†,∥,*]

[†]Department of Chemistry, University of Utah, 315 South 1400 East, Salt Lake City, Utah 84112, United States

[‡]Propellants Branch, Rocket Propulsion Division, Aerospace Systems Directorate, Air Force Research Laboratory, AFMC AFRL/RQRP, 10 East Saturn Boulevard, Edwards AFB, California 93524, United States

[§]Center for Green Manufacturing and Department of Chemistry, The University of Alabama, Tuscaloosa, Alabama 35487, United States

Supporting Information

ABSTRACT: The structure of two different energetic ionic liquids and the nature of their binding to elemental boron surfaces were investigated by a combination of X-ray photoelectron spectroscopy, IR spectroscopy, zeta potential measurements, thermogravimetric analysis, and first-principles theory. It was found that both 1-methyl-4-amino-1,2,4-triazolium dicyanamide ([MAT][DCA]) and 1-butyl-3-methylimidazolium dicyanamide ([BMIM][DCA]) ionic liquids bind to boron well enough to resist removal by ultrasonic washing and to protect the boron surface from oxidation during air exposure of the washed powder. The data suggest that both the cation and the anion of the ionic liquids interact with the boron surface; however, for [MAT][DCA], the interaction of the cation appears to dominate, while for [BMIM][DCA] the interaction with the $[DCA]^-$ anion dominates. The difference is attributed to the binding of boron to the amino group of $[MAT]^+$, and the amino group also appears to help bind a thicker ionic liquid (IL) capping layer.

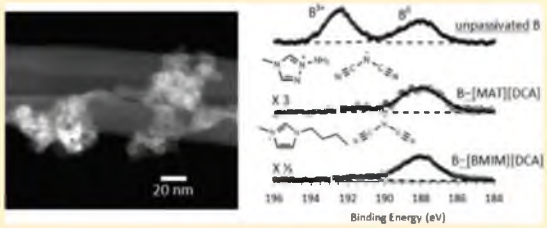

I. INTRODUCTION

Hydrazine and its derivatives are widely employed as propellants in rocket engines for spacecraft station keeping, orbit maneuvering, and orientation control applications. A typical bipropellant rocket engine might use a hydrazine compound as fuel and nitrogen tetroxide (NTO) as oxidizer.[1] The fact that such mixtures are hypergolic (i.e., they spontaneously ignite upon mixing) has important advantages in propulsion applications; however, hydrazine and its derivatives have serious disadvantages, including high vapor pressure with toxic[2,3] and flammable vapors and relatively low energy density.[1,2] Ionic liquids (ILs), now defined as salts with melting point below 100 °C, can have low or negligible vapor pressures, and the wide variety of cations and anions available make it possible to tune the properties for a wide variety of applications.[4−10] The discovery of ILs with hypergolic properties opened the possibility of using them as low vapor pressure, safer rocket propellants.[11−15] Throughout the years, researchers at the Air Force Research Laboratory (AFRL) have synthesized hypergolic ILs, focusing on imidazolium-based cations for their stability in air and also for high nitrogen content and dicyanamide[12,13,15] and dicyanoborate[16] anions for lower viscosity[17,18] and better ignition delay properties, respectively. Also, such propellants can potentially have significantly higher energy density than those of hydrazine and its derivatives. Shreeve et al. synthesized a number of highly energetic ionic liquids with multiple nitrogen atoms in their structures,[18−23] in the hope of increasing volumetric and gravimetric energy density by introducing multiple nitrogen atoms and more nitrogen−nitrogen bonds.[24−27] In lieu of this, azolium azolate ILs, salts with both cation and anion composed of heterocyclic organic ions, are now being considered as the next stage in IL propellant development, although their hypergolic property is yet to be demonstrated.[28−34] A more detailed review of some of the considerations involved in developing IL propellants is given in the Supporting Information (SI).

In addition to developing improved ILs, another approach to increase energy density is adding high energy density nanoparticles to the IL propellant. Boron has both gravimetric (59.0 MJ/kg) and volumetric (137.8 MJ/L) energy densities[35] that are far higher than those for typical hydrocarbons (35−40 MJ/L or kg) and significantly higher than those of other active metal fuels such as aluminum (31.0 MJ/kg, 83.8 MJ/L)[35] or magnesium (24.0 MJ/kg, 43.0 MJ/L).[35] Therefore, boron

Received: October 10, 2012
Revised: January 28, 2013
Published: January 29, 2013

dx.doi.org/10.1021/jp3100409 | J. Phys. Chem. C 2013, 117, 5693−5707

nanoparticles have attracted significant interest as additives to liquid fuels and propellants.[36−43]

Boron's potential as a high energy fuel additive is impeded by its high vaporization temperature, which results in oxidation being a heterogeneous process, and thus limited by the diffusion of reactants and products to and from the interface. Furthermore, boron, like most active metals, develops a thin, passivating oxide layer upon air exposure, and this oxide layer inhibits ignition under combustion conditions.[37,38] Using boron in the form of well-dispersed nanoparticles increases the surface area and mitigates the diffusion limitation; however, the oxide layer still inhibits particle ignition and also makes up an increasing fraction of the particle mass as the dimension is reduced.[41] Therefore, a possible strategy for improving the ignition properties of boron (or any metal particle) is to cap the nanoparticles with chemical agents that prevent formation of the passivating oxide layer and also render the particles highly dispersible in the fuel of interest.[44,45]

We have previously shown that unoxidized, air-stable boron nanoparticles capped with oleic acid can be synthesized by ball milling and are highly dispersible in hydrocarbon fuels.[44,45] The oleic acid layer is expected to desorb or oxidize at relatively low temperatures, allowing ignition of the underlying unoxidized boron. Also, we recently demonstrated that a similar approach can be used to generate unoxidized and air-stable boron nanoparticles by capping with a hypergolic IL, [MAT][DCA].[46] Additionally, these boron nanoparticles do not inhibit hypergolic ignition of the IL with nitric acid.[47]

An important issue in generalizing this result to other ILs or other metals is the lack of understanding of the nature of the IL−boron bonding. This information would also be useful in understanding issues like IL storability and stability in contact with metals. In this paper, we report the spectroscopic studies on neat [MAT][DCA] and [BMIM][DCA] ILs, as well as their interactions with boron surfaces. In addition, light scattering, thermogravimetric, and quantum chemistry techniques were utilized to probe the boron−IL systems.

II. EXPERIMENTAL AND COMPUTATIONAL METHODOLOGY

A. Boron Milling Process. Boron powder (97%, ~2 μm nominal particle size) from C.R. Supply Co. (West Hills, CA) was used as starting material in the milling process. The [MAT][DCA] and [MAT]I ILs used were synthesized at the Air Force Research Laboratory (AFRL) at Edwards AFB, using procedures described elsewhere.[13] [BMIM]Cl was synthesized through a neat quaternatization reaction between 1-methylimidazole, redistilled prior to use, and 1-chlorobutane, which were purchased from Sigma-Aldrich (St. Louis, MO). [BMIM][DCA] and Na[DCA] were purchased from Sigma Aldrich and used as received. Ethanol (200 proof) and acetonitrile (99.5%) solvents were purchased from PharmCo-Aaper Products Inc. (Brooksfield, CT) and Macron, Inc. (San Antonio, TX), respectively. Air-sensitive reagents were handled and stored in a N_2-filled glovebox. Particle size reduction was done using a small-scale shaker mill (Spex, (Metuchen, NJ) Certiprep 8000 model) using a 55-mL tungsten carbide-lined milling jar with tungsten carbide media, following a procedure described previously[46] and summarized here. A two-stage milling process was employed. First, 1.0 g of boron was dry milled with 80.0 g of 1/8 inch tungsten carbide balls for one hour. To avoid possible reaction of boron with nitrogen under milling conditions, the dry milling was done under Ar atmosphere by loading and sealing the jar in an Ar-filled glovebox. This "dry milling" process accomplishes part of the particle size reduction and thereby produces a substantial area of fresh unoxidized boron surface that is highly reactive. At this point, the jar was opened, and 10.0 mL of the IL was added prior to milling for an additional three hours. After milling, the boron/IL mixture was scraped out of the jar and washed off the balls using ethanol as solvent. Opening and closing of the milling jar for addition of reagents were done inside the Ar-filled glovebox.

Hazards. Unpassivated boron nanoparticles are highly pyrophoric, and exposure to air leads to spontaneous ignition, which can be violent for dry particles. Ignition can occur after a substantial delay if the particles are wet at the time of exposure. While the milling procedures described produce air-stable boron nanoparticles, as a safety measure we always treat the particles as if they are pyrophoric until they have been proven to be air-stable by testing on small samples. In addition, any materials such as solvents, paper towels, sample bottles, etc. that have been in contact with boron nanoparticles must be treated as potentially pyrophoric. Before disposing such potentially contaminated items, they were exposed to air in a fume hood for several days to ensure time for oxygen to diffuse and react with any unpassivated boron present.

B. Size Characterization. Particle size and size distributions were analyzed using scanning electron microscopy (SEM-FEI Nova Nano 600, Hillsboro, OR) and dynamic light scattering (DLS—Wyatt DynaPro NanoStar, Wyatt Technology, Dernbach, Germany), respectively. Samples for SEM were washed by sonicating the particles with ethanol and centrifuging. The centrifuged particles were redispersed in fresh ethanol, and the process was repeated for a total of three washings to remove any ILs that are not bound to the particle surface, as these tend to cause adverse charging artifacts during SEM analysis. Washed particles were diluted with ethanol, then drop casted and dried on a transmission electron microscopy (TEM) grid, and affixed on a SEM aluminum stub using carbon tape. DLS analysis was done on washed samples diluted and dispersed in ethanol.

C. X-ray Photoelectron Spectroscopy (XPS). XPS analyses were done using a Kratos Axis Ultra instrument (Chestnut Ridge, NY). For XPS of the ionic liquid itself, a drop of neat [MAT][DCA] or [BMIM][DCA] was placed in a shallow well, machined in an aluminum sample holder fabricated to handle liquid samples. The sample-containing well was clamped on a Kratos sample bar and placed inside the load lock of the instrument and evacuated before transfer into the ultrahigh vacuum (UHV) system. The vapor pressures of both ILs are low enough that no significant pressure rise was observed after introduction of the IL samples. For boron samples, XPS was done on as-milled nanoparticles in excess IL and also on boron recovered at various stages of the ethanol washing process, described above. The washed samples were dried in air overnight to evaporate ethanol and then pressed onto a carbon tape atop a copper shim, prior to introduction into the XPS instrument's vacuum system.

X-ray photoelectron spectra were taken using the monochromatic Al Kα source (1486.7 eV) at a 300 × 700 μm spot size. Low-resolution survey and high-resolution region scans were taken for each sample. To minimize charging, samples were flooded with low-energy electrons and ions from the instrument's built-in charge neutralizer. Data were analyzed using CASA XPS software, and energy corrections on high-resolution scans were done by referencing the C 1s peak of

dx.doi.org/10.1021/jp3100409 | J. Phys. Chem. C 2013, 117, 5693−5707

adventitious carbon to 284.5 eV.[48] As shown below, this energy referencing method gives literature-consistent binding energies for boron as well.

D. Fourier Transform Infrared (FTIR) Spectroscopy. Infrared (IR) spectra were collected using a Bruker (Madison, WI) platinum α-FTIR by direct measurement via attenuated total reflectance of samples on a diamond crystal. Solid nanoparticulate samples were washed with ethanol to remove unbound ILs, air-dried, and then pressed onto a diamond crystal with a Platinum ATR QuickSnap sampling module. Spectra were acquired with resolution of 1 cm^{-1} in 10 independent scans and then averaged.

E. Zeta Potential Measurements. Zeta potentials were measured using a Particle Sizing Systems NICOMP 380 instrument (Santa Barbara, CA). Dried, ethanol-washed boron nanoparticles were dispersed in acetonitrile (Macron Chemicals, San Antonio, TX, 99.8%). Acetonitrile was used as solvent to eliminate any possibility of hydrolysis of ethanol or water on the boron nanoparticle surface. Measurements were made at three different applied potentials (5, 10, and 15 mV/cm^2), and because the zeta potentials were independent of the applied potential within the uncertainty, the values were averaged. The calibration of the NICOMP instrument was checked by measuring the zeta potential of a zeta potential standard sample, which was also measured on a Zetasizer Nano Z instrument (Malvern Instruments Ltd., Worcestire, UK).

F. Thermogravimetric Analysis (TGA). A TGA 2950 Thermogravimetric Analyzer (TA Instruments, New Castle, DE) was used to measure mass changes occurring during heating of the ILs and IL-functionalized boron. Neat ILs were run at a temperature ramp rate of 20 °C/min from 35 to 800 °C under O_2. Boron samples were run at a slower ramp rate of 5 °C/min from 35 to 900 °C also under O_2 atmosphere. The slower ramp rate and increased range for boron nanoparticles were used because full oxidation of the solid samples is expected to be limited by diffusion of oxygen through the boron oxide layer that initially forms as the IL is desorbed/decomposed.

G. Core-Level Binding Energies and Charge Distribution Calculations. Density functional theory (DFT) calculations were performed using the revised Tao–Perdew–Staroverov–Scuseria (revTPSS) meta-generalized gradient approximation (meta-GGA) functional[49] and the 6-311++G(d,p) basis set.[50−52] All structures were fully optimized and verified as local minima by confirming that the Hessian matrix is positive definite, i.e., that the calculated harmonic vibrational frequencies are all real. All calculations were performed using the GAMESS[53,54] quantum chemistry package. Calculated core level orbital energies were used as an approximation of the binding energies to be expected for ionizing out those levels. Because this approximation (Koopmans' theorem: binding energy = −orbital energy)[55] neglects relaxation and screening, the orbital energies differ substantially from the experimental binding energies. Differences between orbital energies for different atomic centers are, however, expected to mirror the differences in measured binding energies. For the comparisons given below, the Koopmans' theorem binding energies were shifted to bring the calculated and experimental binding energies for the most strongly bound orbital into agreement but were not scaled or otherwise corrected.

III. RESULTS AND DISCUSSION

The ultimate goal of this study is to understand how the two ILs form dense, solvent-resistant passivating layers on boron; however, interpreting the spectroscopic data regarding IL–boron binding requires that we first understand the spectroscopic signature of the ionic liquids. The results are interesting in themselves, because they provide insight into the structure and charge distributions in the neat ILs.

A. XPS Analysis of Liquid [MAT][DCA] and [BMIM][DCA]. A number of researchers have taken advantage of the low vapor pressure of ILs to measure the C 1s, N 1s, O 1s, and S 2p X-ray photoelectron spectra (XPS) of various ILs, correlating the observed core level binding energies to the ILs' structures.[56−60] These analyses relied on binding energy values from other compounds with fragments that were isostructural to the ILs studied. Here we took advantage of the fact that the XPS for the ILs of interest show considerable structure that could be compared to ab initio theory to make assignments. The assignments were confirmed by reference studies on salts containing either the cation or anion of interest. For instance, 1-methyl-4-amino-1,2,4-triazolium iodide ([MAT]I) and 1-butyl-3-methyl-imidazolium chloride ([BMIM]Cl) were used as references to identify the N 1s and C 1s XPS signals coming from $[MAT]^+$ and $[BMIM]^+$ cations, respectively, while sodium dicyanamide (Na[DCA]) was used for the $[DCA]^-$ anion.

Figure 1a shows the high-resolution N 1s spectra for [MAT]I (broken line) and Na[DCA] (solid line) plotted together to allow direct comparison with the N 1s spectrum for the [MAT][DCA] IL (Figure 1b). The $[MAT]^+$ cation has four N atoms, all of which are unique and distinguishable, at least in principle. The $[DCA]^-$ anion has a central N atom and a pair of terminal N atoms that are equivalent at least in the isolated anion. This equivalence results in exact overlaying of the two fit components that make up the terminal N peak. The structures of the cations and anions and the labels used for the different N atoms are shown in Figure 1e. The spectra were fit by assuming that there should be four component peaks for [MAT]I and three for Na[DCA] (with the two N_{DT} atoms being identical), each with the same integrated intensity. The peak positions and widths of the fit components were allowed to be freely adjustable, resulting in excellent fits. The best-fit widths of the components are all about the same, with the exception of that for N_{DC} (the central N atom in $[DCA]^-$), which is best fit with a somewhat narrower peak indicating a more homogeneous environment for the central N atom. It is clear from these spectra that the four N atoms in $[MAT]^+$ have higher N 1s binding energies than any of the N atoms in $[DCA]^-$, which is consistent with the usual idea that positively charged centers should have chemical shifts to higher binding energies, while negatively charged centers should have chemical shifts to lower binding energies.

In the case of $[DCA]^-$, symmetry allows assignment of the weaker peak at 399.6 eV to the central N atom (N_{DC}) and the stronger peak (twice the integrated intensity) at 398.3 eV to the two terminal N atoms (N_{DT}). The implication is that the negative charge on the anion is largely distributed between the nitrile groups, leaving the central N atom with a smaller negative charge than the two terminal N atoms. For $[MAT]^+$, the four N atoms clearly fall into two distinct pairs of chemical shifts; however, a more detailed assignment of the individual N atoms to the two spectral features is not possible, a priori.

dx.doi.org/10.1021/jp3100409 | J. Phys. Chem. C 2013, 117, 5693−5707

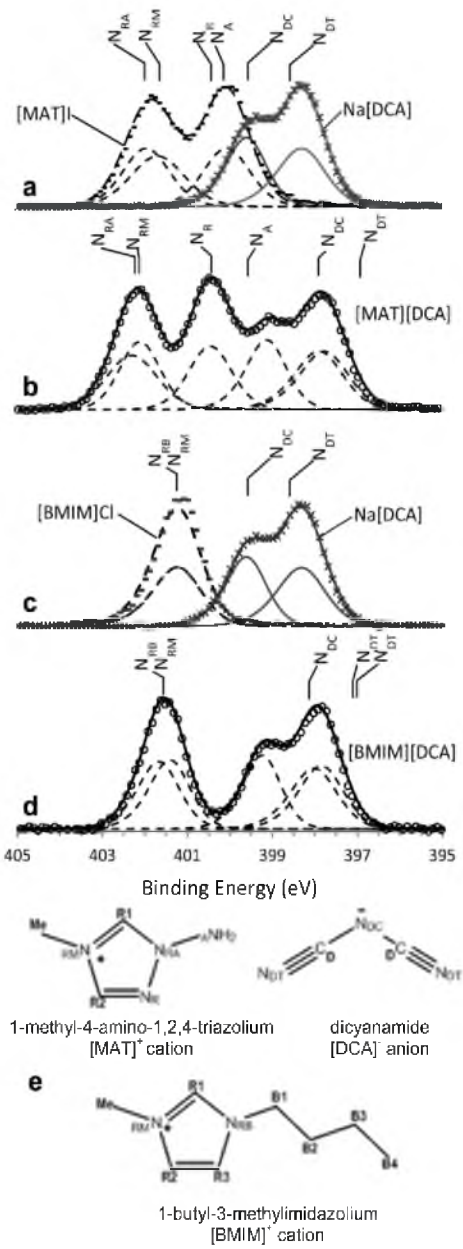

Figure 1. N 1s high-resolution XPS scan of (a) [MAT]I and Na[DCA] (overlapped), (b) [MAT][DCA], (c) [BMIM]Cl and Na[DCA] (overlapped), and (d) [BMIM][DCA]. (e) Chemical structures of the IL cation and anion.

Clearly, the overlapped spectra of [MAT]I and Na[DCA] are quite similar to the N 1s spectrum of neat [MAT][DCA], indicating that local environments around $[MAT]^+$ and $[DCA]^-$ are similar in the IL and in the two salts examined. From the comparison, it is clear that the two higher binding energy peaks at 402 and 400 eV in the spectrum of [MAT][DCA] must correspond to the nitrogen atoms of $[MAT]^+$, while the two low binding energy peaks at 399 and 398 eV must result from $[DCA]^-$. Likewise, the N 1s spectrum of [BMIM][DCA] is well represented by overlapping the spectra of [BMIM]Cl and Na[DCA], making it clear that in the [BMIM][DCA] spectrum (Figure 1d) the two low binding energy peaks come from the three N atoms in $[DCA]^-$, while the high binding N 1s signal at 402 eV must correspond to overlapping contributions from the two N atoms in the $[BMIM]^+$ cation.

To assign the spectra in detail, we carried out DFT calculations on single ion pairs of both ILs and on the reference compounds, [MAT]I, [BMIM]Cl, and Na[DCA], determining N 1s and C 1s core orbital energies and atomic charges. As described above, these were shifted to correct for relaxation and screening effects not included in the calculations and compared with the experimental binding energies. The theoretical N 1s binding energies are indicated in the figure as vertical lines labeled according to the scheme in Figure 1e. Table 1 lists the experimental and theoretical N 1s binding energies for each nitrogen center in the four systems. The agreement between theory and experiment is generally quite good and certainly good enough to assign the spectra unambiguously. The two highest binding energies (~402 eV) are assigned to the ring N atoms in $[MAT]^+$ that have methyl and amino substituents, N_{RM}, and N_{RA}, respectively, while the

Table 1. N 1s Binding Energy Values and Atomic Charges Obtained from XPS and DFT Calculations[a]

nitrogen atom	experimental binding energy (eV)	calculated core energy (eV)	atomic charge[b]
[MAT]I			
N_{RA}	402.0	402.0	−0.04
N_{RM}	401.7	401.8	−0.04
N_R	400.1	400.4	−0.06
N_A	400.1	400.2	−0.16
Na[DCA]			
N_{DC}	399.6	399.6	−0.13
N_{DT1}	398.3	398.6	−0.19
N_{DT2}	398.3	398.6	−0.19
[MAT][DCA]			
N_{RM}	402.3	402.3	0.03
N_{RA}	402.1	402.2	0.03
N_R	400.5	400.4	−0.04
N_A	400.5	399.6	−0.14
N_{DC}	399.1	397.9	−0.14
N_{DT1}	397.9	396.9	−0.25
N_{DT2}	397.7	396.8	−0.27
[BMIM]Cl			
N_{RB}	401.2	401.2	−0.04
N_{RM}	401.2	401.2	−0.04
[BMIM][DCA]			
N_{RB}	401.6	401.6	0.01
N_{RM}	401.4	401.6	0.01
N_{DC}	399.2	398.2	−0.16
N_{DT1}	398.0	397.1	−0.28
N_{DT2}	397.8	397.0	−0.24

[a] N_{RM}: ring N bonded to methyl group; N_{RA}: ring N bonded to amino group; N_R: ring N, unsubstituted; N_A: amino N; N_{DC}: central $[DCA]^-$ N; N_{DT}: terminal $[DCA]^-$ N; N_{RB}: ring N bonded to butyl group. [b] Atomic charges were obtained using the Lowdin Population Analysis,[88] which is a Mulliken population analysis[89−91] based on symmetrically orthogonalized orbitals.

dx.doi.org/10.1021/jp3100409 | J. Phys. Chem. C 2013, 117, 5693−5707

unsubstituted ring nitrogen (N_R) and amino group nitrogen (N_A) contribute to the lower binding energy peak (~400 eV). For $[BMIM]^+$, the two ring nitrogen atoms (methyl and butyl substituted, N_{RB} and N_{RM}) give overlapping contributions to a peak around 401.5 eV. For $[DCA]^-$, theory agrees with the assignment discussed previously, namely, that the central N atom (N_{DC}) has higher binding energy and the two terminal N atoms (N_{DT}) have lower binding energies. This assignment is consistent with the calculated atomic charges listed in Table 1, which predict the two terminal nitrogens to be more negatively charged ($-0.19e^-$) than the central nitrogen ($-0.13e^-$).

Note that for the ILs the calculated N 1s binding energies for the $[DCA]^-$ anion appear to be ~1 eV lower; however, this is misleading. In fact, what we can say is that the splitting between N 1s peaks associated with the cation versus the anion is about 1 eV larger. The fact that the discrepancy appears to affect only the anion is an artifact of using the highest binding peak (on the cation) to correct the theoretical values. This discrepancy suggests that the average chemical environment surrounding the various N atoms is different in a room-temperature IL compared to an isolated ion pair, reflecting both thermal deviations from the minimum energy structure and the presence of many additional ions in the surroundings. The observation that the splitting is smaller in the IL than in the ion pair suggests that, as expected, interactions with neighboring ions tend to reduce the cation−anion charge difference compared to an isolated ion pair.

C 1s high-resolution spectra (Figure 2) were also analyzed for the same set of samples; however, their interpretation is more challenging. The difficulty results partly from the presence of carbonaceous adsorbates which deposit on any sample exposed to laboratory atmosphere and partly because there is less structure in the C 1s spectra. A common practice used to identify and reduce the contribution of adventitious carbon in XPS is to take spectra before and after using high-energy Ar^+ ions to sputter away the surface layer of the sample. This process also damages molecules in the near-surface region probed by XPS, thus the results have to be interpreted with caution. Lovelock et al.[61] have shown that clean surfaces can be obtained by sputtering for the $[C_nC_1Im][Tf_2N]$ IL systems. Data showing sputtering effects on the ILs and other materials of interest for the two IL systems studied here are presented in the SI. Unfortunately, some of the materials, particularly Na[DCA] and [BMIM]Cl, are rapidly and extensively damaged by Ar^+ sputtering, and for this reason most of the discussion focuses on the spectra of unsputtered samples. We note, however, that for the N 1s spectra, which provide the most insight into the IL structure and binding to the boron surfaces, the spectra of the ILs, themselves, are essentially unaffected by sputtering; i.e., the adventitious adsorbates have negligible effects. The major contribution from adventitious adsorbates is significant on the C 1s spectra, and for these spectra we used sputtering to identify the peaks arising from adventitious sources but did not attempt to completely remove the contaminants.

The data on sputtered surfaces show that adventitious carbon made its major contribution to a single peak in each spectrum, and as is common, we have used this adventitious carbon peak as a binding energy reference, shifting each spectrum to put adventitious C 1s at 284.5 eV.[48] This reference method works well in this system, giving binding energies for B^0 and B^{3+} that are in excellent agreement with literature values, as shown below.

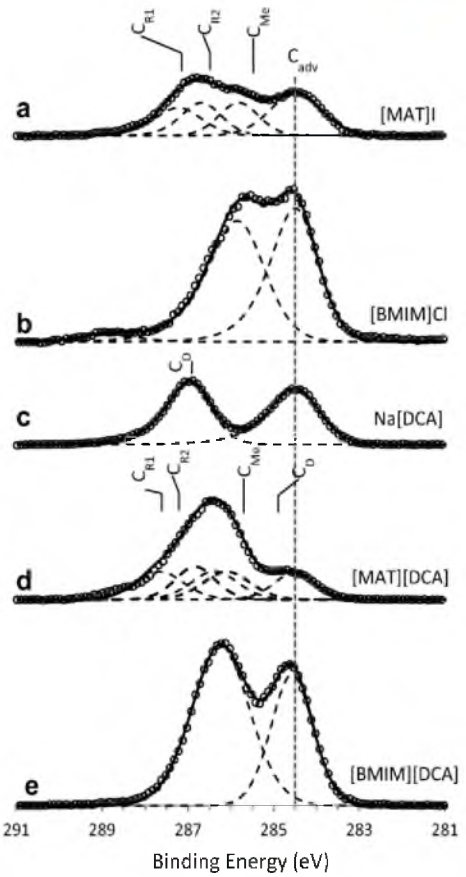

Figure 2. C 1s high-resolution XPS scan of (a) [MAT]I, (b) [BMIM]Cl, (c) Na[DCA], (d) [MAT][DCA], and (e) [BMIM][DCA].

The C 1s spectra in Figure 2 are for unsputtered [MAT]I, [BMIM]Cl, Na[DCA], [MAT][DCA], and [BMIM][DCA], with the adventitious C 1s peak indicated by a vertical dashed line. The C 1s binding energies from DFT calculations are shown as vertical lines above each spectrum, and the theoretical and experimental binding energies are summarized in Table 2. For the $[MAT]^+$-containing samples, assignments can be made by comparing DFT and experiment. The three carbon atoms in [MAT]I have calculated binding energy values ranging from 285.5 to 287.2 eV, with the ring carbons having higher energies than the methyl carbon. These three peaks overlap to form a single asymmetric feature, which can be seen more clearly when the adventitious signal is reduced by sputtering (SI Figure S6). The two carbon atoms of the Na[DCA] are identical, with a C 1s binding energy of 286.9 eV—surprisingly high considering that this is an anion. The DFT results are in good agreement with this observation, however, and explain the high binding energy by showing that the negative charge is delocalized on the three N atoms, with the C atoms having negligible charge.

Since the observed C 1s binding energies of [MAT]I and Na[DCA] are in the same range, it is not surprising that the spectrum for [MAT][DCA] consists of a single peak. The experiment suggests that the C 1s binding energy for the $[DCA]^-$ carbon atoms in the IL are shifted lower than in Na[DCA], and again this suggestion is consistent with the DFT

dx.doi.org/10.1021/jp3100409 | J. Phys. Chem. C 2013, 117, 5693−5707

Table 2. C 1s Binding Energy Values and Atomic Charges Obtained from XPS and DFT Calculations[a]

nitrogen atom	experimental binding energy (eV)	calculated core energy (eV)	atomic charge[b]
[MAT]I			
C_{R1}	287.2	287.2	−0.11
C_{R2}	286.7	286.5	−0.04
C_{Me}	285.8	285.5	−0.13
Na[DCA]			
C_{D1}	286.9	286.7	−0.03
C_{D2}	286.9	286.7	−0.03
[MAT][DCA]			
C_{R1}	287.6	287.6	0
C_{R2}	286.8	287.2	−0.01
C_{Me}	286.4	285.7	−0.10
C_{D1}	286.3	284.9	−0.07
C_{D2}	286.2	284.8	−0.05
[BMIM]Cl			
C_{R1}	Peak 1	287.2	−0.08
C_{R2}		286.0	−0.09
C_{R3}		286.0	−0.09
C_{Me}		286.0	−0.13
C_{B1}		286.0	−0.10
C_{B2}	Peak 2	285.0	−0.18
C_{B3}		284.8	−0.17
C_{B4}		284.5	−0.23
[BMIM][DCA]			
C_{R1}	Peak 1	287.1	−0.03
C_{R2}		286.2	−0.05
C_{R3}		286.2	−0.07
C_{Me}		285.8	−0.11
C_{B1}		286.4	−0.08
C_{B2}	Peak 2	284.8	−0.17
C_{B3}		284.0	−0.18
C_{B4}		283.7	−0.23
C_{D1}		284.8	−0.09
C_{D2}		284.6	−0.09

[a] C_{R1-R3}: unsubstituted ring carbons; C_{Me}: methyl carbon; $C_{D1,D2}$: dicyanamide carbons; C_{B1-B4}: butyl carbons. [b] Atomic charges were obtained using the Lowdin Population Analysis,[89] which is a Mulliken population analysis[89−91] based on symmetrically orthogonalized orbitals.

results, although as discussed above, DFT gives the cation−anion splittings that are larger than in the experiment.

The experimental [BMIM]Cl and [BMIM][DCA] C 1s spectra show two relatively sharp peaks, one of which clearly is at least partly due to adventitious carbon. This adventitious carbon peak does not sputter away in [BMIM][DCA] to the same extent as in the other samples (SI Figure S4). This suggests that this peak may have contributions from the $[BMIM]^+$ cation[57] based on the fact that this peak is also present in [BMIM]Cl. Figure 2e does not show individual experimental fit components because there is simply no unambiguous way to fit two peaks with more than eight distinguishable C 1s binding energies (eight from $[BMIM]^+$, plus a pair from $[DCA]^-$). The figure also does not indicate the DFT-estimated C 1s binding energies, simply for lack of space. The DFT results are given in Table 2 and are in good agreement with the observation that there are two groups of binding energies, one around 284.5 eV and one around 286 eV.

The sputtering results shown in the SI (Figures S1−S11) are peripheral to the main point of this study but are interesting enough to warrant a brief description. For [MAT]I, [MAT][DCA], and [BMIM][DCA], sputtering resulted in relatively minor changes in the C 1s and N 1s spectra, apart from the decrease in the C 1s peaks thus identified as arising from adventitious carbon. In particular, the peak positions shifted very little, and there are no major intensity changes. The changes are consistent with the sample remaining largely unchanged, with a small admixture of damaged molecules in the top few nanometers of the samples, probed by XPS.

In contrast, sputtering causes dramatic changes in the [BMIM]Cl and Na[DCA] samples, as shown by the C 1s and N 1s spectra (SI Figures S7−S11). For [BMIM]Cl, the N 1s signal dramatically broadened, and the integrated intensity decreased significantly, indicating preferential loss of nitrogen from sputtering. The C 1s signal shifted to higher binding energy with sputtering; the intensity in the range attributed to adventitious and aliphatic carbon signals was also reduced dramatically; and the total C 1s signal increased substantially, indicating an increase in the fraction of carbon in the near-surface region. Finally, there was a larger-than-normal increase in the background pressure during sputtering, suggesting substantial evolution of a gaseous product. The fact that the changes are so dramatic, affecting essentially all molecules in the near-surface region, suggests that sputtering triggers decomposition. There may also be some conversion of the Cl^- to an alkyl chloride, as suggested by the observation that the Cl 2p peak (SI Figure S9) also shifted to a higher binding energy after sputtering, which is characteristic of such compounds.[62]

For Na[DCA], the N 1s spectrum also changes dramatically with a substantial decrease in N intensity, a shift of the main spectral features to lower binding energy, and growth of a small feature at ~404 eV, which is well above the range typically seen in oxygen-free organo-nitrogen compounds.[63] In contrast to the [BMIM]Cl results, where the C 1s spectrum shifts to higher binding energy, the Na[DCA] C 1s signal shifts to substantially lower binding energy with essentially no signal remaining at the unsputtered peak position. Again, these results suggest that sputtering initiates some decomposition chain reaction that destroys all the molecules in the near-surface region. While these observations have no effect on interpretation of the XPS results, they are interesting examples of severe sputter damage and can be compared to the thermal decomposition results discussed below.

B. Summary of Particle Properties. We previously[46] showed that boron milled with [MAT][DCA] generated particles mostly in the 50−70 nm size range, with a tail running out to ~150 nm. The particles were coated with a solvent-resistant IL layer that prevented oxidation upon exposure to air. The question of how an IL like [MAT][DCA] could bind strongly to boron surfaces prompted the present investigation into the binding mechanism. Given that boron is generally considered to be electron deficient,[64] one potential binding motif is complexation of the $[MAT]^+$ cation to boron via interaction of the lone pair on the amino group; however, one might also expect that the anion might bind via lone pairs on either the central N atom or the nitrile groups. For comparison purposes, therefore, we also produced boron nanoparticles by milling with the IL [BMIM][DCA], which has the same anion but a cation without an amino substituent. Boron milled with [BMIM][DCA] produced a black viscous

dx.doi.org/10.1021/jp3100409 | J. Phys. Chem. C 2013, 117, 5693−5707

suspension, which showed some sign of settling after 48 h, similar to that formed by milling with [MAT][DCA]. DLS measurements of the [BMIM][DCA]-coated nanoparticles dispersed in ethanol (Figure 3) showed a relatively sharp

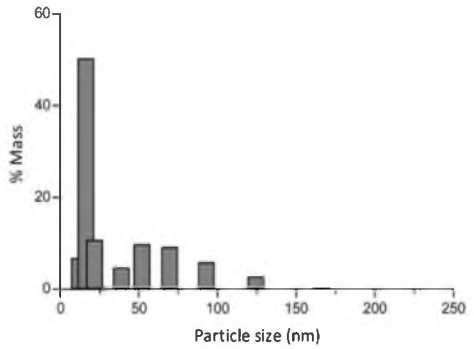

Figure 3. Mass weighted DLS size distribution of boron [BMIM][DCA].

feature around 20 nm in the mass-weighted size distribution, with a broad tail extending to ~125 nm, which may result from aggregates of smaller primary particles. This represents a significant shift to smaller particles, compared to those produced with [MAT][DCA] under identical conditions, possibly because [BMIM][DCA] is less viscous.[15,65] SEM imaging of samples washed with ethanol as described above showed individual irregularly shaped boron particles 50−70 nm in diameter; however, TEM (Figure 4) suggests that these large particles seen in SEM are aggregates formed in drying of primary particles that appear to be ≤20 nm. Electron energy loss spectroscopy (EELS) analysis confirmed that the particles observed are indeed composed of boron with traces of nitrogen, carbon, and oxygen, which presumably reflect some contribution from the IL and from adventitious adsorbates.

Trace amounts of tungsten and cobalt contaminants originating from the milling media and jar were observed in XPS (SI Figure S14). We previously demonstrated that this contamination is in the form of small particles and that the contamination level can be reduced substantially by simply stirring the milling products with a magnetic stir bar, which collects the cobalt-cemented tungsten carbide particles quite efficiently.[45]

We also produced particles by milling boron with the salts [MAT]I, [BMIM]Cl, and Na[DCA], which contain only one of the cations or anions that make up the two ILs of interest. Because our interest in the salt-milled particles was in their surface chemistry, we did not characterize size distributions or other particle properties.

C. Boron Nanoparticle Passivation by ILs. The oxidation state of boron nanoparticles milled under different conditions was studied using XPS, taking advantage of the low IL vapor pressures[36,66] to study both washed and IL-wetted particles. For unoxidized elemental boron (B^0), the B 1s binding energy is 188 eV, and when fully oxidized to B_2O_3 (B^{3+}), the B 1s binding energy is shifted by 5 to 193 eV.[48] As shown in Figure 5a, when boron nanoparticles are produced, as described above, but with no passivating agent (only acetonitrile to prevent caking of the dry powder), then air-dried prior to transfer to the XPS instrument, peaks are observed for both elemental boron in the core of the particles and B^{3+} in the oxide layer that

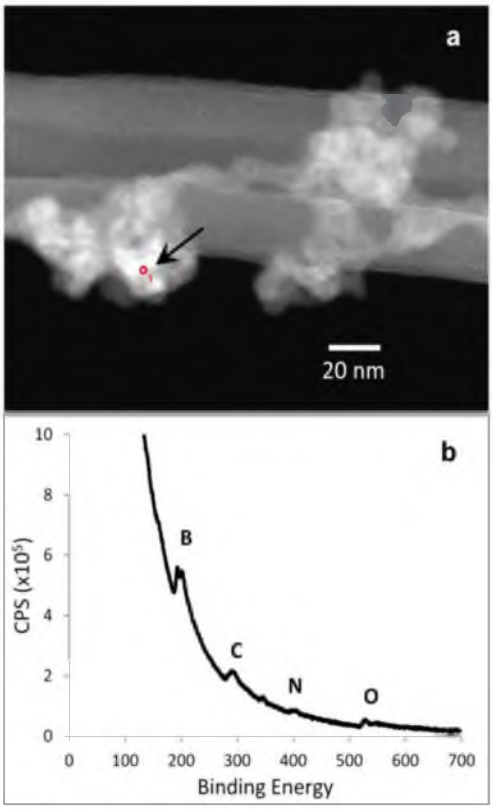

Figure 4. (a) High-resolution TEM image of boron nanoparticles. (b) EELS spectrum of the area marked with a circle on image (a).

spontaneously formed upon air exposure. As discussed previously, the intensity of the B^{3+} peak for milled, unpassivated boron is actually substantially larger than it is for unmilled, oxidized boron.[45] This effect is attributed to the deposition of dissolved boron oxide or small, completely oxidized boron particles, on the surface of the sample when it is dried for analysis.

When boron is produced in either [MAT][DCA] or [BMIM][DCA], and the IL-wetted nanoparticles are analyzed without washing (Figures 5b and e), no signal is observed for either elemental boron or fully oxidized boron. Instead, there is a weak signal (note scale factors in the figure) for boron with B 1s binding energy of ~191.5 eV, corresponding to some intermediate oxidation state (B^{n+}). If the particles are thoroughly washed with ethanol, as described above, to remove excess IL (Figures 5c and f), then XPS shows a substantial peak for B^0, with a weak tail that extends into the region corresponding to B^{n+} and little if any signal for fully oxidized B^{3+} at 193 eV. Finally, if the ethanol used in the washing process is evaporated to recover the excess IL washed off of the particles, XPS of this residue shows a small amount of boron, predominantly corresponding to the intermediate oxidation state, B^{n+} (Figure 5d and g). Note that an alternative explanation for the 191.5 eV feature in the B 1s spectra of milled samples might be the formation of some boron particles that are so small that charging and screening of the photoemission core hole state is inefficient compared to bulk boron, resulting in higher measured B 1s binding energy. The

dx.doi.org/10.1021/jp3100409 | J. Phys. Chem. C 2013, 117, 5693−5707

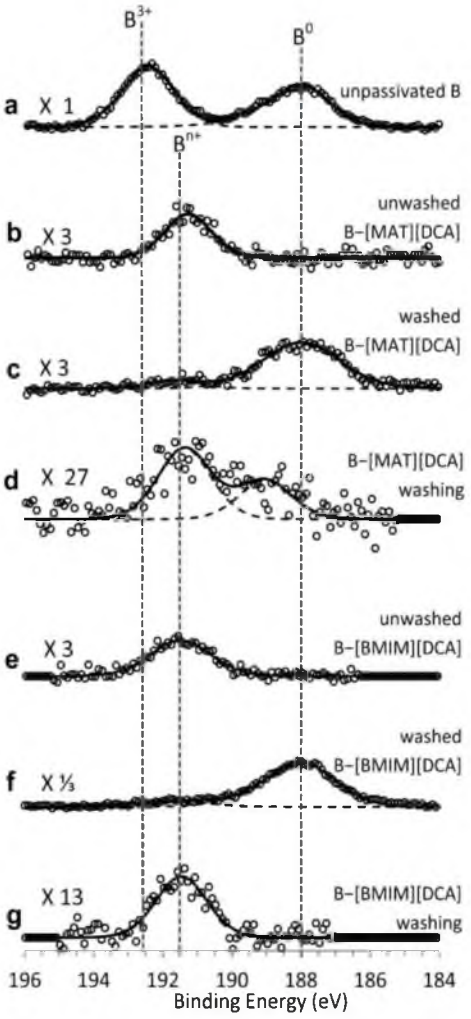

Figure 5. B 1s high-resolution XPS scan of (a) boron milled with acetonitrile with no added IL, (b) boron milled with [MAT][DCA] unwashed, (c) boron milled with [MAT][DCA] completely washed with ethanol, (d) [MAT][DCA] recovered from a milled boron sample after washing with ethanol, (e) boron milled with [BMIM]-[DCA] unwashed, (f) boron milled with [BMIM][DCA] completely washed with ethanol, and (g) [BMIM][DCA] recovered from the milled boron sample after washing with ethanol.

fact that this 191.5 eV peak is diminished in the washed samples might simply indicate that such small particles tend to be lost in the washing/centrifuging process used to remove the excess IL from the particles.

Comparison of the XPS for washed particles (Figures 5c and f) with that for unpassivated boron (Figure 5a) shows that the washed particles must still be coated with a dense enough layer of IL to passivate the boron so that it does not oxidize during air exposure (for >8 h). This IL layer is bound strongly enough to resist removal by repeated ultrasonication in ethanol, which is a good solvent for the ILs. Acetonitrile is a better solvent for these ILs; however, we avoided the use of any N-containing solvents to eliminate N Is contributions from the solvent in the XPS. As shown in the survey spectra in SI Figure S14, the presence of substantial N 1s XPS signals is consistent with the presence of a capping layer derived from the ILs.

Comparison of the B 1s intensities of the B^0 peak in the washed samples (Figure 5c and f—note scale factors) shows that the B 1s signal from boron coated with [MAT][DCA] is ~10 times smaller than the signal observed from particles coated with [BMIM][DCA]. Given that the particles in each case are solid boron, the variations in intensity indicate that the solvent-resistant capping layer is substantially thicker (resulting in more attenuation of electrons from the underlying boron) for boron milled with [MAT][DCA] than for boron milled with [BMIM][DCA]. This conclusion is supported by the observation that the N 1s intensity is ~3 times greater for boron capped with [MAT][DCA] than for boron capped with [BMIM][DCA] (SI Figure S14), whereas the ratio of the number of N atoms is only 7:5 in the two ILs. As discussed in the SI, the intensities in Figure 5 can be used to estimate that the [MAT][DCA] capping layer is ~2 nm thicker than that for [BMIM][DCA]. TGA and IR results below provide additional insight into this issue, and the estimates of the layer thicknesses are given below.

The fact that neither B^0 nor B^{3+} signal is observed for the unwashed samples simply means that the boron particles are buried under a thick enough layer of IL that blocks detection of electrons emitted from the particles. As mentioned above, the effective attenuation length for B 1s photoelectrons in a material with the composition and density of these ILs is calculated to be ~3.3 nm,[67] thus the particles are invisible to XPS unless they are within ~10 nm of the liquid surface. Instead, the XPS signal is observed from some intermediate oxidation state boron (B^{n+}) that is dissolved or suspended in the IL, such that it has significant concentration in the top 10 nm of the IL. The presence of this B^{n+} boron in the ILs recovered from washing confirms this conclusion. The B^{n+} binding energy of ~191.5 eV observed for this dissolved/suspended boron could correspond to a suboxide; however, we note that the B 1s binding energy for boron nitride is reported to be in this range,[68] and while we do not suggest that boron nitride is formed in the milling process, it may be that this feature represents boron atoms or small boron clusters bound to the N-rich ILs, or some B_xN_y compound formed under our milling conditions, which is soluble in the ILs. We note that the ILs recovered from the washings are slightly darker in color than the IL starting materials.

One interesting question is whether the local high temperatures and mechanical forces generated during milling are required for formation of an effective passivating IL layer or if it is sufficient to simply allow clean boron surfaces to interact with neat ILs, after completion of the milling process. This question was tested for both [MAT][DCA] and [BMIM][DCA] by milling boron with only acetonitrile as a dispersing agent and then ultrasonicating the resulting boron particles with one or the other IL. These "post-milling IL-capping" experiments are described in more detail, and the data are presented in the SI (Figures S12 and S13). In brief, it was shown that a capping layer is formed by ultrasonicating boron with either of the ILs, that this capping layer persists after ethanol washing, and that it largely protects the boron from oxidation during subsequent air exposure. Comparison of Figures 5 and S12 (SI) shows, however, that protection against oxidation is significantly better for the particles milled with the ILs, compared to the particles that were ultrasonicated with the ILs after milling. It is possible that the milling really does drive more complete reaction of

dx.doi.org/10.1021/jp3100409 | J. Phys. Chem. C 2013, 117, 5693−5707

boron with the ILs, resulting in a better capping layer; however, we note that in the "post-milling IL-capping" experiments the particles have substantial exposure to the glovebox atmosphere during the postmilling workup, while the particles milled with ILs are capped immediately as they form. They, therefore, would be much less affected by possible oxidation by contaminants in the glovebox atmosphere.

D. Boron Nanoparticle–IL Interaction. Imidazolium-based ILs have been previously used as stabilizing agents in the synthesis of metal nanoparticles,[59,69−74] but not for highly reactive materials like boron. Calculations[70,75] and empirical[69] data suggest a number of possible motifs for interaction of these ILs with nanoparticles. Surface-enhanced Raman spectroscopy (SERS) studies done by Dupont's group on imidazolium IL-stabilized gold nanoparticles suggest a strong interaction between the imidazolium cation and the gold nanoparticle surface through a parallel coordination, where the imidazolium ring lies flat on the gold surface while a long chain ether functional group is directed away from the surface, providing steric stabilization.[74] Zhang et al. arrived at a similar conclusion using XPS to study imidazolium-functionalized gold and platinum nanoparticles. In addition, they found that reactive substituents (i.e., R−COOH, R−NH_2) on the imidazolium ring provided an alternative interaction with the nanoparticles.[59] Other evidence regarding imidazolium−metal interactions was obtained from ^{2}H NMR studies of functionalized iridium nanoparticles, which suggested formation of an N-heterocyclic carbene.[73] In addition to these studies suggesting that IL−metal interactions are dominated by the cation, there is work documenting the role of the anion. Anions with strongly coordinating atoms like F and O (i.e., BF_4^-, PF_6^-, and $CF_3SO_3^-$) were found to interact strongly with iridium nanoparticles, forming nonstoichiometric cationic and anionic supramolecular aggregates on the surface.[72] Khare also concluded that stabilization of Fe_3C nanoparticles with dicyanamide- and thiocyanate-containing ILs was due to the complex formed by either anion with iron.[71] For a material like boron, which is considered to be electron deficient, hence highly reactive, readily forming stable hydrides, carbides, oxides, and nitrides, it is not at all clear what interactions might be expected for ILs like [BMIM][DCA] or [MAT][DCA].

We probed the IL−boron interactions using a combination of XPS, FTIR, TGA, and zeta potential measurements. N and C 1s XPS analyses were performed on the same ethanol-washed boron nanoparticle samples used for the B 1s spectra in Figure 5c and f. Figure 6 compares the N 1s spectra of the IL-covered boron nanoparticles with the spectra of the corresponding pure ILs. In both cases, the highly structured N 1s spectra seen for the pure ILs collapsed into broad and almost featureless peaks for nitrogen in the IL capping layer. In particular, the higher binding energy peaks associated with the $[MAT]^+$ or $[BMIM]^+$ cations are substantially weakened in the IL−boron spectra, with the corresponding intensity shifted to lower binding energy. The residual intensity at high binding energies may, in fact, simply result from a small amount of free IL that was not washed from the sample by our three-step sonication−centrifugation process. In [MAT][DCA]−boron, the peaks associated with free $[DCA]^-$ shifted to higher binding energy, so that all the N 1s signal collapses into a single, relatively compact feature at intermediate binding energies. Core level binding energies shift depending on the charge on the atoms emitting the electrons, as exemplified by the splitting between N 1s peaks from the cations and anions of the free ILs. The fact

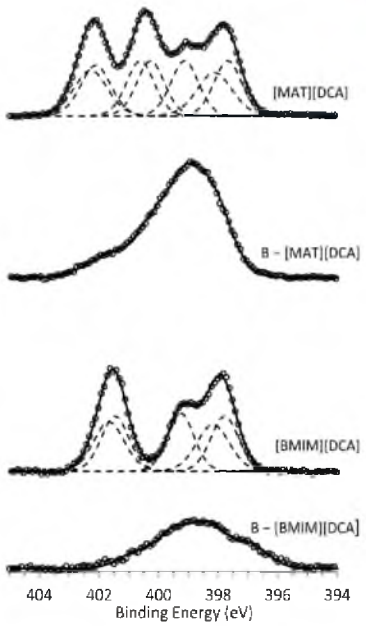

Figure 6. N 1s high-resolution scan of [MAT][DCA], boron milled with [MAT][DCA], [BMIM][DCA], and boron milled with [BMIM][DCA].

that the N atoms in the [MAT][DCA]−boron sample all have similar 1s binding energies suggests that the charge distribution in the capping layer is no longer strongly polarized. For [BMIM][DCA]−boron, a similar merging of cation- and anion-derived peaks into a single feature occurs, although the resulting feature is broader. The lower intensity observed for [BMIM]-[DCA]−boron is additional evidence that the capping layer is thinner for [BMIM][DCA]−boron than for [MAT][DCA]−boron.

C 1s spectra of the IL-coated boron samples are given in the SI (Figure S15). Because there was less structure in the carbon spectra of the pure ILs, it is harder to infer anything about binding from the boron−IL spectra. For [MAT][DCA]−boron, where the pure IL spectrum only has a single broad peak, the spectrum shows a slight shift and broadening toward higher binding energies. For [BMIM][DCA]−boron, where the pure IL showed two peaks, the spectrum collapses to a single, broad, almost structureless feature.

To help understand the IL−boron interaction, we also measured XPS of samples prepared by milling boron with [MAT]I, [BMIM]Cl, and Na[DCA]. Since these reagents are solids at room temperature, ethanol was added to the milling mix to avoid caking and achieve efficient mixing during milling. All three salts are quite soluble in ethanol, which was used to avoid introducing any other source of nitrogen. Prior to XPS analysis, samples were washed thoroughly with ethanol, as described above, to remove any material that was not bound tightly to the boron particles. Figure 7 shows the N 1s spectra of boron milled with [MAT]I, [BMIM]Cl, and Na[DCA]. Note that the sample prepared with [MAT]I and then washed still has significant N 1s intensity, indicating that [MAT]I is bound to the surface strongly enough to resist removal by repeated ultrasonic washing. In addition to the two peaks at 400 and 402 eV, characteristic of $[MAT]^+$ in pure [MAT]I and

dx.doi.org/10.1021/jp3100409 | J. Phys. Chem. C 2013, 117, 5693−5707

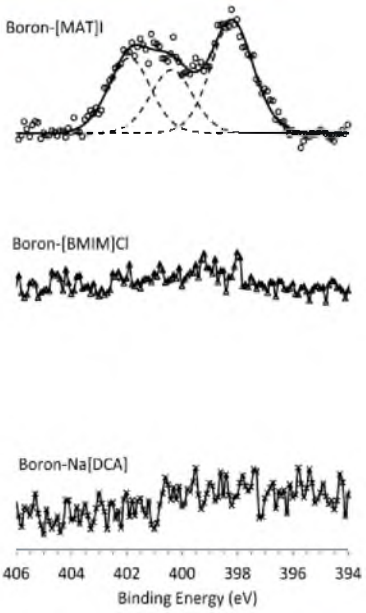

Figure 7. N 1s high-resolution XPS scan of boron samples milled with [MAT]I, [BMIM]Cl, and Na[DCA].

[MAT][DCA] (Figure 1), there is a new peak at ~398 eV, which is the N 1s binding energy for nitrogen in boron nitride[76] and which we attribute to formation of B−N bonds between $[MAT]^+$ and boron. The presence of all three peaks tends to suggest that the capping layer for boron−[MAT]I contains roughly equal amounts of $[MAT]^+$ that still looks like the free cation and $[MAT]^+$ that has reacted with the boron surface. In contrast, boron milled with [BMIM]Cl or Na[DCA] and washed shows essentially no XPS signal in the N 1s region, indicating that [BMIM]Cl and Na[DCA] were completely washed out of the sample.

It is tempting to interpret these results as showing that the $[MAT]^+$ cation binds to boron surfaces, while both $[DCA]^-$ and $[BMIM]^+$ do not; however, several observations indicate that the situation is more complex and that binding depends on both the cation and anion and interactions between the two. For example, while $[BMIM]^+$ and $[DCA]^-$ do not bind strongly to boron when paired with Cl^- and Na^+, respectively, the [BMIM][DCA] combination does form a dense, solvent-resistant capping layer. It is also interesting that while the N 1s spectrum of boron−[MAT]I shows signs of both free $[MAT]^+$ and nitrogen making strong B−N bonds, there is essentially no signature for free $[MAT]^+$ in the capping layer formed for boron−[MAT][DCA], despite the indications from B 1s XPS and TGA (see below) that the capping layer for boron−[MAT][DCA] is relatively thick. The fact that the anion is $[DCA]^-$ in one case and I^- in the other may affect both boron−$[MAT]^+$ binding, hydrogen bonding within the capping layer, and the extent to which charge is redistributed between cation and anion. For example, I^- and $[DCA]^-$ are quite different in size and shape, and the electron affinity of the $[DCA]^-$ radical has been measured to be 4.14 eV[77] compared to 3.06 eV[78] for iodine atoms. It could be that I^- tends to bind to the boron surface to some extent, helping to stabilize the [MAT]I capping layer, and that [BMIM]Cl and Na[DCA] do not form a solvent-resistant layer partly because the Cl^- and Na^+ counterions do not interact with boron strongly enough.

In the case of the $[BMIM]^+$ cation, although it has been found that metal nanoparticles may interact with the imidazolium ring lying flat on the surface,[74] this interaction may not be strong enough to prevent it from being removed from the boron surface through rigorous ultrasonic washing by ethanol. Data from zeta potential experiments presented later confirmed this conclusion.

Infrared spectroscopy provides additional insight into the binding of the ILs to boron surfaces. Figure 8 compares spectra

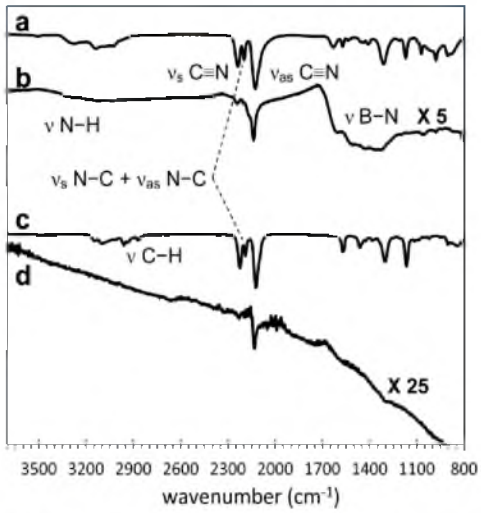

Figure 8. FTIR spectra of (a) neat [MAT][DCA], (b) boron milled with [MAT][DCA] washed with ethanol, (c) neat [BMIM][DCA], and (d) boron milled with [BMIM][DCA].

of neat [MAT][DCA] and [BMIM][DCA] with those for ethanol-washed samples of boron capped with each IL. One obvious point is that the signatures of IL binding in the [BMIM][DCA] case are substantially weaker than those for [MAT][DCA] (note scale factors), providing additional evidence that the capping layer is thicker in the latter case. The strongest spectral feature for both ILs is a group of three intense peaks at 2246, 2193, and 2126 cm^{-1} which have been assigned as vibrations of $[DCA]^-$.[79] These are, respectively, the symmetric C≡N stretch (ν_s), overlapping symmetric and asymmetric stretches of the N−C bonds about the central N (ν_{as} N−C + ν_s N−C), and the asymmetric C≡N stretch (ν_{as}). In addition, N−H and C−H stretches from the amino and methyl groups, respectively, were also observed in the 3300−3000 cm^{-1} region[79] for [MAT][DCA], while the C−H stretching modes from the methyl and butyl substituents were observed from 2980 to 2900 cm^{-1} for [BMIM][DCA].

For the ILs on boron, all the IL-specific peaks decrease substantially in intensity (note scale factors), presumably because the IL capping layers are thin compared to the IL layer studied for the neat ILs. The N−H stretch in [MAT][DCA] appears to be broadened and shifted to higher wavenumbers for boron−[MAT][DCA], and the various C−H stretches for both ILs are nearly absent in the boron−IL samples. The effect on the N−H stretch would be consistent with binding of $[MAT]^+$ to the surface via interaction of the amino group. Also, B−N bond formation is consistent with the

dx.doi.org/10.1021/jp3100409 | J. Phys. Chem. C 2013, 117, 5693−5707

appearance of a broad peak at about 1350 cm^{-1} that has been attributed to a B−N stretching mode.[80,81] The absence of such a feature for [BMIM][DCA], which has no amino group, would be consistent with this scenario.

Note, however, that the spectral features associated with $[DCA]^-$ are also strongly perturbed by binding to the surface, suggesting that the anion is also involved in the binding. In particular, the symmetric C≡N stretch and C−N stretching bands are attenuated substantially compared to the asymmetric C≡N stretching bands in both [MAT][DCA] and [BMIM]-[DCA] samples. These changes in features associated with $[DCA]^-$ suggest that there must also be boron−[DCA] interactions, as have been seen for titanium nanoparticles.[82] If, for example, one of the terminal N atoms in $[DCA]^-$ reacted with boron, this would break symmetry, eliminating both symmetric stretch modes and leaving a single C≡N stretch of the nonbonded end of the DCA. Both the XPS and IR results, therefore, tend to suggest that there is strong boron−$[MAT]^+$ bonding, likely involving the amino group. However, there appears to be interaction of $[BMIM]^+$ and $[DCA]^-$ with the boron as well and that some degree of cooperativity between cation and anion binding to boron probably affects all these systems.

Another way of examining how ILs and salts bind to nanoparticle surfaces is by measuring the zeta potential of the samples. In essence, this technique applies an AC electric field across a sample of nanoparticles suspended in a solvent and measures the amplitude and direction of the resulting AC motion. The zeta potential is related to the electric potential at the boundary between the layer of ions that is attached to the particle surface tightly enough to move with it (the Stern layer), as opposed to the diffuse layer of counterions dissolved in the solvent.[83] Zeta potential is sensitive to the net charge of the ionic species binding on the particle surface. Figure 9 gives the zeta potentials measured for boron nanoparticles produced under a variety of conditions, using acetonitrile as an aprotic solvent. Using acetonitrile as an inert solvent eliminates the effect of pH changes, thus the measured zeta potentials are comparable to results obtained under neutral conditions. This was confirmed by measuring the zeta potentials of SiO_2 and Al_2O_3 powder dispersed in acetonitrile, where both oxides displayed similar values to what is found for dispersions in water at pH 7.[84]

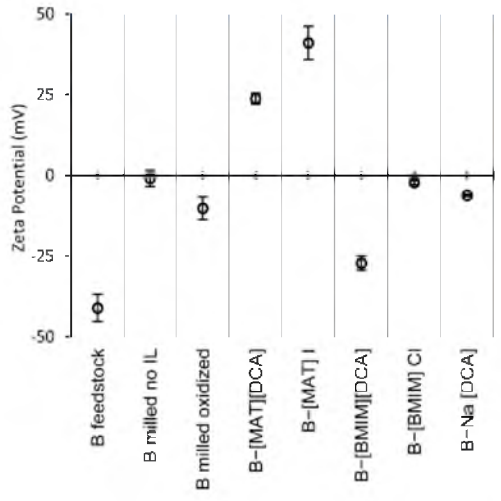

Figure 9. Zeta potential measurements of boron nanoparticles coated with ILs and other test ligands.

The unmilled boron feedstock has a zeta potential of about −42 mV, implying net anionic charging. The negative zeta potential presumably reflects the fact that the boron feedstock is covered by an oxide layer and probably has a significant coverage of adsorbed atmospheric water. When dispersed in a polar solvent, adsorbed water may hydrolyze leaving OH^- species on the surface of the particle.

Boron milled in acetonitrile with no capping ligands and measured without exposure to O_2 beyond what could diffuse through the acetonitrile solvent resulted in a zeta potential of essentially zero (−1.0 ± 2.5 mV), probably because the oxide was dispersed in the acetonitrile, leaving an essentially neutral surface as the particles are crushed during milling. When the same boron particles were air-dried to allow oxidation, then resuspended in acetonitrile, the zeta potential (−10.2 ± 3.5 mV) was found to be intermediate between those of the oxidized feedstock and the milled unoxidized boron, confirming that boron surface oxidation tends to give a negative zeta potential.

When boron was milled with [MAT][DCA] and [MAT]I, the particles have positive zeta potentials, indicating that the strongly bound layer is dominated by the $[MAT]^+$ cation. In contrast, boron particles functionalized with [BMIM][DCA] showed a negative zeta potential, suggesting that in that system the strongly bound layer is dominated by $[DCA]^-$. Interestingly, the zeta potentials of boron milled with either Na[DCA] or [BMIM]Cl are essentially zero, which could mean either that the strongly bound layer has equal numbers of cations and anions or simply that neither of these salts binds significantly. The XPS results (Figure 7), which show almost no nitrogen on the surface of ethanol-washed samples of boron milled with Na[DCA] or [BMIM]Cl, demonstrate that these salts simply do not bind.

The zeta potential measurements reinforce the XPS finding that [MAT][DCA], [BMIM][DCA], and [MAT]I form solvent-resistant layers on boron surfaces and reveal whether these layers are dominated by anions or cations. Furthermore, the fact that the zeta potential for boron−[MAT]I is much more positive (+41 ± 5 mV) than that for boron−[MAT][DCA] (+24 ± 2 mV) suggests that in the latter case there is more anion binding, partially canceling the potential from the cations. The fact that the zeta potential for boron−[BMIM][DCA] is strongly negative indicates that the ionic surface layer is dominated by $[DCA]^-$ in this case, suggesting weak binding by $[BMIM]^+$, presumably because it lacks the amino group that seems to be involved in boron−$[MAT]^+$ binding. We propose that both cations and anions are interacting with boron in both cases; however, for [MAT]-[DCA] the stronger cation binding via the amino group gives a net positive charge, while for boron−[BMIM][DCA], the net negative charge indicates that the anion binding density is higher than that of the cation. Note that for [MAT][DCA] our results cannot distinguish clearly between dative B−N binding (B−$N(H_2)$−) and covalent BN binding, which would be accompanied by loss of one or more of the amino H atoms (either as H_2 or by formation of the B−H bond).

E. IL Desorption and Boron Nanoparticle Oxidation. As a final probe of IL−boron coordination, we used thermogravimetric analysis (TGA) to examine the thermal stability of the IL layer. One of the main motivations for coating

dx.doi.org/10.1021/jp3100409 | J. Phys. Chem. C 2013, 117, 5693−5707

boron particles with ILs is to prevent oxide layer formation in ambient air, but of course it is important that oxidation occurs efficiently at higher temperatures, to allow boron ignition. Therefore, we studied the thermal behavior of pure [MAT][DCA] and [BMIM][DCA] and of boron nanoparticles capped with each IL in oxygen. The percentage mass change is plotted against temperature in Figure 10a. For the pure ILs, mass losses

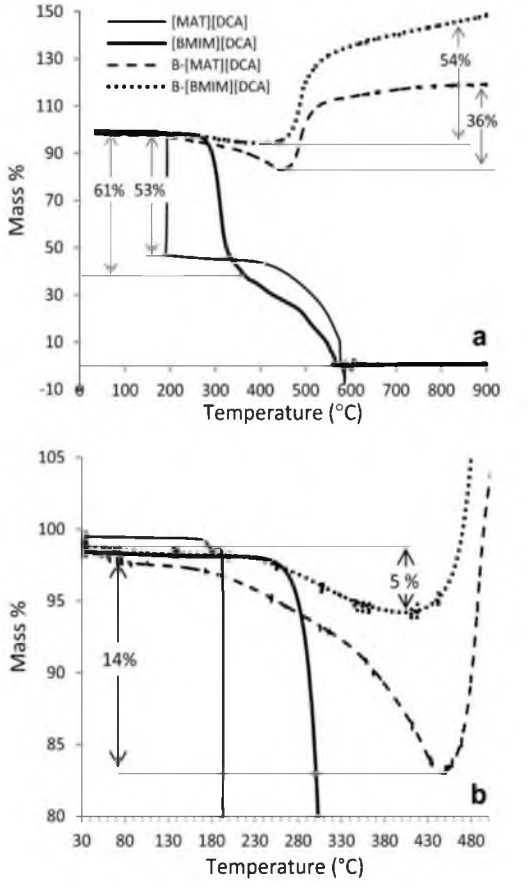

Figure 10. (a) TGA spectra of the neat ILs and boron samples milled with them. (b) Magnified portion showing mass decrease of boron-milled samples.

are expected, as the IL decomposes and/or is oxidized to gaseous products. For IL-capped boron, there should be mass loss associated with loss of the IL layer, but there is an offsetting mass gain associated with oxidizing the boron particle. Therefore, the net mass change for IL-capped boron will depend on the mass fraction of IL in the original samples.

For both ILs, two stage mass losses were observed, with the final mass near zero, indicating complete decomposition/combustion. For [MAT][DCA], the first stage is a sudden, isothermal mass loss of 53% at 192 °C, followed by a gradual decomposition/combustion leading to loss of the remaining mass over the temperature range from 370 to 580 °C. The residual mass at high temperatures is ~0.84% of the initial mass. The initial 53% mass loss at 192 °C is comparable to the stoichiometric mass percentage of the $[MAT]^+$ cation (59.8%). Furthermore, TGA of [MAT]I under similar conditions shows the onset of mass loss at about the same temperature, as shown in SI Figure S17. The similarity of these two measurements, together with the observation that the initial decomposition of [BMIM][DCA] occurs at much higher temperatures, indicates that this initial decomposition is triggered by the decomposition of the $[MAT]^+$. The material remaining after $[MAT]^+$ decomposition (probably a neutral derivative of $[DCA]^-$) may form polymeric products[85,86] before it is totally decomposed/oxidized in the temperature range between ~400 and 580 °C. It is interesting that for [MAT]I >90% of the total mass is lost in the initial decomposition event, suggesting that $[MAT]^+$ decomposition leaves behind mostly products that are volatile at these temperatures. For example, it may be that in the decomposition process charge transfer results in formation of I atoms that recombine and desorb as I_2.

The TGA of [BMIM][DCA] shows initial decomposition starting at higher temperature (~280 °C) and not quite as sharp as that for $[MAT]^+$ decomposition. The mass fraction lost initially is ~61%, which is reasonably consistent with the mechanism being decomposition of the $[BMIM]^+$ cation (67% mass) to gaseous products. Furthermore, TGA analysis of [BMIM]Cl under the same conditions (SI Figure S18) shows essentially 100% mass loss at slightly lower temperatures, again suggesting that for the IL cation decomposition leaves material that must be slowly oxidized away, while decomposition of the cation in the salt leaves a volatile product, such as Cl_2 or some organic chloride. Interestingly, for [BMIM][DCA], the second stage of decomposition begins to occur at a temperature lower than for [MAT][DCA], although the decomposition/oxidation goes to completion at about the same temperature.

As the IL makes up only a fraction of the initial mass in the IL-capped boron samples and because mass gain from boron oxidation offsets mass loss from IL decomposition, oxidation of these samples is more complex. Figure 10b shows the same TGA results magnified to allow the subtle changes to be seen more clearly. For [BMIM][DCA]-capped boron, there is ~5% mass loss in the range between 200 and 430 °C, by which point the pure [BMIM][DCA] IL would have lost >70% of its mass. (Note: The <1% mass losses seen below 200 °C probably just result from evaporation of residual ethanol that was used to wash excess IL from the particles, despite the fact that the washed particles were dried for more than 24 h at room temperature.) Starting around 430 °C, there is a rapid mass gain, and the 54% magnitude indicates that more than just a surface layer is oxidized; i.e., diffusion of oxygen and boron in the surface oxide layer that forms on the particles is fast enough to allow oxidation of the particle bulk. In this context, it is interesting to note that the melting point of bulk boron oxide is 450 °C,[87] thus significant bulk oxidation appears to require temperatures very close to the oxide melting point.

Several different limiting analyses of the mass loss/gain pattern are given in the SI, and the results are summarized here. One limiting analysis approach is to assume that all the IL leaves the surface as it is heated to ~430 °C but that the boron surface does not oxidize at all in this temperature range. This assumption is not realistic, but it gives a rigorous lower limit on the amount of IL that could initially have been present on the particles. We also analyzed a variation on this scenario, where boron did not oxidize and the IL on the surface was assumed to have a mass loss identical to that in the neat IL (i.e., only a fraction of the IL is lost below 430 °C). A more realistic assumption is that the boron surface oxidizes to form a self-limiting oxide layer as the IL leaves the surface when the sample

is heated to 430 °C. We further assume that the fraction of IL that decomposes up to this temperature is the same on the boron surface as in the neat IL. Given that bulk oxidation does not occur below 430 °C, this set of assumptions results in an upper limit on the amount of IL that could have been present initially.

Table 3 lists the lower (column 1) and upper (column 3) limits on the mass of IL/nm^2 and the corresponding number of ion pairs/nm^2 present on the ethanol-washed particles. The table also gives estimates of how these limits correspond to the number of monolayers of IL, depending on whether the ILs lie parallel or perpendicular to the surface of the particle. For the [BMIM][DCA] capping layer, the lower and upper limits on the number of ion pairs/nm^2 are 1.8 and 4.7, and we expect that the true value should be closer to the upper limit. This upper limit corresponds to only ~3 monolayers of IL bound to the surface, indicating that a quite thin IL layer is sufficient to block oxidation of the boron by air.

Table 3. IL Coverage on Boron Nanoparticle Calculated TGA Data[a]

	1st scenario (B does not oxidize until IL is fully decomposed)		2nd scenario (B simultaneously oxidizes while IL decomposes)
ionic liquid	case 1	case 2	case 2
[MAT][DCA]			
mass density (fg/nm^2)	3.8×10^{-6}	7.1×10^{-6}	7.8×10^{-6}
ion pair density (IL/nm^2)	13.9	25.9	28.4
number of monolayers			
parallel to surface	5.8	10.9	11.9
perpendicular to surface	1.6	3.1	3.38
[BMIM][DCA]			
mass density (fg/nm^2)	6.2×10^{-7}	9×10^{-7}	1.6×10^{-6}
ion pair density (IL/nm^2)	1.8	2.6	4.7
number of monolayers			
parallel to surface	1.3	1.8	3.2
perpendicular to surface	0.2	0.3	0.6

[a]Case 1: mass loss is due to 100% decomposition of IL at 450 °C. Case 2: mass loss is due to partial decomposition of IL at 450 °C.

For [MAT][DCA], significant mass loss starts below the temperature where pure [MAT][DCA] begins to decompose, which may simply indicate that [MAT][DCA]-capped boron tends to retain ethanol (resulting in larger solvent mass loss) or could imply that the boron surface actually initiates $[MAT]^+$ decomposition at lower temperature. The initial mass loss rate is much less abrupt than that for pure [MAT][DCA], increasing slowly with temperature until mass gain suddenly becomes apparent between ~430 and 450 °C (Figure 10b). The total mass loss to the minimum is 14%, and the mass gain relative to the minimum is only 36%.

Several points seem clear regarding the interpretation of the [MAT][DCA]-capped boron results. The larger mass loss indicates that the thickness of the solvent-resistant IL capping layer is substantially greater for [MAT][DCA] than for [BMIM][DCA], consistent with the conclusions drawn from the XPS and IR data. Using the same assumptions discussed, the results in Table 3 are obtained. Note that the IL mass/nm^2 and number of ion pairs/nm^2 are substantially greater for [MAT][DCA] than [BMIM][DCA], consistent with the conclusions from XPS and IR. However, it is probably not reasonable to simply compare upper or lower limits for the two IL systems. For [BMIM][DCA], the IL layer is quite thin, thus it seems likely that boron oxidation should start quite early as the IL layer is removed, but for the much thicker [MAT][DCA] layer, it may be that there is not much boron oxidation over most of the temperature range below 430 °C. Nonetheless, if we compare the lower limit estimate for [MAT][DCA] with the upper limit for [BMIM][DCA], it is clear that the [MAT][DCA] layer is at least ~3 times thicker than that for [BMIM][DCA], which is in reasonable agreement with the difference in the N 1s XPS signal for the two samples. Also, with the results obtained from B 1s XPS intensities that the [MAT][DCA] overlayer is ~2 nm thicker than [BMIM][DCA], we can approximate a thickness of 3 nm for [MAT][DCA] and 1 nm for [BMIM][DCA], which is a reasonable estimate for a monolayer of [BMIM][DCA] and 2–4 monolayers of [MAT][DCA] oriented perpendicular to the surface of the nanoparticles (Table 3).

It is interesting that such a thick layer remains for [MAT][DCA] after our aggressive ultrasonic washing process. The data presented in Figure 10 for the B–[MAT][DCA] sample were already washed for a total of five times (two more than our typical three-cycle washing), but still a significant amount of [MAT][DCA] was observed. Another sample, washed ultrasonically for three cycles, gave a mass loss of 32% (i.e., 17% more than the five-times-washed sample in Figure 10). The observation that thick [MAT][DCA] capping layers survive such aggressive washing suggests that there are stronger cohesive interactions within the [MAT][DCA] compared to [BMIM][DCA], which might be expected from the possibility of forming strong hydrogen bonds between the amino group on $[MAT]^+$ and the lone pairs in one or more nitrogen atoms of $[DCA]^-$.

IV. CONCLUSIONS

Nanoparticulate boron powder dispersed in, and capped with, two different hypergolic ILs was synthesized using a ball milling technique. We have shown that the boron nanoparticles produced through this process are capped by IL layers that are dense enough to protect the boron surfaces from air oxidation. The combination of XPS, IR, and zeta potential results suggest that binding by $[MAT]^+$ is dominant when it is present, probably involving a B–N bond. However, in [BMIM][DCA] there is also a strongly bound layer, despite the fact that neither [BMIM]Cl nor Na[DCA] binds. We suggest that this [BMIM][DCA] involves cooperative binding of the cation and anion, with some indication from the zeta potential that anion binding predominates. The differences in binding of [MAT][DCA] and [MAT]I suggest that binding is cooperative in those systems as well. TGA measurements show that the IL bound to the nanoparticles decomposes at lower temperatures compared to the neat ILs. Surface coverage calculations confirmed the conclusion from XPS and IR that the capping layer for [MAT][DCA] is substantially thicker (at least ~3 times thicker) than that formed by [BMIM][DCA]. This research shows the potential importance of organic substituents

dx.doi.org/10.1021/jp3100409 | J. Phys. Chem. C 2013, 117, 5693–5707

in tailoring the desired specific surface interactions with metal nanoparticles.

While our data provide considerable insight into factors that influence formation of an effective IL capping layer, and data that would sensitively test models of IL−boron binding, true atomic-level detail regarding the IL−surface binding mechanism is not likely to come from experiments. For this reason, a theoretical study of the nature of IL−surface binding would be quite valuable.

■ ASSOCIATED CONTENT

Supporting Information

Additional XPS and TGA data. Detailed calculations of IL coverage of nanoparticles. This material is available free of charge via the Internet at http://pubs.acs.org.

■ AUTHOR INFORMATION

Corresponding Author

*E-mail: anderson@chem.utah.edu.

Notes

The authors declare no competing financial interest.

‖Senior Author.

■ ACKNOWLEDGMENTS

The authors acknowledge support from the Air Force Office of Scientific Research under AFOSR MURI Grant FA9550-08-1-0400 and from the University of Utah Research Foundation (grant 51003387). We would also like to acknowledge the CAMCOR TEM facility which is supported by grants from the W.M. Keck Foundation, the M.J. Murdock Charitable Trust, and the Oregon Nanoscience and Microtechnologies Institute. The AFRL group would like to acknowledge the Department of Defense High Performance Computing Modernization Program at the Air Force Research Laboratory, Engineering Research and Development Center, and Navy DoD Supercomputing Resource Centers for the computer time granted for the theoretical work. The University of Alabama group would like to thank the Air Force Office of Scientific Research (AFOSR Grant # FA9550-10-1-0521), and P.D.M. thanks the United States Department of Defense (DoD) through the National Defense, Science & Engineering Graduate Fellowship (NDSEG) Program.

■ REFERENCES

(1) Clark, J. D. *Ignition! An Informal History of Liquid Rocket Propellants*; Rutgers University Press: New Brunswick, NJ, 1972.

(2) Cardulla, F. *J. Chem. Educ.* **1983**, *60*, 505−508.

(3) MacEwen, J. D.; Vernot, E. H. *Toxic Hazards Research Unit Annual Technical Report: 1977*; University of California: Irvine: Dayton, OH, September, 1977.

(4) Renner, R. *Environ. Sci. Technol.* **2001**, *35*, 410A−413A.

(5) Magee, J. W.; Kabo, G. J.; Frenkel, M. In *Physical Property Measurements and a Comprehensive Data Retrieval System for Ionic Liquids*, 226th ACS National Meeting, New York, NY.

(6) Yang, Q.; Dionysiou, D. D. *J. Photochem. Photobiol. A: Chem.* **2004**, *165*, 229−240.

(7) Visser, A. E.; Swatloski, R. P.; Reichert, W. M.; Mayton, R.; Sheff, S.; Wierzbicki, A.; Davis, J. H.; Rogers, R. D. *Environ. Sci. Technol.* **2002**, *36*, 2523−2529.

(8) Welton, T. *Chem. Rev.* **1999**, *99*, 2071−2083.

(9) Chauvin, Y.; Olivier-Bourbigou, H. *CHEMTECH* **1995**, *25*, 26−30.

(10) Ngo, H. L.; LeCompte, K.; Hargens, L.; McEwen, A. B. *Thermochim. Acta* **2000**, *357*−*358*, 97−102.

(11) Zhang, Y.; Gao, H.; Joo, Y.-H.; Shreeve, J. M. *Angew. Chem., Int. Ed.* **2011**, *50*, 9554−9562.

(12) Chambreau, S. D.; Schneider, S.; Rosander, M.; Hawkins, T.; Gallegos, C. J.; Pastewait, M. F.; Vaghjiani, G. L. *J. Phys. Chem. A* **2008**, *112*, 7816−7824.

(13) Hawkins, T. W.; Schneider, S.; Drake, G. W.; Vaghjiani, G.; Chambreau, S. Hypergolic Fuels, US Pat. 8,034,202 B1, 2011.

(14) Schneider, S.; Hawkins, T.; Ahmed, Y.; Rosander, M.; Hudgens, L.; Mills, J. *Angew. Chem., Int. Ed.* **2011**, *50*, 5886−5888.

(15) Schneider, S.; Hawkins, T.; Rosander, M.; Vaghjiani, G.; Chambreau, S.; Drake, G. *Energy Fuels* **2008**, *22*, 2871−2872.

(16) Zhang, Y.; Shreeve, J. n. M. *Angew. Chem., Int. Ed.* **2011**, *50*, 935−937.

(17) Huzel, D. K.; Huang, D. H. *Modern Engineering for Design of Liquid-Propellant Rocket Engines*; American Institute of Aeronautics and Astronautics, Inc.: Reston, VA, 1992.

(18) Xue, H.; Gao, Y.; Twamley, B.; Shreeve, J. M. *Chem. Mater.* **2005**, *17*, 191−198.

(19) Gao, Y.; Arritt, S. W.; Twamley, B.; Shreeve, J. M. *Inorg. Chem.* **2005**, *44*, 1704−1712.

(20) Jin, C.-M.; Ye, C. F.; Piekarski, C.; Twamley, B.; Shreeve, J. M. *Eur. J. Inorg. Chem.* **2005**, *2005*, 3760−3767.

(21) Xue, H.; Arritt, S. W.; Twamley, B.; Shreeve, J. M. *Inorg. Chem.* **2004**, *43*, 7972−7977.

(22) Xue, H.; Twamley, B.; Shreeve, J. M. *J. Mater. Chem.* **2005**, *15*, 3459−3465.

(23) Ye, C.; Xiao, J.-C.; Twamley, B.; Shreeve, J. M. *Chem. Commun.* **2005**, 2750−2752.

(24) *Energetic Materials: Part 1. Decomposition, Crystal and Molecular Properties*; Elsevier: Amsterdam, The Netherlands, 2003.

(25) Fried, L. E.; Manaa, M. R.; Pagoria, P. F.; Simpson, R. L. *Annu. Rev. Mater. Res.* **2001**, *31*, 291−321.

(26) Politzer, P.; Murray, J. S.; Seminario, J. M.; Lane, P.; Grice, M. E.; Concha, M. C. *J. Mol. Struct. (Theochem)* **2001**, *573*, 1−10.

(27) Rice, B. M.; Pai, S. V.; Hare, J. *Combust. Flame* **1999**, *118*, 445−458.

(28) Hammerl, A.; Hiskey, M. A.; Holl, G.; Klapötke, T. M.; Polborn, K.; Stierstorfer, J.; Weigand, J. J. *Chem. Mater.* **2005**, *17*, 3784−3793.

(29) Katritzky, A. R.; Singh, S.; Kirichenko, K.; Holbrey, J. D.; Smiglak, M.; Reichert, W. M.; Rogers, R. D. *Chem. Commun.* **2005**, 868−870.

(30) Katritzky, A. R.; Singh, S.; Kirichenko, K.; Smiglak, M.; Holbrey, J. D.; Reichert, W. M.; Spear, S. K.; Rogers, R. D. *Chem. Eur. J.* **2006**, *12*, 4630−4641.

(31) Pogodina, N. V.; Metwalli, E.; Müller-Buschbaum, P.; Wendler, K.; Lungwitz, R.; Spange, S.; Shamshina, J. L.; Rogers, R. D.; Friedrich, C. *J. Phys. Chem. Lett.* **2011**, *2*, 2571−2576.

(32) Smiglak, M.; Bridges, N. J.; Dilip, M.; Rogers, R. D. *Chemistry* **2008**, *14*, 11314−9.

(33) Xue, H.; Gao, Y.; Twamley, B.; Shreeve, J. M. *Inorg. Chem.* **2005**, *44*, 5068−5072.

(34) Xue, H.; Twamley, B.; Shreeve, J. M. *J. Mater. Chem.* **2005**, *15*, 3459−3465.

(35) Cox, J. D.; Wagman, D. D.; Medvedev, V. A. *CODATA Key Values for Thermodynamics*; Hemisphere Publishing Corp: New York, 1984.

(36) Hsia, H. T.-S. *Air-Augmented Combustion of Boron and Boron-Metal Alloys*; Air Force Rocket Propulsion Laboratory, Air Force Systems Command, United States Air Force: Edwards, CA, 1971.

(37) Jain, A.; Anthonysamy, S.; Ananthasivan, K.; Gupta, G. S. *Thermochim. Acta* **2010**, *500*, 63−68.

(38) Jain, A.; Joseph, K.; Anthonysamy, S.; Gupta, G. S. *Thermochim. Acta* **2011**, *514*, 67−73.

(39) Kuo, K. K.; Risha, G. A.; Evans, B. J.; Boyer, E. *Mater. Res. Soc. Symp. Proc.* **2004**, 3−14.

(40) Mitani, T.; Izumikawa, M. *J. Spacecr. Rockets* **1991**, *28*, 78−84.

(41) Risha, G. A.; Boyer, E.; Evans, B.; Kuo, K. K.; Malek, R. *Mater. Res. Soc. Symp. Proc.* **2003**, *800*, 243−254.

(42) Young, G. *Metallic Nanoparticles as Fuel Additives in Airbreathing Combustion*; University of Maryland, Digital Repository at the University of Maryland, 2007.
(43) Hsieh, W.-H.; Peretz, A.; Huang, I.-T.; Kuo, K. K. *J. Propulsion* **1991**, *7*, 497−503.
(44) Van Devener, B.; Perez, J. P. L.; Anderson, S. L. *J. Mater. Res.* **2009**, *24*, 3462−3464.
(45) Van Devener, B.; Perez, J. P. L.; Jankovich, J.; Anderson, S. L. *Energy Fuels* **2009**, *23*, 6111−6120.
(46) Perez, J. P. L.; McMahon, B. W.; Anderson, S. L. *J. Propul. Power* **2013**, DOI: 10.2514/1.B34724.
(47) McCrary, P. D.; Beasley, P. A.; Cojocaru, O. A.; Schneider, S.; Hawkins, T. W.; Perez, J. P. L.; McMahon, B. W.; Pfeil, M.; Boatz, J. A.; Anderson, S. L.; Son, S. F.; Rogers, R. D. *Chem. Commun.* **2012**, *48*, 4311−4313.
(48) Wagner, C. D.; Naumkin, A. V.; Kraut-Vass, A.; Allison, J. W.; Powell, C. J.; John, R. Rumble, J. *NIST X-ray Photoelectron Spectroscopy Database*, June 6, 2000 ed.; Measurement Services Division of the National Institute of Standards and Technology (NIST) Material Measurement Laboratory (MML): Maryland, 2007.
(49) Perdew, J. P.; Adrienn, R.; Csonka, G. I.; Constantin, L. A.; Sun, J. *Phys. Rev. Lett.* **2009**, *103*, 026403.
(50) Krishnan, R.; Binkley, J. S.; Seeger, R.; Pople, J. A. *J. Chem. Phys.* **1980**, *72*, 650−654.
(51) Hariharan, P. C.; Pople, J. A. *Theor. Chim. Acta.* **1973**, *28*, 213−222.
(52) Clark, T.; Chandrasekhar, J.; Spitznagel, G. W.; Schleyer, P. v. R. *J. Comput. Chem.* **1983**, *4*, 294−301.
(53) Schmidt, M. W.; Baldridge, K. K.; Boatz, J. A.; Elbert, S. T.; Gordon, M. S.; Jensen, J. H.; Koseki, S.; Matsunaga, N.; Nguyen, K. A.; Su, S. *J. Comput. Chem.* **1993**, *14*, 1347−1363.
(54) Gordon, M. S.; Schmidt, M. W. *Advances in Electronic Structure Theory: GAMESS a Decade Later. In Theory and Applications of Computational Chemistry: The First Forty Years*; Elsevier: Amsterdam, 2005.
(55) Phillips, J. *Phys. Rev.* **1961**, *123*, 420−424.
(56) Smith, E. F.; Garcia, I. J.; Briggs, D.; Licence, P. *Chem. Commun. (Cambridge, U. K.)* **2005**, 5633−5.
(57) Smith, E. F.; Rutten, F. J. M.; Villar-Garcia, I. J.; Briggs, D.; Licence, P. *Langmuir* **2006**, *22*, 9386−9392.
(58) Hurisso, B. B.; Lovelock, K. R.; Licence, P. *Phys. Chem. Chem. Phys.* **2011**, *13*, 17737−48.
(59) Zhang, H.; Cui, H. *Langmuir* **2009**, *25*, 2604−2612.
(60) Zhang, Q.; Ma, X.; Liu, S.; Yang, B.; Lu, L.; He, Y.; Deng, Y. *J. Mater. Chem.* **2011**, *21*, 6864.
(61) Lovelock, K. R.; Kolbeck, C.; Cremer, T.; Paape, N.; Schulz, P. S.; Wasserscheid, P.; Maier, F.; Steinrück, H.-P. *J. Phys. Chem. B* **2009**, *113*, 2854−2864.
(62) Zhou, X.-L.; Blass, P. M.; Koel, B. E.; White, J. M. *Surf. Sci.* **1992**, *271*, 452−467.
(63) Moulder, J. F.; Stickle, W. F.; Sobol, P. E.; Bomben, K. D., *Handbook of X-ray Photoelectron Spectroscopy*; Perkin-Elmer Corporation: Eden Prairie, MN, 1992.
(64) Balakrishnarajan, M. M. *J. Am. Chem. Soc.* **2004**, *126*, 13119−13131.
(65) Carvalho, P. J.; Regueira, T.; Santos, L. M. N. B. F.; Fernandez, J.; Coutinho, J. A. P. *J. Chem. Eng. Data* **2010**, *55*, 645−652.
(66) Niedermaier, I.; Kolbeck, C.; Taccardi, N.; Schulz, P. S.; Li, J.; Drewello, T.; Wasserscheid, P.; Steinrück, H.-P.; Maier, F. *ChemPhysChem* **2012**, *13*, 1725−1735.
(67) Powell, C. J.; Jablonski, A. *NIST Electron Effective Attenuation Length Database*, 2003.
(68) Trehan, R.; Lifshitz, Y.; Rabalais, J. W. *J. Vac. Sci. Technol. A* **1990**, *8*, 4026−4032.
(69) Neouze, M.-A. *J. Mater. Chem.* **2010**, *20*, 9593−9607.
(70) Dupont, J.; Scholten, J. D. *Chem. Soc. Rev.* **2010**, *39*, 1790−1804.
(71) Khare, V.; Kraupner, A.; Mantion, A.; Jelicic, A.; Thunemann, A. F.; Giordano, C.; Taubert, A. *Langmuir* **2010**, *26*, 10600−5.
(72) Fonseca, G. S.; Machado, G.; Teixeira, S. R.; Fecher, G. H.; Morais, J.; Alves, M. C.; Dupont, J. *J. Colloid Interface Sci.* **2006**, *301*, 193−204.
(73) Ott, L. S.; Cline, M. L.; Deetlefs, M.; Seddon, K. R.; Finke, R. G. *J. Am. Chem. Soc.* **2005**, *127*, 5758−5759.
(74) Schrekker, H. S.; Gelesky, M. A.; Stracke, M. P.; Schrekker, C. M.; Machado, G.; Teixeira, S. R.; Rubim, J. C.; Dupont, J. *J. Colloid Interface Sci.* **2007**, *316*, 189−95.
(75) Mendonça, A. C. F.; Malfreyt, P.; Pádua, A. A. H. *J. Chem. Theory Comput.* **2012**, *8*, 3348−3355.
(76) Hendrickson, D. N.; Hollander, J. M.; Jolly, W. L. *Inorg. Chem.* **1969**, *8*, 2642−2647.
(77) Jagoda-Cwiklik, B.; Wang, X.-B.; Woo, H.-K.; Yang, J.; Wang, G.-J.; Zhou, M.; Jungwirth, P.; Wang, L.-S. *J. Phys. Chem. A* **2007**, *111*, 7719−7725.
(78) Peláez, R. J.; Blondel, C.; Delsart, C.; Drag, C. *J. Phys. B: At., Mol. Opt. Phys.* **2009**, *42*, 125001.
(79) Lotsch, B. V.; Senker, J.; Kockelmann, W.; Schnick, W. *J. Solid State Chem.* **2003**, *176*, 180−191.
(80) Kester, D. J.; Ailey, K. S.; Davis, R. F. *J. Mater. Res.* **1993**, *8*, 1231−1216.
(81) Verinaud, F.; Weissmantel, E.; Grenier, L.; Celerier, A.; Machet, J. *Thin Solid Films* **1992**, *209*, 59−66.
(82) McCrary, P. D.; Beasley, P. A.; Kelley, S. P.; Schneider, S.; Boatz, J. A.; Hawkins, T. W.; Perez, J. P. L.; McMahon, B. W.; Pfiel, M.; Son, S. F.; Anderson, S. L.; Rogers, R. D. *Phys. Chem. Chem. Phys.* **2012**, *14*, 13194−13198.
(83) Delgado, A. V.; González-Caballero, F.; Hunter, R. J.; Koopal, L. K.; Lyklema, J. Measurement and Interpretation of Electrokinetic Phenomena (IUPAC Technical Report). *Pure Appl. Chem.* **2005**, *77*, 1753−1805.
(84) Attard, P.; Antelmi, D.; Larson, I. *Langmuir* **2000**, *16*, 1542−1552.
(85) Paraknowitsch, J. P.; Zhang, J.; Su, D.; Thomas, A.; Antonietti, M. *Adv. Mater.* **2010**, *22*, 87−92.
(86) Wooster, T. J.; Johanson, K. M.; Fraser, K. J.; MacFarlane, D. R.; Scott, J. L. *Green Chem.* **2006**, *8*, 691−696.
(87) Weast, R. C.; Astle, M. J.; Beyer, W. H. *CRC Handbook of Chemistry and Physics*, 66 ed.; CRC Press: Boca Raton, 1985.
(88) Lowdin, P. O. *Adv. Quantum Chem.* **1970**, *5*, 185−199.
(89) Mulliken, R. S. *J. Chem. Phys.* **1955**, *23*, 1841.
(90) Mulliken, R. S. *J. Chem. Phys.* **1955**, *23*, 2338.
(91) Mulliken, R. S. *J. Chem. Phys.* **1955**, *23*, 2343.

CHAPTER 4

HYDROGEN LOADED BORON NANOPARTICLES: AN APPROACH TO POTENTIALLY IMPROVED COMBUSTIBILITY AND SPECIFIC IMPULSE

4.1 Overview

Ball milling of boron in an H_2 atmosphere was found to result in hydrogen uptake of up to 5 % by weight. The amount of incorporated hydrogen was analyzed by pyrolysis of the sample, and the nature of the hydrogen binding to boron was probed by a combination of IR spectroscopy, thermogravimetric analysis, and mass spectral measurements of gases evolved during sample heating. Hydrogen incorporated in the samples was found to be stable for at least a month at ambient conditions. Desorption is observed beginning at ~60 °C and continuing as the temperature is increased, with broad desorption features peaking at ~250 °C and ~450 °C, and ending at ~800 °C. The mass loss over this temperature range is ~6 wt%, but this includes some water and hydrocarbon contaminants present in the boron feedstock. Deuterium isotope labeling was used to distinguish between the hydrogen loaded in the milling process and the hydrogen-containing contaminants, and to probe H atom exchange. Unprotected hydrogenated boron nanoparticles were found to be reactive with O_2 producing a hydrated boron oxide surface layer that decomposed readily at 100 °C leading to desorption of H_2O.

4.2 Introduction

Boron's high heat of combustion makes it an interesting material for fuel and propellant applications.[1] Boron is quite refractory, thus combustion is inherently a heterogeneous process, limited by the surface area of the boron particles. Reduction of boron into the nanoscale can, therefore, improve combustibility;[2-4] however, formation of a refractory oxide layer on the particle surfaces upon air exposure, impedes ignition and reduces the energy density. One approach to mitigating the effects of the oxide layer is to cap nanoparticulate boron with organic capping ligands, which protect the boron from premature oxidation, and

control dispersibility in fuels/propellants.[5-8] Here, we examine a different approach to improving boron's potential as a propellant – production of boron nanoparticles containing up to 5 weight percent of hydrogen (~36 mole percent). Incorporation of hydrogen may have several effects. By reducing the average molecular weight of the combustion products, the specific impulse (I_{sp}) would be improved, all else being equal.[9] In addition, given the fact that boranes (B_nH_m compounds) tend to be highly reactive with oxidizers, hydrogenation of boron might be expected to increase reactivity. Given its low atomic mass and propensity for making compounds with hydrogen, boron also has potential as a hydrogen storage material. For example, diborane (B_2H_6) is 22 wt% hydrogen, surpassed only by methane (CH_4) in hydrogen content.

Hydrogen loading and adsorption properties of nanostructured solid boron compounds such as BN[10-11] and MgB_2[12] have been studied recently. Tang et al.[10] measured as much as 5.6 wt% hydrogen loading on mesoporous BN nanotubes, while Pecharsky et al.[12] were able to load ~4 wt% hydrogen into powdered MgB_2 via ball milling methods, producing $MgBH_4$ in the process. Fujii[13] conducted the first attempt to hydrogenate elemental boron powder through ball milling. Their results suggest that 2.3 wt% hydrogen loading was achieved after 80 h of milling under 10 atm of H_2.[13] There is some precedence for use of hydrogenation to improve ignitability of diesel fuel,[14] and the effects of hydrogen loading on conventional hydrocarbon fuels such as gasoline,[15] jet fuel[16] and natural gas[17-19] have also been studied. Results suggest that thermal efficiency was increased and fuel consumption was reduced when the optimum proportion of hydrogen is added. Furthermore, evidence of reduced CO emission was also observed for hydrogen enriched fuels.[16,19-20]

Here, ball milling was used to prepare boron nanoparticles and load them with up to 5 wt% hydrogen – comparable to the DOE target for hydrogen storage systems (5.5 wt% by

2017).[21] We show that the hydrogen remains incorporated into the boron samples when the H_2 pressure is removed, and use a variety of spectroscopic and mass spectrometric methods to probe how the hydrogen is bound, and the temperature required to release it. The effects of air exposure are also probed, showing that the hydrogen-loaded boron does, indeed, oxidize more readily than boron prepared under inert atmosphere.

4.3 Methodology

4.3.1 Hydrogen loading and nanoparticle production. Boron powder feedstock (~95 %, 2 μm diameter) was purchased from C. R. Supply Co. (West Hills, CA) and used as received, although some experiments aimed at purifying the boron feedstock are discussed below. Elemental boron powder is typically produced from borates by reduction with magnesium, followed by washing with HCl to dissolve excess magnesium. The boron is typically further purified by alkaline treatment followed by boiling in hydrofluoric acid, and then finally dried under vacuum, yielding boron powder with 94 – 95 % purity (2 – 4 % magnesium and 1.2 – 1.5 % of undissolved residue as contaminants).[22] The use of acids during the purification process may potentially represent a source of hydrogen in the feedstock. As described below, elemental analysis of our feedstock showed ~0.4 weight percent hydrogen content. As described in Appendix C, we attempted to remove hydrogen and other contaminants by heating the feedstock at 400 °C under vacuum; however, while we did see desorption of H_2 and other hydrogen-containing species, a significant amount of hydrogen remains in the feedstock after more than 12 hours of treatment (Figure C3). Hydrogen loading was accomplished by milling boron powder in an H_2 atmosphere. In a typical milling procedure, 2 g of boron and 160 g of 1/8 inch diameter tungsten carbide media were loaded into a 500-mL tungsten carbide-lined milling jar. The jar lid was modified with two valved ports which allow the jar atmosphere to be pumped out, purged, filled, and

sampled, without breaking the lid seal. After loading, the jar is sealed and then pumped out and purged with Ar three times, before finally pumping out the Ar and charging the jar with H_2 gas (99.95 % purity, Airgas USA, LLC, Denver, CO). For most experiments the absolute H_2 charge pressure was 60 psia (~4 atm). The reactants and the tungsten carbide media were milled using a PM 400 planetary ball mill (Retsch, Inc., Haan, Germany) for a total of 16 hours at 300 rpm. The milling program consisted of 30-minute milling periods with 5 minute rest/cooling intervals, reversing the milling direction between each cycle. The pressure of H_2 inside the jar was monitored at intervals during the milling process by stopping the mill and connecting a gauge to one of the ports in the jar lid, pumping out the gauge, and then opening the valve to allow measurement of the internal pressure. For deuterium-loading experiments, the same set of procedures was employed with the use of D_2 gas instead of H_2. Control experiments were performed with H_2 as the jar atmosphere, but without boron added, and with boron but with argon as the milling atmosphere.

Unless noted, all manipulations of the boron, including loading and unloading the jar, and transfer of samples for various analyses, were performed in an N_2-filled glove box to minimize exposure to air. Gas sampling was also done inside the glovebox such that the jar atmosphere was never exposed to air.

4.3.2 Hydrogen content analysis. Hydrogen uptake was determined in two ways. The most straightforward was simply measuring the drop in H_2 pressure in the milling jar over the course of the milling run. This measurement allows the total hydrogen uptake to be calculated, but provides no insight into the form in which the hydrogen is bound. Therefore, we also analyzed the hydrogen loading of the resulting particles using a high-temperature-conversion elemental analyzer (TC/EA) coupled to a Thermo Finnigan Delta V Plus Isotope Ratio Mass Spectrometer (IRMS) (Thermo Fisher Scientific Inc., Waltham,

MA) through an open split interface. For this analysis, a sample of the solid milling product was transferred to a sample vial, and from the vial a sample was dropped into a He carrier stream, which carried the sample through a 1400 °C glassy carbon pyrolytic reactor, forming H_2 in the process. Gases are separated in a 1 m long gas chromatography column (5A, 80 mL/min, 95 °C) before entering the IRMS for quantitation of the H_2. Ultrahigh purity H_2 was injected at appropriate times during analysis to ensure proper mass and sensitivity calibration.

4.3.3 Particle characterization. Particle size and shape were analyzed using scanning electron microscopy (SEM-FEI Nova Nano 600, Hillsboro, OR). Samples for SEM were prepared by sonicating and dispersing the particles in ethanol to break up aggregates. Particles were then drop cast and dried on a transmission electron microscopy (TEM) grid, which was affixed to the SEM sample holder using carbon tape. These samples were exposed to air during transfer to the SEM. In addition, a scanning TEM was used to examine the particles. This analysis was done using a FEI Technai Osiris instrument (FEI Co., Hillsboro, OR) at 200 kV operation. Electron energy loss spectroscopy (EELS) was used to verify that the particles examined were boron.

4.3.4 Fourier transform infrared (FTIR) analysis. A Nicolet iS5 FTIR spectrometer (Thermo Fisher Scientific, Waltham, MA) was used to collect infrared (IR) spectra using an attenuated total reflectance (ATR) set-up. Dry milled boron samples were directly pressed onto the instrument's diamond crystal. IR spectra were obtained with a resolution of 1 cm^{-1} in 15 independent scans, and then averaged.

4.3.5 Mass spectrometry analysis. After milling selected samples, headspace gas was analyzed using a quadrupole mass spectrometer system with base pressure below 10^{-8} mbar. The gas was sampled by connecting a sealed glass tube to the milling jar's valve port. To

avoid N_2 introduction from the glove box atmosphere, the glass tube was first purged by pumping out and filling it with Ar repeatedly, before the headspace gas was collected. The glass tube was then valved off, and connected to the inlet system of the mass spectrometer. The dead volume between the valves on the sample tube and mass spectrometer inlet was evacuated, and then the valves were opened to allow headspace gas to enter the mass spectrometer ion source.

Mass spectra were also measured for gases evolved from samples of H_2- and D_2-loaded boron nanoparticles as they were heated. For these measurements, the jar was opened in the glove box, and a boron powder sample was collected and transferred into a glass sample tube equipped with a valve. The boron-filled tube was then connected to the mass spectrometer inlet manifold, and gases were continuously leaked into the instrument as the sample tube was slowly heated using a tube furnace, thereby obtaining mass spectra of gases evolving as the temperature was raised.

The detection sensitivity of mass spectrometers typically varies with mass, and for light gases like hydrogen, the effect can be substantial. To ensure that the compositions reported for the headspace and evolved gases are accurate, the sensitivity of the mass spectrometer used in these analyses was calibrated by measuring the intensities for H_2, D_2, and Ar, independently introduced into the mass spectrometer at constant pressure, as measured by an ionization gauge, and corrected for the gauge's detection sensitivity. The spectra presented below have been corrected for variation of sensitivity with mass.

4.3.6 Tandem thermogravimetric-mass spectrometry analysis (TGA-MS). Mass losses as a function of temperature were studied using a thermogravimetry instrument, also equipped with a mass spectrometer for analysis of the evolved gases. Samples were prepared and analyzed with a TA Model Q500 Thermogravimetric Analyzer operated inside a N_2-filled

glovebox. Samples were heated from 25 °C to 900 °C at a constant temperature ramp rate of 10 °C/min under N_2 gas flow (90 mL/min). Mass analysis was done simultaneously with TGA by sampling the gas stream with a Pfeiffer ThermoStar GSD301T3 quadrupole mass spectrometer (Pfeiffer Vacuum, Nashua, NH) which allowed monitoring specific masses of interest as a function of sample temperature.

Oxidation of hydrogenated boron samples as a function of temperature was studied using a TA Model 2950 Thermogravimetric Analyzer (TA Instruments, New Castle, DE) operated outside the glovebox and flowing O_2 into the furnace and the sample balance. Because this TGA was located outside the glove box, the samples for oxidation analysis were, necessarily, exposed to air during transfer to the instrument. This instrument was not equipped with a mass spectrometer.

4.4 Results and Discussion

4.4.1 Quantifying hydrogen loading in boron. Hydrogen uptake was monitored throughout the milling process by measuring the pressure drop inside the milling jar at intervals, until the pressure stabilized after ~15 hours of milling, indicating that H_2 had essentially saturated the particles. Figure 4.1a shows the pressure drop inside the milling jar, for three sets of conditions. Data are shown for milling of 2 g of boron and 160 g of tungsten carbide media in 60 psi (4 atm) initial H_2 pressure. For comparison, analogous pressure versus time data are given for identical milling runs where either the boron was omitted, or the jar was filled with argon instead of H_2. For the run with H_2 and boron, the absolute pressure dropped by nearly a factor of three over the 15 hour milling run. In contrast, there was no significant pressure drop for the run with boron in argon, showing that boron does not absorb argon significantly. The jar pressure was also constant for the

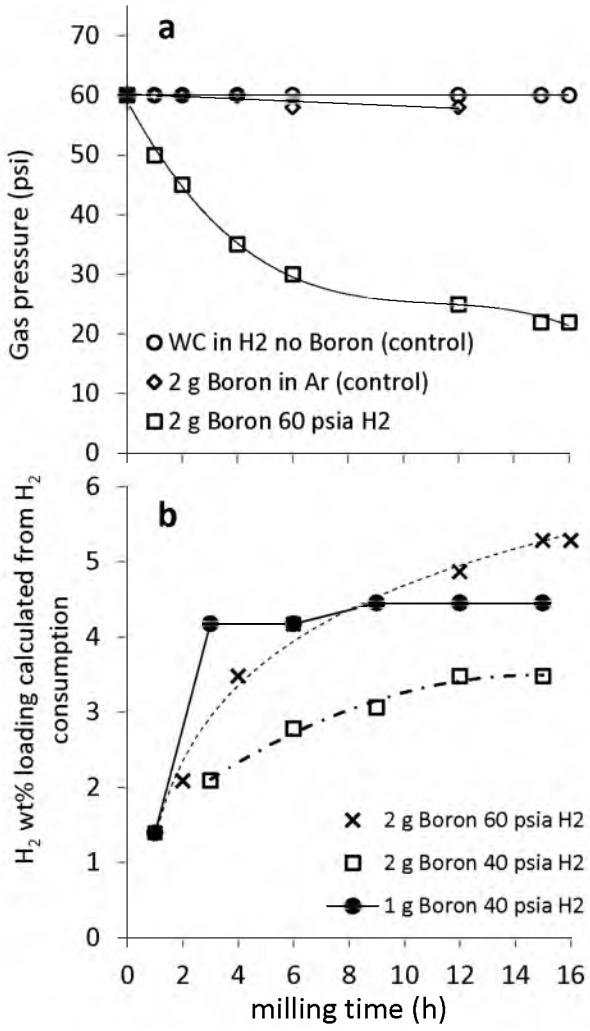

Figure 4.1 **(a.)** Pressure drop of H_2 inside the jar measured at different intervals during the milling. **(b.)** H_2 consumed during the milling as weight percent of boron loading.

run with H_2 but no boron, showing that that the jar seal is not permeable to H_2, and that the tungsten carbide media and jar lining do not take up any significant amount of hydrogen.

Several different experiments were carried out varying the initial boron feedstock mass and H_2 charge pressure, and the results were summarized in Figure 4.1b, where the H_2 pressure drops have been converted to the equivalent H_2 uptake, expressed as H_2 consumed as a weight percent (wt%) of the initial boron mass in each experiment. The H_2 weight

percent consumed varied from ~3 wt% to 5 wt%, increasing with increasing ratio of H_2 to boron in the initial jar loading. We have not attempted milling at higher H_2 pressures due to limitations of the jar seal design, however, we note that the H_2 uptakes observed here are higher than the 2 – 3 wt% hydrogen loadings observed in previous studies that used higher H_2 pressures and much longer milling times (70 – 145 psi, 80 – 100 h).[13,23]

An obvious question is whether the hydrogen taken up by the boron during milling, remains in the sample when the H_2 overpressure is removed. Therefore, we also directly measured the hydrogen content of one of the milled samples using TC/EA, as described above. For this analysis the sample used was one where the H_2 loading calculated from the pressure drop during milling was 3.4 wt%. TC/EA analysis found evolution of 3.5 wt% of H_2 when the sample was heated to 1400 °C. It is important to note, however, that the TC/EA instrument is not equipped with an inert sample transfer system, thus the sample was exposed to air. Air exposure might result in some hydrogen loss from the boron due to oxidation of the boron particle surface, but might also lead to uptake of hydrogen in the form of atmospheric water or other hydrogen-containing contaminants. Therefore, a sample of the boron feedstock was also analyzed by TC/EA resulting in a measured hydrogen content of ~0.4 wt%. The TC/EA analysis shows, therefore, that milling boron in H_2 increased the hydrogen content by at least ~3.1 wt%. The extra hydrogen content is slightly lower than the 3.4 wt% uptake inferred from the pressure drop during milling, however, lack of quantitative agreement is not surprising given the possible effects of air exposure prior to TC/EA analysis. We tentatively conclude, therefore, that the H_2 pressure drop really does reflect some process by which H_2 is taken up by the boron under milling conditions, binding in such a way that it is not lost under ambient conditions.

4.4.2 Potential mechanisms for H_2 uptake by boron. Before discussing experiments designed to probe the nature of the hydrogen binding in the H_2-loaded samples, we first briefly outline several possibilities. The first point to consider is the magnitude of the hydrogen uptake, which ranges up to 5 wt% – close to the 5.5 wt% hydrogen storage target set by DOE for 2017 on-vehicle storage. Given the atomic weights of H (1.008 g/mole) and B (10.81 g/mole), 5 wt% corresponds to ~36 mole %, or a stoichiometry of 1 H atom for every ~1.8 B atoms. There are several mechanisms that could result in such high hydrogen uptakes.

One possibility is that boron reacts with H_2 under milling conditions to bind to the boron surface, presumably by dissociating and forming B−H bonds, reminiscent of those found in borane compounds. If we assume that B−H bond formation occurs only on the surfaces of the particles, and that every surface B atom has a single H atom bound to it, then this scenario would require that ~56 % of the B atoms be on the surface layer – corresponding to 1200 m^2 of available surface binding sites per gram of boron, assuming that the density of milled product is equal to that of the amorphous boron feedstock (2.37 g/cm^3). If spherical, the particles would have to have an average diameter of ~2 nm to have such high surface area/g.

Another possibility is that hydrogen might react with boron under milling conditions to generate stable borane molecules. For example, if we assume that the H_2 reacts with boron to produce diborane gas (B_2H_6), the result would be a pressure drop of a factor of three (at 100 % conversion), in reasonable agreement with observation (Figure 4.1a). Formation of less volatile higher molecular weight boranes such as tetraborane ($B_4H_{10(g)}$), pentaborane ($B_5H_{9(\ell)}$) or decaborane ($B_{10}H_{14(s)}$) would result in larger pressure drops, for a given extent of conversion. Most of these species have significant vapor pressures, and therefore should be

observable by mass spectrometry of the milling jar headspace, or of gases evolved when samples are heated, as described below.

Finally, it is possible that some hydrogen is taken up by interstitial sites in the boron particle bulk. Several of the isomorphs of crystalline boron are built of hollow B_{12} icosahedra, and it is known that amorphous boron also includes randomly oriented B_{12} icosahedra.[24] The presence of such structures raises the possibility that either atomic or molecular hydrogen might bind to, or become physically trapped in the interior of the icosahedra. It is not clear what the signature of such interior hydrogen would be experimentally. Density functional theory (DFT) calculations are currently being conducted to determine the energetics involved in such binding sites.

4.4.3 IR and XPS spectroscopy. Infrared spectroscopy provides a valuable probe of B−H bonding in milled samples, and an example spectrum is shown in Figure 4.2. Unfortunately, the FTIR instrument was not equipped for inert sample introduction, and therefore this sample was exposed to air prior to analysis. The boron oxidation state in air-exposed samples was probed by X-ray photoelectron spectroscopy (XPS), as shown in Figure 4.3. Most of the XPS signal comes from the top ~6 nanometers of the boron surface,[6] thus the appearance of a substantial peak for B^{3+} at 193 eV is consistent with the sample having a thin oxidized surface layer, passivating the unoxidized core of the particles, which gives rise to the large peak for B^0 at 188 eV. The binding energy for B^{3+} in materials such as B_2O_3, $B(OH)_3$ and various borates is quite similar,[25] thus XPS provides no information on the hydration state of the oxidized layer.

The infrared spectrum (Figure 4.2) of the oxidized H_2-loaded boron is dominated by strong bands assigned to B−O stretching (1434 cm^{-1}) and O−H stretching (3202 cm^{-1}) vibrations.[26] The strength of the O−H stretch band suggests a significant degree of

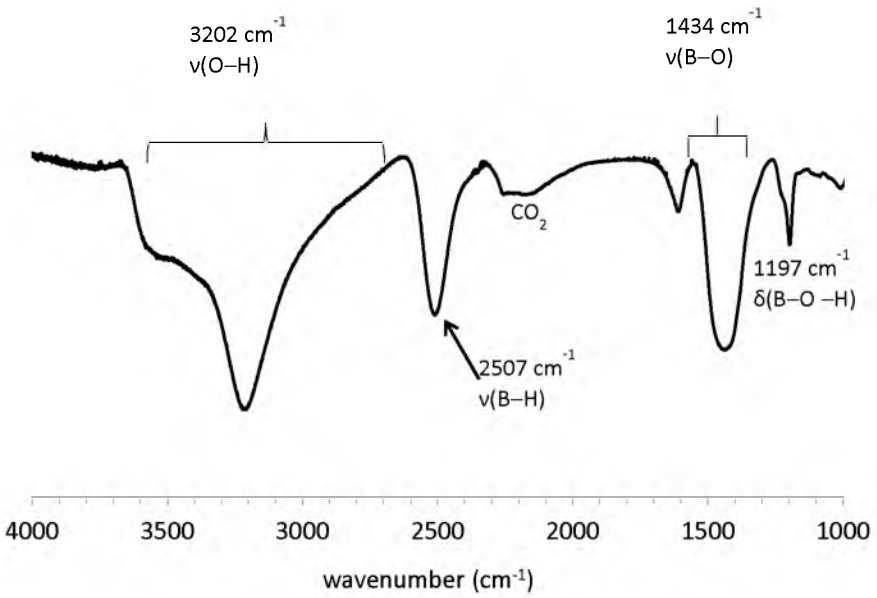

Figure 4.2 FTIR spectrum of hydrogenated boron nanoparticles produced after milling.

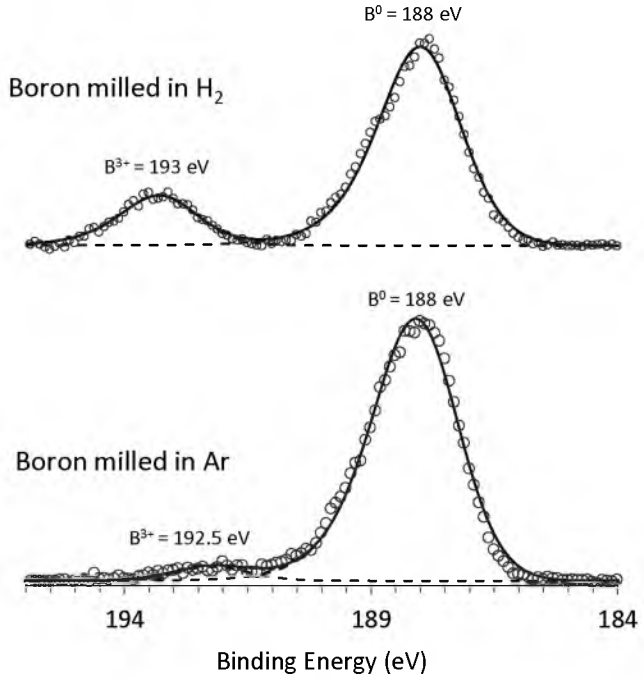

Figure 4.3 B 1s Region XPS of H_2-milled (top) and Ar-milled (bottom) boron nanoparticles exposed to air prior to analysis.

hydroxylation, i.e., the surface oxide layer appears to be partially hydrated. The IR spectrum also shows a strong peak at 2507 cm^{-1}, which is in the range typically seen for B−H stretching vibrations in borane compounds,[27] confirming that at least some of the hydrogen is in the form of H atoms covalently bound to boron. The B−H stretch frequency for H atoms bound to B atoms on the surface of solid boron is not known, but might be expected to be similar to B−H stretches in boranes. The IR spectrum, therefore, does not rule out formation of boranes as the mechanism for hydrogen uptake under milling conditions, although to survive transfer in air to the FTIR instrument, such boranes would have to be both nonvolatile and air-stable, ruling out any of the low molecular weight boranes.[28] Further evidence on the borane issue is presented below.

Note also that IR data do not rule out the possibility of the hydrogen incorporated as H_2, either via some form of nondissociative chemisorption, or by interstitial trapping in the boron particle bulk. Such molecular H_2 might not be IR active, or might have signatures that overlap with the strong O−H band.

4.4.4 Comparison with boron milled under other conditions. As shown in Figure 4.3, the relative intensity of the B^{3+} peak in the XPS of boron that was dry-milled in H_2 and subsequently exposed to air, is ~5 times greater than that observed for boron dry-milled in argon or N_2 atmosphere prior to air exposure. This observation indicates that the concentration of oxidized boron in the surface region of the samples, as prepared for XPS, is significantly higher for the H_2-milled sample. For bulk boron, air exposure results in formation of a self-limiting oxide layer ~0.4 nm thick,[6] while XPS samples the top ~6 nm of the sample (see Supporting Information). The greater extent of boron oxidation for the H_2-milled sample may indicate that hydrogen loading increases thickness of the self-limiting oxide layer, perhaps by increasing the permeability of the initial oxide layer to O_2. Greater

oxidation would also be explained if H_2-milling changed the morphology of the resulting particles. If, for example, the H_2-milled boron contained a larger fraction of particles in the few nanometer thickness range, XPS would "see through" the particles and detect the oxide layer on both surfaces. Similarly, if the H_2-milled particles were rougher, with nanometer scale asperities, then a larger fraction of the XPS-detectable surface region would oxidize on air exposure. We note that high oxidized (B^{3+}) boron intensity is also seen in XPS of boron milled under Ar or N_2, but with hexane added as a wetting agent.[6] Generally, size reduction is more efficient when wetting agents are used, because they help keep the particles well dispersed in the mill, and reduce cold welding of particles.[6] The hydrogen uptake under H_2-milling conditions is sufficiently large that it is not unreasonable to expect that there might be changes in the physical and chemical properties, which might aid size reduction or reduce cold welding.

Figure 4.4 compares SEM images of boron nanoparticles obtained by dry milling in Ar and H_2 atmospheres. The Ar-milled nanoparticles are noticeably more compact, compared to the H_2-milled sample, where the particles appear quite irregular, and where there is clearly a larger population of the smallest size particles. The highly irregular structure of the larger particles is likely a sign that these are actually aggregates of the smaller, primary particles. Such morphology differences, compared to the Ar-milled particles, would tend to result in a larger fraction of exposed, oxidized surface, relative to the unoxidized bulk.

Boron, because it is a low Z element, is difficult to study in TEM, but Figure 4.4c also shows a TEM image of one of the small particles generated by H_2-milling. Electron energy loss spectroscopy was used to verify that the particle was boron. The fact that the contrast is relatively constant across most of this particle suggests that it has a flat, plate-like structure. The areas of higher contrast to the upper left and upper right of the particle indicate thicker

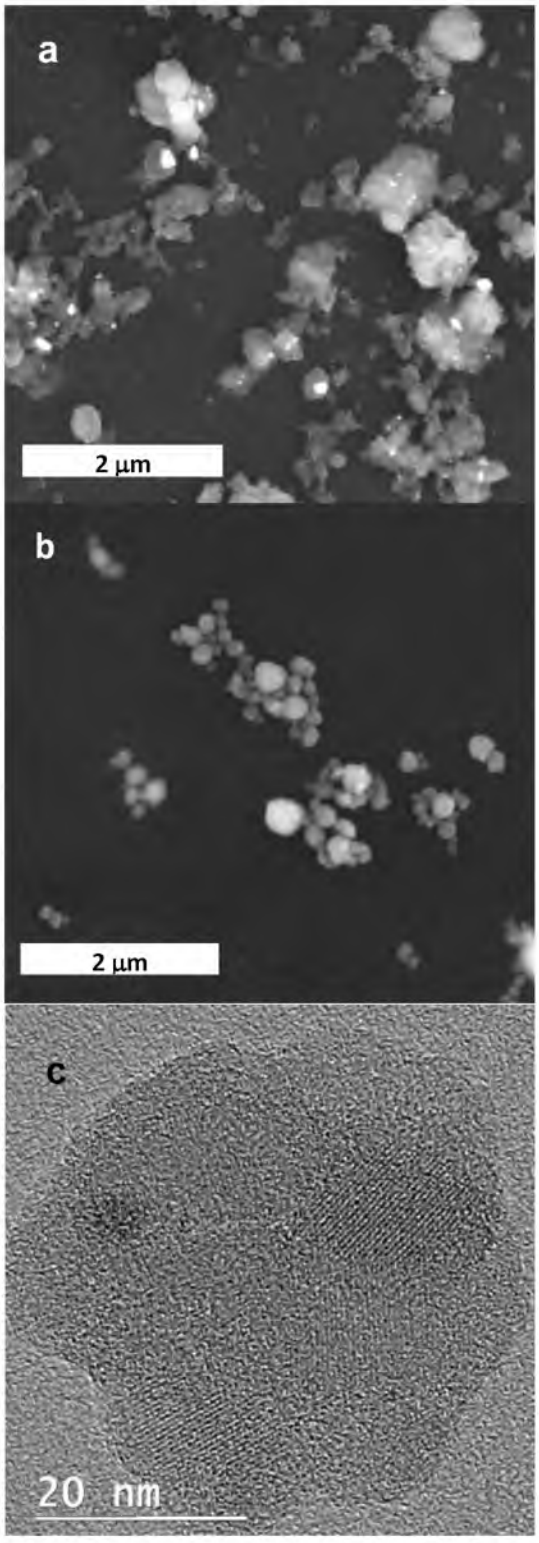

Figure 4.4 SEM images of boron nanoparticles produced from dry milling in **(a.)** H_2 atmosphere, and **(b.)** Ar atmosphere. **(c.)** TEM image of boron nanoparticle milled in H_2.

regions, which are tentatively ascribed to smaller particles binding to the main particle, such that the aggregate thickness is higher.

While the poor contrast in TEM of boron makes imaging difficult, the apparent high surface area/volume ratio of the plate-like primary particles might help explain why the H_2-milled samples are able to take up such a high hydrogen loading, and also explain the higher degree of oxidation upon exposure to air.

4.4.5 Mass spectrometry of headspace and desorbing gases. As noted, both the hydrogen uptake and the appearance of B−H bonds in the IR spectrum could result either from H atoms chemisorbed on the boron particle surface, or to formation of boranes. Low molecular weight boranes such as $B_2H_{6(g)}$, $B_4H_{10(g)}$, and $B_5H_{9(l)}$ are volatile and highly reactive. They are unlikely to survive in the air-exposed IR sample, however, boranes could still form in H_2-milling, and if so, their high H:B stoichiometries might partially account for the high H_2 uptake observed in milling.

Mass spectrometry was, therefore, used to look for the signature of volatile boranes in the milling jar headspace gas, and also in gases evolved from the boron samples during heating. To avoid destruction of reactive boranes, the mass spectrometry experiments summarized in Figure 4.5 and 4.6 were done carefully, avoiding air exposure. Figure 4.5 shows a typical mass spectrum of the headspace gas collected from the jar after milling in H_2. For this experiment, argon was added to the initial gas mixture at a 12:1 H_2:Ar ratio, in order to have a known concentration of Ar in the headspace as an intensity standard. As expected, the headspace spectrum included prominent peaks from H_2 (m/q = 2) and Ar (m/q = 40), as well as numerous small peaks attributed to organic ions, attributable to organic contaminants in the boron feedstock (see below). There are two interesting features

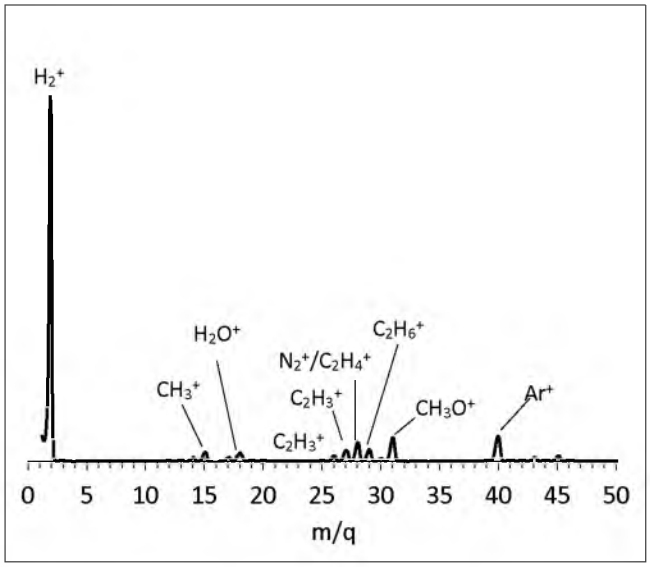

Figure 4.5 Mass spectrum of headspace gas collected from the jar after milling for 16 hours.

of the spectrum. There is a set of small peaks (m/q = 18, 17, 16) indicating the presence of water. Some water is expected because the 95 % pure boron feedstock is known to contain water, but one might also expect that oxygen present in the boron feedstock might react with H_2 to form water under milling conditions. Evolution of water and isotope labeling experiments are discussed below.

More importantly, the mass spectrum provides no evidence for the presence of volatile boranes. Such boranes all have characteristic patterns of peaks corresponding to stable $B_xH_y^+$ stoichiometries, and reflecting the 5:1 ^{11}B:^{10}B natural abundance.[27] For example, under electron impact conditions similar to ours, standard mass spectra of stable B_nH_m ($n \leq 6$) compounds all show substantial peaks at m/q = 11, which is absent in our spectrum. Furthermore, the borane spectra include families of $B_xH_y^+$ peaks that lie in m/q ranges (23 – 27, 33 – 38, 44 – 50) where there is essentially no signal in our spectra. We conclude, therefore, that the B–H covalent bonds observed in the IR spectrum, and the high hydrogenuptake, do not result from formation of low molecular weight boranes, but rather

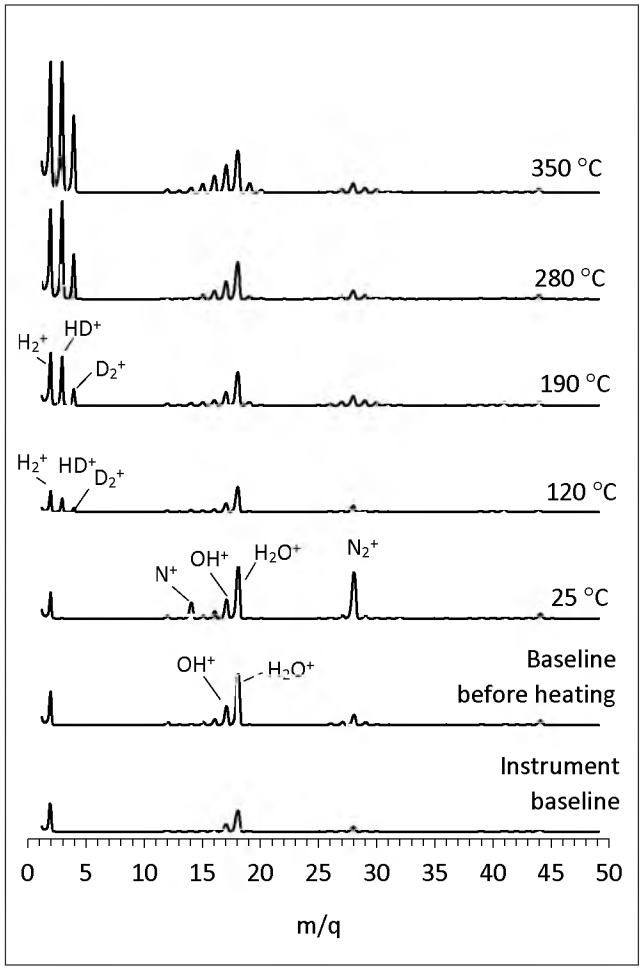

Figure 4.6 Mass spectra of gases evolved from deuterated boron nanoparticles heated to 350 °C.

from covalent bonding of H atoms to the boron nanoparticles. This conclusion reinforced the obtained results from the TC/EA hydrogen analysis (where volatiles would have been lost before analysis), which showed that the amount of hydrogen stably bound to the samples is comparable to the amount inferred from hydrogen uptake during milling.

Mass spectrometry was also used to monitor gases evolved from the particles as they were heated to 350 °C. To help distinguish between hydrogen introduced by milling from hydrogen present as feedstock contaminants such as water and hydrocarbons, the gas evolution experiments were performed using boron milled in a D_2 atmosphere. The first

point of interest is that the amount of D_2 taken up by the boron, as determined from pressure decreases during milling, is the same as the uptake observed when milling with H_2, indicating that there are no significant deuterium isotope effects on the loading process, or on H versus D binding to the boron. After preparation of the D_2-loaded sample, the jar was opened in the glovebox, and a sample of the D_2-loaded boron powder was loaded into a glass tube (thus allowing volatiles such as D_2 to escape). The tube valve was closed in the glovebox, then connected to the mass spectrometer inlet system, which was evacuated to avoid air exposure, prior to opening the valve to allow gas sampling.

Figure 4.6 shows the results. At the bottom, two spectra are given showing typical instrument baseline data. The bottom spectrum, taken at the beginning of the day, shows the signal for hydrogen (m/q = 2), water (m/q = 18, 17, 16), CO/N_2 (m/q = 28), and CO_2 (m/q = 44). The second baseline spectrum was taken just before the start of the heating series, and shows significantly elevated water signal (m/q = 18, 17, 16) as a result of water introduction during previous experiments that day. The spectrum labeled 25 °C shows the gases from the sample container before heating was started, and the only significant signal, compared to the preheating baseline, is from glovebox nitrogen (m/q = 28, 14) trapped in the sample container. There is no evidence of H_2, HD, or D_2 evolving from the sample at room temperature.

The sample was then heated to 350 °C, slowly enough (5 hours) to ensure that the temperature throughout the powdered sample was reasonably homogeneous. During this slow heat ramp, the gases evolved from the sample were continuously pumped out via the instrument inlet system, with mass spectra recorded at selected temperatures. Therefore the spectra represent snapshots of the gasses evolving at particular temperatures during the heat ramp.

By the time the 120 °C spectrum was recorded (~30 minutes), little N_2 remained in the sample, as shown by negligible m/q = 28 signal. In addition, the water signals also decreased by ~60 % relative to the preheating baseline, reflecting a combination of loss of water from the sample, and slow recovery of the instrument baseline water signal. More importantly, the spectrum shows small signals for HD, and D_2 evolving from the sample. Interestingly, there is no evidence for D_2O or HDO evolution at either 25 °C or 120 °C, where desorption of molecularly bound water might be expected. This absence suggests that water is not formed by reaction of the hydrogen milling atmosphere with oxides initially present in the boron feedstock. Furthermore, we can infer that H_2O, known to be present as a contaminant in the feedstock, does not undergo exchange with D bound to the boron.

As the temperature increased, the signals for H_2, HD, and D_2 increase significantly, dominating the mass spectra. The large H_2 signal is attributed to significant hydrogen contamination of the feedstock, as discussed above and in Appendix C. This hydrogen apparently combines with deuterium loaded during milling to generate all three isotopologs of H_2. For propellant and fuels application, such "extra" hydrogen does not cause any deleterious effects; however, it does complicate the mass analysis to some extent.

The intense HD signal in Figure 4.6 indicates that isotope scrambling is reasonably efficient, which suggests, in turn, that most of the desorbing hydrogen is produced by recombination of H and D dissociatively chemisorbed to the boron. At higher temperatures, small peaks at m/q = 19 and 20 were observed, suggesting that there begins to be some water desorbing by recombination of dissociated species such as H and OH, thus allowing isotope scrambling. With increasing temperature, a number of peaks attributed to hydrocarbon species, originating from contaminants in the boron feedstock, begin to appear. See the discussion in Appendix C for additional information about hydrocarbon and water

contaminants of the boron, and use of vacuum heating to reduce the contaminant level substantially.

Finally, the results in Figure 4.6 show no signs of boranes evolving from the sample in the temperature range up to 350 °C. The m/q = 11 signal seen for all boranes[27] is not observed, for example. The fragment ion patterns for deuterated boranes have not been reported to our knowledge, but would be broadened and shifted to higher mass, compared to the known spectra[27] for all -H boranes. For example, the prominent $B_3H_x^+$ (x = 0 – 5) peaks seen for tetraborane and pentaborane would appear in the range m/q = 33 to 43, and while there are some small peaks in this mass range, the intensity pattern is not consistent with $B_3D_xH_y^+$ ions, and suggests, instead, that the origin is fragment ions from the hydrocarbon contaminants.

4.4.6 Thermogravimetric analysis with mass spectrometry (TGA-MS). To probe mass loss quantitatively, and to examine gas evolution over a wider temperature range, samples prepared by milling in D_2 atmosphere were characterized with TGA-MS, and the results are given in Figure 4.7. It is important to note that these samples were never exposed to air, and TGA was done inside a nitrogen glovebox, therefore, any hydrogen- or oxygen-containing species observed in the analysis are the result of contaminants in the boron feedstock. When considering these results, it is important to keep in mind several limitations of the instrument. It was only possible to monitor a small set of ion masses during the TGA heat ramp, which were chosen as H_2^+, D_2^+, H_2O^+, D_2O^+, B^+ and $B_2D_5^+$. The latter two masses would be indicative of signal from deuterated boranes, and have little or no contribution from cracking of hydrocarbon ions. In addition, the mass spectral sensitivity of the TGA-MS instrument was found to be a strong function of mass. In particular, the sensitivity decreased rapidly at low m/q, affecting our ability to monitor H_2 and D_2 evolution.

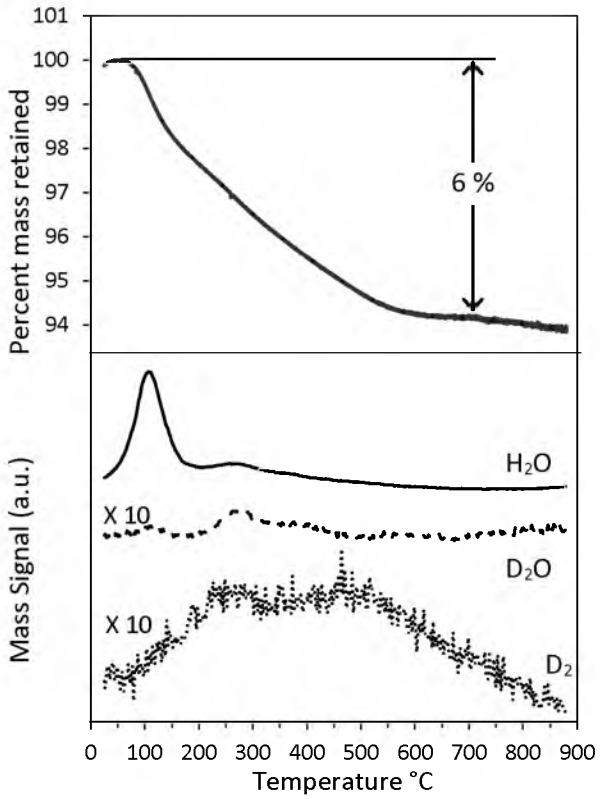

Figure 4.7 TGA profile of deuterated boron nanoparticles with corresponding desorption signal of H_2O, D_2O, and D_2 monitored through the run. TGA analysis was done inside a glovebox under inert atmosphere.

No signal was observed for H_2^+, even though the mass spectra in Figure 4.6, where sensitivity was calibrated, show this to be a major product ion. The signal for D_2^+ was sufficient to allow TGA-MS measurements, but comparison with Figure 4.6 indicates that the D_2^+ sensitivity is at least 25 times lower than that for H_2O^+, which was the most intense mass spectral signal observed.

The top frame of Figure 4.7 shows the percent mass change versus temperature, and the raw ion intensities for D_2^+, D_2O^+, and H_2O^+ are shown in the bottom frame. A rapid ~1.5 % mass loss was observed between ~100 °C and 150 °C, and the mass spectral results suggest that ~1 % corresponds to desorption of undeuterated water attributed to water in the boron

feedstock. A somewhat slower mass loss continued as the sample was heated up to 900 °C, totaling ~6 %, or ~5 % if the contribution from water is subtracted. The pressure drop during production of this sample was consistent with ~6 wt% deuterium loading, thus the mass loss, not including water, was about 1 % less than expected. This may simply indicate that higher temperatures would be required to lose all the deuterium. The mass spectral results (Figure 4.6) indicate that the primary loss was of D_2, HD, and H_2, although only D_2 could be monitored in the TGA-MS. The D_2 desorption temperature dependence shows evidence of two broad features, peaking at ~270 °C and ~480 °C. These have previously been attributed to recombinative desorption from sites with terminal B−D and bridging B−D−B bonds, respectively,[13] although the FTIR results above show no evidence for bridge-bonded hydrogen. Clearly, the hydrogen loaded into boron by milling is strongly bonded, with temperatures well over 600 °C required to desorb it all. The high desorption temperature would clearly be problematic for hydrogen storage applications; however, for applications in propellants or fuels, the strong B−H binding is advantageous, ensuring that the hydrogen is not lost during storage. Under combustion conditions, the hydrogen would be consumed as the boron burned, presumably increasing the I_{sp} by generating more low molecular weight products. There is also the possibility that presence of hydrogen on the boron surface might significantly enhance ignition, because, by analogy with boranes, the B−H bonds are likely to be reactive with oxidizers.

The D_2O intensity trace is also interesting. During the strong initial pulse of water desorption around 120 °C, there is little if any D_2O desorption, however, there are also weak water desorption features between ~250 °C and 400 °C, and both H_2O and D_2O are observed in these. These TGA-MS results are consistent with the conclusion reached above, that milling in D_2 does not result in significant production of molecularly adsorbed

deuterated water. The water desorption peak around 120 °C corresponds to desorption of this molecularly adsorbed water with no isotope exchange, while the higher temperature desorption feature corresponds to recombinative desorption, where H/D scrambling is facile. This two-stage water desorption behavior is somewhat reminiscent of water desorption from boric acid (H_3BO_3).[29]

4.3.7 Reactivity with oxygen. Reactivity of hydrogenated boron nanoparticles with oxygen was investigated by monitoring mass gain as samples were heated under an O_2 gas flow using a TGA system. Figure 4.8 compares results for samples of hydrogen-milled and argon-milled boron. For Ar-milled boron, the sample mass was essentially constant up to about 100 °C, and then there was a slow increase totaling ~1 % as the temperature was ramped up to ~400 °C. At that point, the rate of mass gain increased, reaching a maximum at 500 °C, before tapering off above ~550 °C. For this sample, which was transferred to the TGA in air, the boron particles are coated and passivated by a thin oxide layer, as shown by the XPS results in Figure 4.3. For temperatures well below the B_2O_3 melting temperature (450 °C), slow mass gain is expected because diffusion of oxygen through the solid oxide layer is slow. As the oxide approaches and passes its melting point, oxygen diffusion becomes fast, and the oxide layer grows at an increasing rate, with concomitant increase in mass. The temperature range probed is well below the oxide sublimation temperature (1500°C) thus the oxidation products remain on the particle surface, thickening the oxide layer, and leading to eventual slowing of the mass gain rate.

The particular H_2-milled sample used in this experiment had ~3.5 wt% of hydrogen uptake, resulting in B−H bond formation on the particle surfaces, and possibly other hydrogen incorporated in other sites. The XPS data in Figure 4.3 shows that when such H_2-milled samples are exposed to air, the fraction of oxidized boron in the surface region is

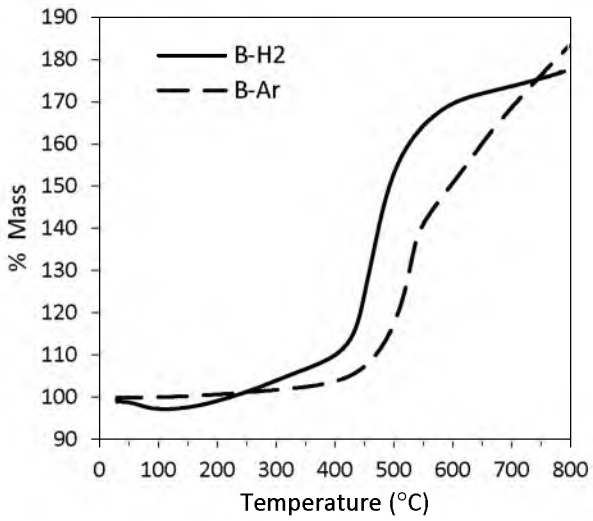

Figure 4.8 TGA analysis of boron milled in H_2 and Ar run under O_2 atmosphere.

substantially greater than in the Ar-milled sample. This increased oxidation could indicate that incorporated hydrogen increases reactivity toward oxygen, but also could reflect increased surface area (Figure 4.4). When hydrogenated boron oxidizes, it could form B_2O_3 (as in unhydrogenated boron), but one might expect that the surface would consist of hydrated forms of the oxide, such as $B(OH)_3$, HBO_2, or $H_2B_4O_7$, which form in oxidation of boranes.[30-31] The presence of some degree of hydration is confirmed by the strong OH stretching signal observed in the IR spectrum of oxidized, H_2-milled boron (Figure 4.2).

As such a sample is heated, the surface layer would tend to dehydrate, leading to an initial mass loss, and just such an initial mass loss of 3 % is observed as the sample was heated to 100 °C. Note, however, that the mass loss stops well below the temperature expected for complete dehydration to B_2O_3 (250 °C for bulk boron oxide), and mass begins to increase again above 100 °C. Furthermore, the rate of mass gain in the 100 °C to ~420 °C temperature range is five times faster than the rate observed for the Ar-milled sample. Again, faster oxidation of the H_2-milled boron is attributed to some combination of higher reactivity

of the hydrogen-loaded boron, and higher surface area. For the H_2-milled sample, the transition to rapid mass gain occurs at ~420 °C, compared to ~500 °C for Ar-milled boron, and in addition, the transition is more abrupt and the subsequent rate of mass gain is faster than for the Ar-milled sample. All three of these factors suggest that the changes in surface properties resulting from H_2 milling, should lead to more facile ignition of H_2-milled boron under combustion conditions.

4.5 Conclusions

Boron nanoparticles were prepared and loaded with hydrogen using ball milling procedure as a means to further increase energy density, improve specific impulse, and enhance combustibility. We showed that as much as 5 wt% of hydrogen can be loaded into boron nanoparticles through this process, and mass spectrometry and TGA experiments all show that the incorporated hydrogen is stable up to ~100 °C. FTIR experiments indicate that hydrogen binds to boron in the form of B−H covalent bonds, similar to those observed in boranes. Mass spectroscopy and TGA-MS analyses show no evidence for formation of molecular boranes that are volatile in the temperature range probed. Detailed examination of the desorption process showed that hydrogen desorbs mostly as H_2 gas with a smaller amount desorbing from oxidized samples as H_2O formed by recombination and desorption from hydrated oxides. Under inert atmosphere, most of the hydrogen desorbs from the boron below ~550 °C. Together with the observation that H_2-milled boron also oxidizes more readily than boron without hydrogen loading, this result suggests that hydrogen-loaded boron might significantly improve ignition, combustion, and I_{sp} of boron-loaded propellants. Calculations exploring the nature of boron-hydrogen binding and experiments examining the ignition of H_2-milled boron are needed to further evaluate the potential as a propellant additive.

References

(1) Cox, J. D.; Wagman, D. D.; Medvedev, V. A. *Codata Key Values for Thermodynamics*. Hemisphere Publishing Corp: New York, 1984.

(2) Plantier, K. B.; Pantoya, M. L.; Gash, A. E. Combustion Wave Speeds of Nanocomposite Al/Fe_2O_3: The Effects of Fe_2O_3 Particle Synthesis Technique *Combust. Flame* **2005,** *140*, 299-309.

(3) Armstrong, R. W.; Baschung, B.; Booth, D. W.; Samirant, M. Enhanced Propellant Combustion with Nanoparticles. *Nano Lett.* **2003,** *3*, 253-255.

(4) Wang, L. L.; Munir, Z. A.; Maximov, Y. M. Review Thermite Reactions: Their Utililzation in the Synthesis and Processing of Materials. *J. Mat. Sci.* **1993,** *28*, 3693-3708.

(5) Van Devener, B.; Perez, J. P. L.; Anderson, S. L. Air-Stable, Unoxidized, Hydrocarbon-Dispersible Boron Nanoparticles. *Journal of Materials Research* **2009,** *24*, 3462-3464.

(6) Van Devener, B.; Perez, J. P. L.; Jankovich, J.; Anderson, S. L. Oxide-Free, Catalyst-Coated, Fuel-Soluble, Air-Stable Boron Nanopowder as Combined Combustion Catalyst and High Energy Density Fuel. *Energy Fuels* **2009,** *23*, 6111-6120.

(7) Perez, J. P. L.; McMahon, B. W.; Anderson, S. L. Functionalization and Passivation of Boron Nanoparticles with a Hypergolic Ionic Liquid. *J. Propul. Power* **2013,** *29*, 489-495.

(8) Perez, J. P. L.; McMahon, B. W.; Schneider, S.; Boatz, J. A.; Hawkins, T. W.; McCrary, P. D.; Beasley, P. A.; Kelley, S. P.; Rogers, R. D.; Anderson, S. L. Exploring the Structure of Nitrogen-Rich Ionic Liquids and Their Binding to the Surface of Oxide-Free Boron Nanoparticles. *J. Phys. Chem. C* **2013,** *117*, 5693-5707.

(9) Silvera, I. F.; Cole, J. W. Metallic Hydrogen: The Most Powerful Rocket Fuel yet to Exist. *J. Phys. Conf. Ser.* **2010,** *215*, 012194.

(10) Li, J.; Lin, J.; Xu, X.; Zhang, X.; Xue, Y.; Mi, J.; Mo, Z.; Fan, Y.; Hu, L.; Yang, X.; Zhang, J.; Meng, F.; Yuan, S.; Tang, C. Porous Boron Nitride with a High Surface Area: Hydrogen Storage and Water Treatment. *Nanotechnology* **2013,** *24*, 155603.

(11) Weng, Q.; Wang, X.; Zhi, C.; Bando, Y.; Golberg, D. Boron Nitride Porous Microbelts for Hydrogen Storage. *ACS Nano* **2013,** *7*, 1558-1565.

(12) Gupta, S.; Hlova, I. Z.; Kobayashi, T.; Denys, R. V.; Chen, F.; Zavaliy, I. Y.; Pruski, M.; Pecharsky, V. K. Facile Synthesis and Regeneration of $Mg(Bh_4)_2$ by High Energy Reactive Ball Milling of Mgb_2. *Chem. Commun.* **2013,** *49*, 828-30.

(13) Wang, P.; Orimo, S.; Tanabe, K.; Fujii, H. Hydrogen in Mechanically Milled Amorphous Boron. *J. Alloys Compd.* **2003,** *350*, 218-221.

(14) Tilton, J. A.; Smith, W. M.; Hockerberger, W. G. Production of High Cetane Number Diesel Fuels by Hydrogenation. *Ind. Eng. Chem.* **1948,** *40*, 1269-1273.

(15) Ji, C.; Wang, S.; Zhang, B. Performance of a Hybrid Hydrogen–Gasoline Engine under Various Operating Conditions. *Applied Energy* **2012,** *97*, 584-589.

(16) Clayton, R. M. Hydrogen Enrichment for Low-Emission Jet Combustion. *Adv. Chem. Ser.* **1978,** *166*, 267-286.

(17) Ghenai, C.; Zbeeb, K.; Janajreh, I. Combustion of Alternative Fuels in Vortex Trapped Combustor. *Energy Convers. Manage.* **2013,** *65*, 819-828.

(18) Ma, F.; Wang, Y.; Liu, H.; Li, Y.; Wang, J.; Zhao, S. Experimental Study on Thermal Efficiency and Emission Characteristics of a Lean Burn Hydrogen Enriched Natural Gas Engine. *Int. J. Hydrogen Energy* **2007,** *32*, 5067-5075.

(19) Khalil, A. E. E.; Gupta, A. K. Hydrogen Addition Effects on High Intensity Distributed Combustion. *Applied Energy* **2013,** *104*, 71-78.

(20) Guo, H.; Hosseini, V.; Neill, W. S.; Chippior, W. L.; Dumitrescu, C. E. An Experimental Study on the Effect of Hydrogen Enrichment on Diesel Fueled Hcci Combustion. *Int. J. Hydrogen Energy* **2011,** *36*, 13820-13830.

(21) *Department of Energy Hydrogen and Fuel Cells Program Plan*; U.S. Department of Energy: 2011.

(22) Zhigach, A. F.; Stasinevich, D. C. *Methods of Preparation of Amorphous Boron. Boron and Refractory Borides*, Matkovich, V. I., Ed. Springer-Verlag: New York, 1977; pp 214-226.

(23) Huang, Z.; Calka, A.; Liu, H. Dsc Study of the Effect of Milling Conditions on the Hydrogen Storage Properties of Boron. *J. Mat. Sci.* **2007,** *42*, 3985-3989.

(24) Kobayashi, M.; Higashi, I.; Takami, M. Fundamental Structure of Amorphous Boron. *J. Solid State Chem.* **1997,** *133*, 211-214.

(25) Moulder, J. F.; Stickle, W. F.; Sobol, P. E.; Bomben, K. D.; J. Chastain & R. C. King, J., eds. *Handbook of X-Ray Photoelectron Spectroscopy*. Vol. p Physical Electronics: Eden Prarie, MN, 1995.

(26) Peak, D.; Luther, G. W. I.; Sparks, D. L. Atr-Ftir Spectroscopic Studies of Boric Acid Adsorption on Hydrous Ferric Oxide. *Geochim. Cosmochim. Acta* **2003,** *67*, 2551-2560.

(27) Linstrom, P. J.; Mallard, W. G. *Nist Chemistry Webbook, Nist Standard Reference Database Number 69*. National Institute of Standards and Technology: Gaithersburg MD, 20899, 2011.

(28) Yaws, C. L. *Handbook of Vapor Pressure*. Vol. 4, p Gulf Publishing Co.: Houston, TX, 1995.

(29) Balcı, S.; Sezgi, N. A.; Eren, E. Boron Oxide Production Kinetics Using Boric Acid as Raw Material. *Ind. Eng. Chem. Res.* **2012,** *51*, 11091-11096.

(30) Roth, W.; Bauer, W. H. The Explosive Oxidation of Diborane. *J. Phys. Chem.* **1956,** *60*, 639-641.

(31) Ludlum, K. H.; Wiberley, S. E.; Bauer, W. H. *The Oxidation of Tetraborane.* Dissertation, Rensselaer Polytechnic Institute, 1961.

CHAPTER 5

SUMMARY AND FUTURE DIRECTION OF THE RESEARCH

This research focused on the development of a method that enables us to tap boron's high energy potential as liquid fuel and propellant additive. To mitigate the problem of slow combustion and incomplete burning, particles in the nanometer size regime were produced through various ball milling procedures. The unwanted formation of refractory surface oxide was prevented with the use of organic capping molecules which also served as dispersing agents. Here, we were able to show that oleic acid and ionic liquids with functional groups that are strongly interacting with boron atoms can be effective in protecting elemental boron from oxidation in air. We also showed that by milling boron with hydrogen, a significant amount of H_2 can be stably loaded into the boron nanoparticles. Hydrogen content is comparable to the target loading of the Department of Energy. By hydrogen milling, we observed that a more reactive surface is produced due to the formation of terminal B–H bonds. This is particularly important in the chemistry of the organic ligands with the boron surface. It allows us to use a wider range of organic compounds (i.e., alkenes and alkynes) that are initially unreactive with boron, and also eliminates the prerequisite of using oxygen- and nitrogen-containing functional groups. This opens a large number of avenues in studying the interaction of boron and other organic compounds, which consequently expands the possible uses of nanoparticulate boron in other applications such as in cancer therapy (boron neutron capture therapy) and hydrogen storage.

APPENDIX A

ADDITIONAL DATA FOR CHAPTER 2

A.1 Effect of Multiple Ethanol Washing on Boron Nanoparticles Coated with Oleic Acid

Boron nanoparticles functionalized with oleic acid are typically washed with ethanol through a series of centrifuge-sonication cycles to remove excess free molecules that may interfere with SEM imaging and XPS analysis. The effect of multiple washings (5 repeated cycles) on the surface bound oleic acid is observed in FTIR. Figure A.1 shows an FTIR spectra for a series of washing cycle.

A.2 Quantitation of Oleic Acid on Surface of Nanoparticle Using TGA

Assuming a minimum particle size of 80 ± 30 nm (from the SEM image), the total percent mass loss obtained from TGA was converted to mass of oleic acid as follows:

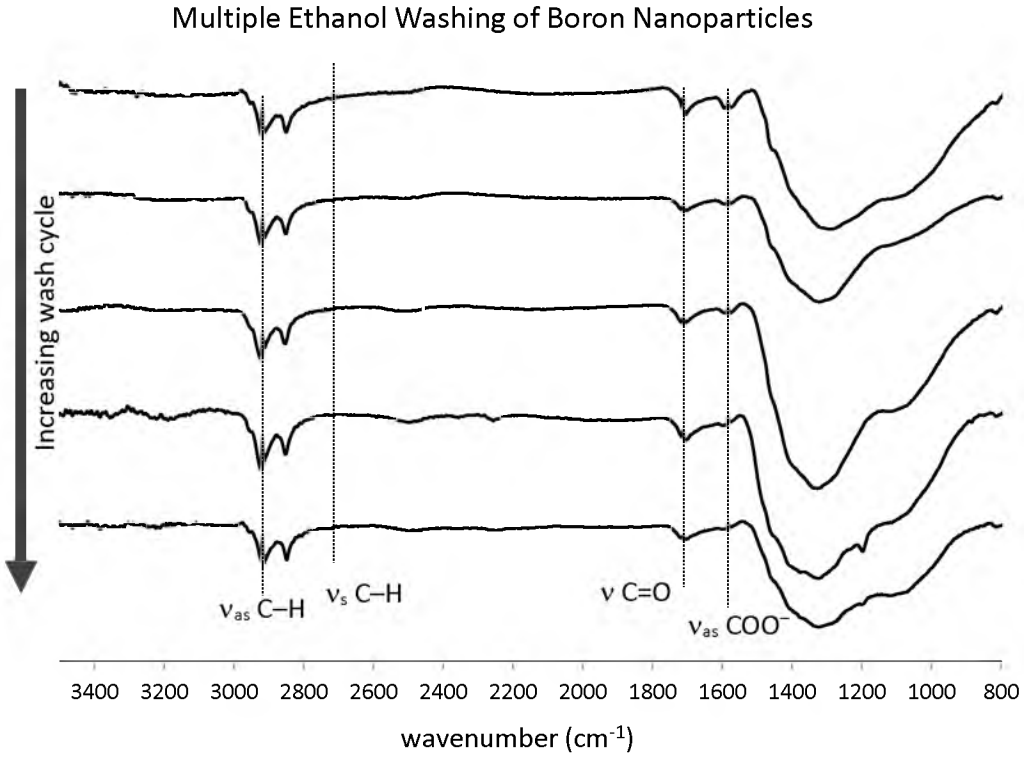

Figure A.1 FTIR spectra of boron nanoparticles washed through a series of sonication and centrifugation with ethanol.

A.2.1 Mass of boron per particle (fg) $= \left(\frac{4}{3}\pi r^3\right) \times \left(\rho_{Boron}\right)$

$= \left[\frac{4}{3}\ \pi\ (4.5 \times 10^{-6}\ \text{cm})^3\right] \times\ (2.34\ \text{g/cm}^3)$

$= 6.3 \times 10^{-16}\ \text{g}$

$= 0.63\ \text{fg}$

Error calculation $= 0.63 \times \sqrt{3\left(\frac{15}{40}\right)^2}$

$= 0.41\ \text{fg}$

$=$ **0.63 ± 0.41 fg**

A.2.2 Mass of oleic acid per particle (fg) $= \left(\frac{\text{mass of B per particle}}{\text{mass \% B}}\right)$ % mass loss

$= \left(\frac{0.63\ \text{fg}}{75\%}\right) 25\%$

$= 0.021\ \text{fg}$

Error calculation $= 0.021 \times \sqrt{\left(\frac{0.41}{0.63}\right)^2 + \left(\frac{1}{25}\right)^2 + \left(\frac{1}{75}\right)^2}$

$= 0.014\ \text{fg}$

$=$ **0.021 ± 0.014 fg**

A.2.3 Mass of oleic acid per nm^2 (fg) $= \frac{\text{mass of oleic acid/particle}}{4\pi r^2}$

$= \frac{0.021\ \text{fg}}{4\ \pi\ (40\ \text{nm})^2}$

$= 1.0 \times 10^{-5}\ \text{fg/nm}^2$

Error calculation $= (1.0 \text{x} 10^{-5}) \times \sqrt{\left(\frac{0.04}{0.05}\right)^2 + 2\left(\frac{15}{40}\right)^2}$

$= 0.9 \text{ x } 10^{-5}\ \text{fg/nm}^2$

= **(1.0 ± 0.9) x 10^{-5} fg/nm^2**

A.2.4 No. of oleic acid molecules per nm^2

$$= \frac{\left(\text{mass of oleic acid per particle (g)} \Big/ \text{FW oleic acid (g/mol)}\right) \times N_A}{4\pi r^2}$$

$$= \frac{\left(5.0 \times 10^{-17}\ \text{g} \Big/ 282.5\ \text{g/mol}\right) \times 6.02 \times 10^{23}\ \text{oleic acid molecules/mol}}{4\ \pi\ (40\ \text{nm})^2}$$

= 22 oleic acid molecules/nm^2

$$\text{Error calculation} = 22 \times \sqrt{\left(\frac{0.014}{0.021}\right)^2 + 2\left(\frac{15}{40}\right)^2}$$

= 21 oleic acid molecules/nm^2

= **22 ± 18 oleic acid molecules/nm^2**

A.2.5 From A.2.4 the number of oleic acid layer can be calculated assuming that the oleic acid polar head has an area of 0.24 nm^2.[1]

Monolayer Coverage = (area covered by a single molecule) × (no of oleic acid mol/nm^2)

IL parallel to the surface = (0.24 nm^2/molecule) × (14 molecules/nm^2)

= 5.3 oleic acid monolayers

Error calculation = 0.24 × 18

= 4.3 monolayers

A.3 Particle Size, Morphology and Reactivity in O_2 of Hydrogenated Boron Nanoparticles as compared to Ar-milled Boron

Figure A.2 shows the effect of H_2 milling of boron nanoparticles prior to surfactant milling with octane. The presence of H_2 gas during the milling process produces terminal B−H bonds on the particle surface, which enhance the reactivity with octene. The presence of the alkyl group is confirmed by the increased dispersibility of the particles in a nonpolar solvent, i.e., hexane (Figure A.2a). This behavior is not observed with particles produced from dry milling with Ar followed by surfactant milling in octene (Figure A.2b). Figure A.3 shows SEM images of these particles. Aggregation is significantly observed on samples dry milled with Ar.

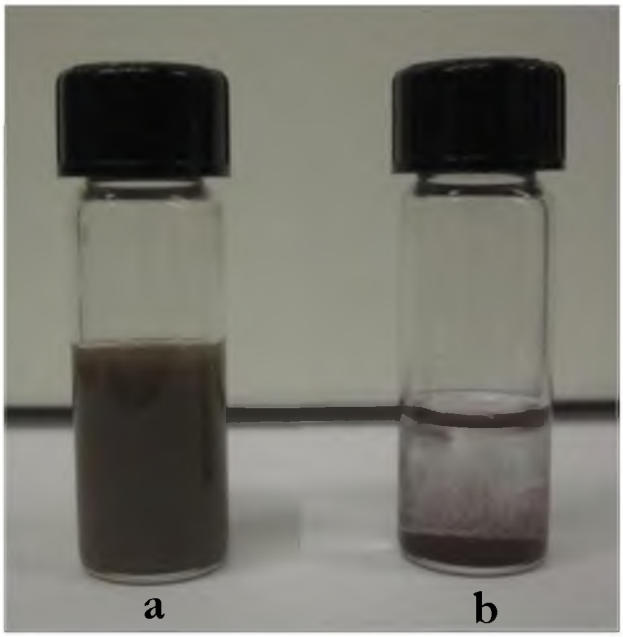

Figure A.2 Boron nanoparticles milled in H_2 and octene **(a)** show more stable dispersion in hexane than boron milled in Ar and octene **(b)**.

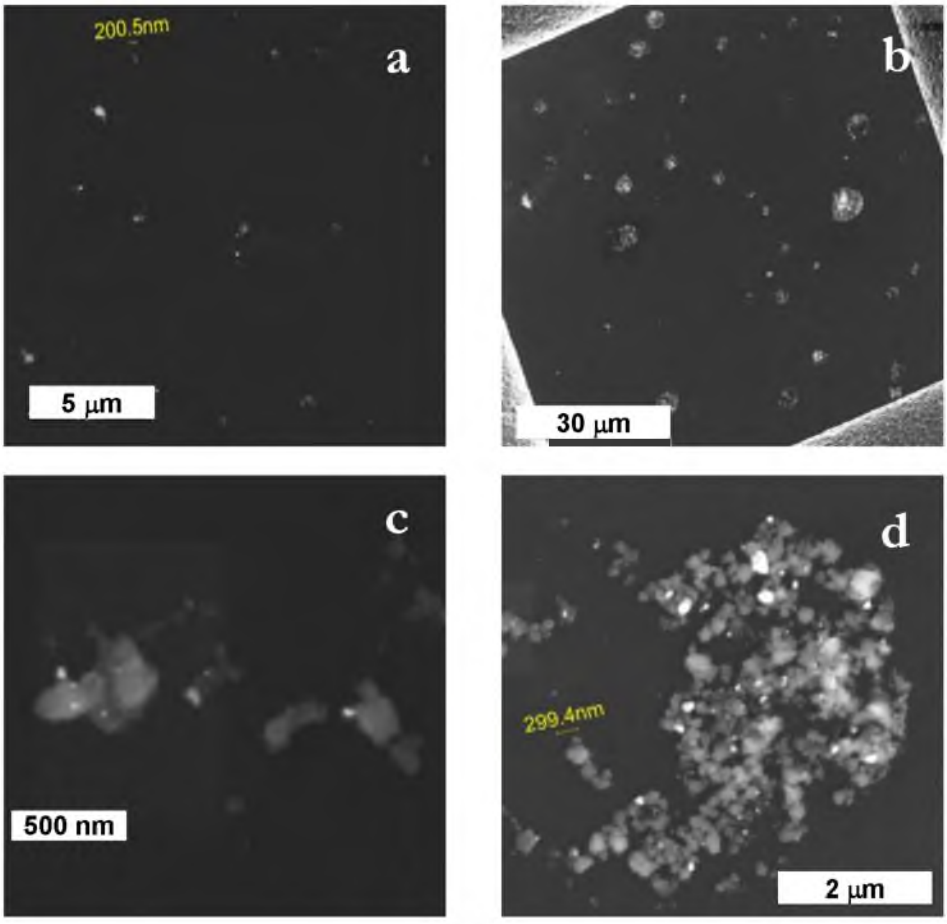

Figure A.3 SEM images of boron milled in H_2 **(a and c)** and boron milled in Ar **(b and d)** showing highly aggregated particles when dispersed in hexane.

A.4 References

(1) Zhang, L.; He, R.; Gu, H.-C. Oleic Acid Coating on the Monodisperse Magnetite Nanoparticles. *Appl. Surf. Sci.* **2006,** *253*, 2611-2617.

APPENDIX B

ADDITIONAL DATA FOR CHAPTER 3

B.1 Effects of Sputtering on XPS data

For XPS analysis of samples exposed to air prior to introduction into the XPS vacuum system, sputtering is often used to remove material from sample surfaces, which typically includes carbonaceous contaminants from adventitious sources, or other chemically modified surface layers. This process exposes a relatively "clean" sample surface for analysis, and allows identification of the adventitious carbon peak, which is often used as a reference in calibrating the binding energy scale that may be affected by differential charging of the sample. The following series of high resolution XPS spectra (Figures B.1 – B.11) displays the effect (if any) of sputtering cycles on N 1s and C 1s binding energy peaks of the neat ILs, the reference salts and the IL-functionalized boron samples. Note that in

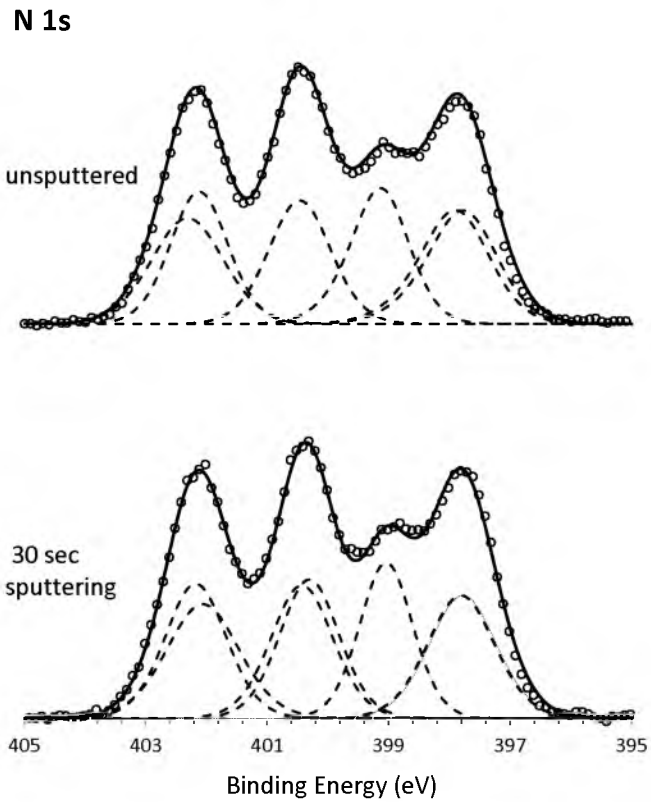

Figure B.1 N 1s high resolution XPS of [MAT][DCA] before and after sputtering.

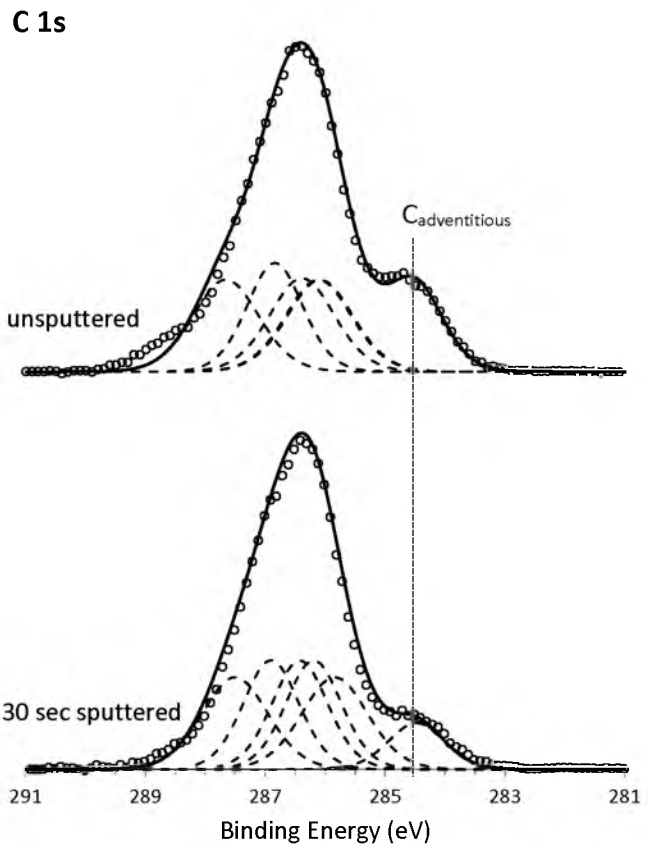

Figure B.2 C 1s high resolution XPS of [MAT][DCA] before and after sputtering.

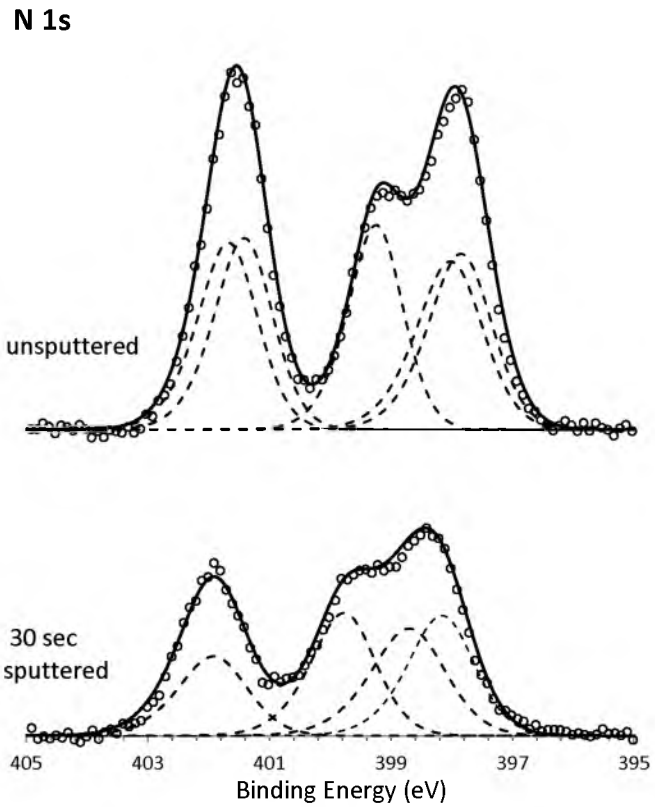

Figure B.3 N 1s high resolution XPS of [BMIM][DCA] before and after sputtering.

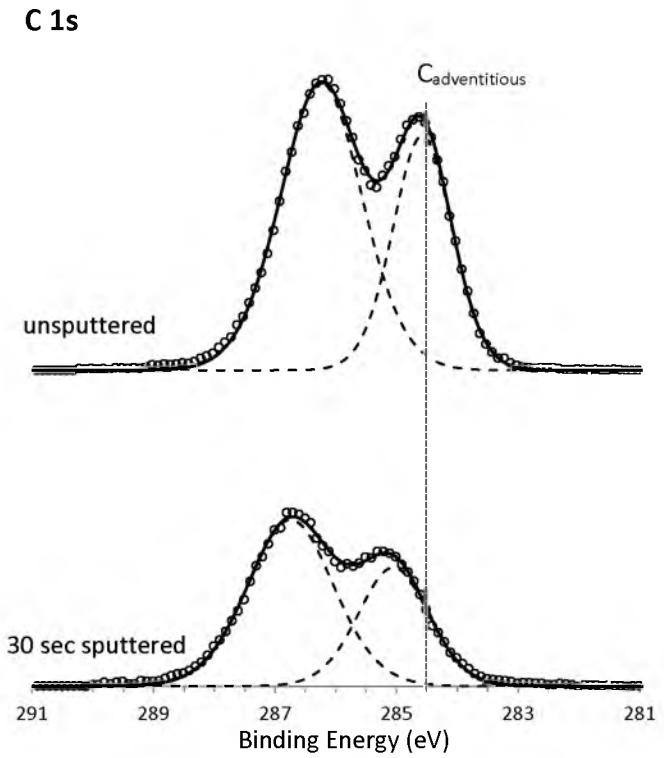

Figure B.4 C 1s high resolution XPS of [BMIM][DCA] before and after sputtering.

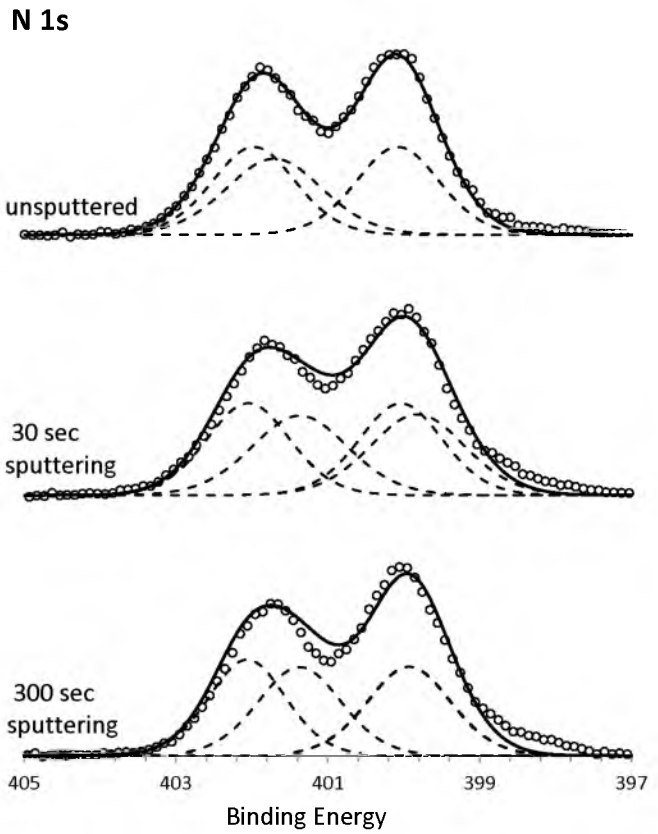

Figure B.5 N 1s high resolution XPS of [MAT]I before and after sputtering.

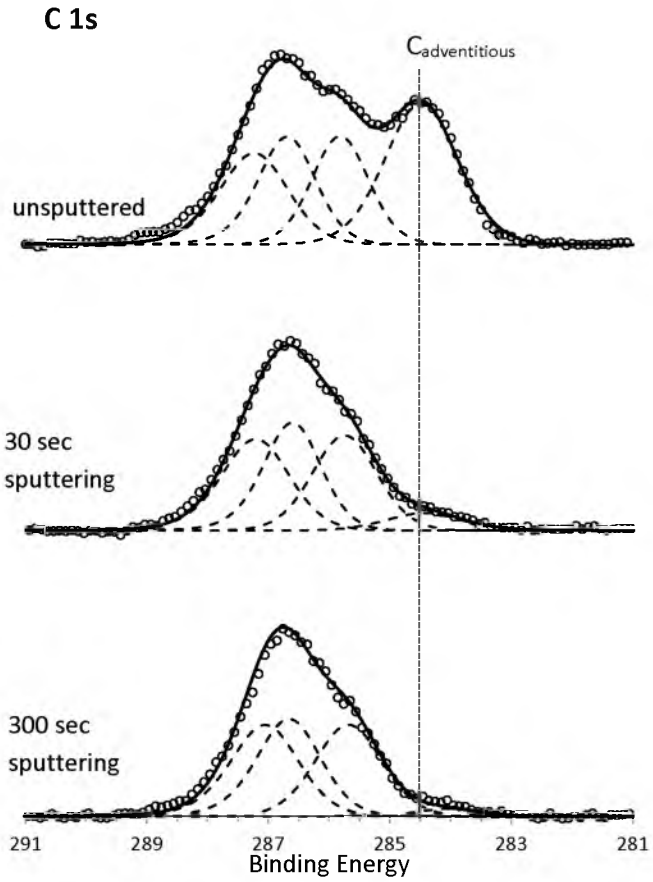

Figure B.6 C 1s high resolution XPS of [MAT]I before and after sputtering.

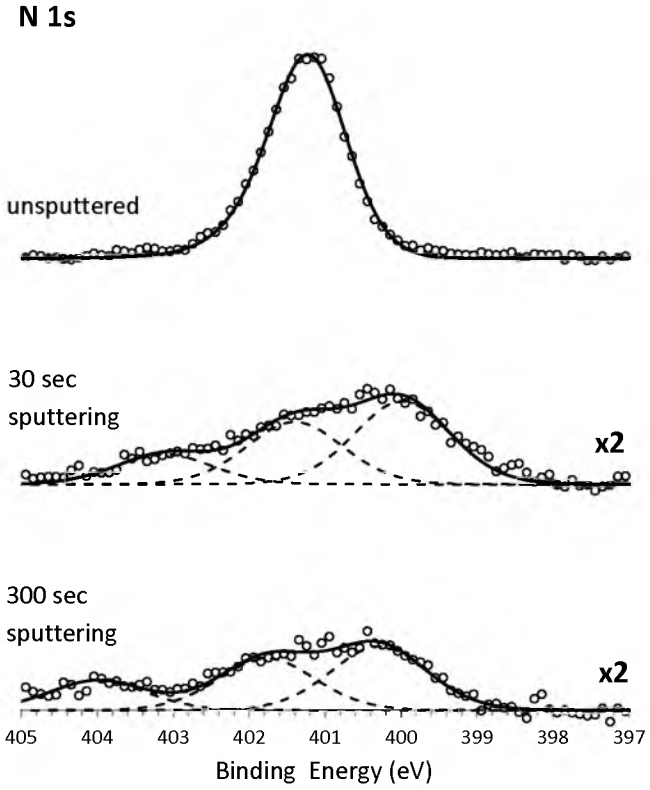

Figure B.7 N 1s high resolution XPS of [BMIM]Cl before and after sputtering.

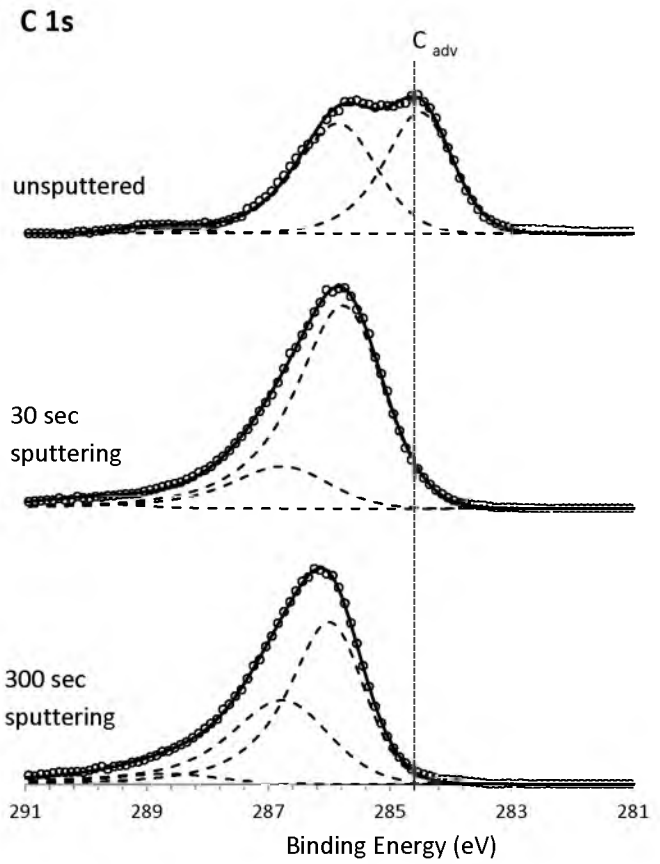

Figure B.8 C 1s high resolution XPS of [BMIM]Cl before and after sputtering.

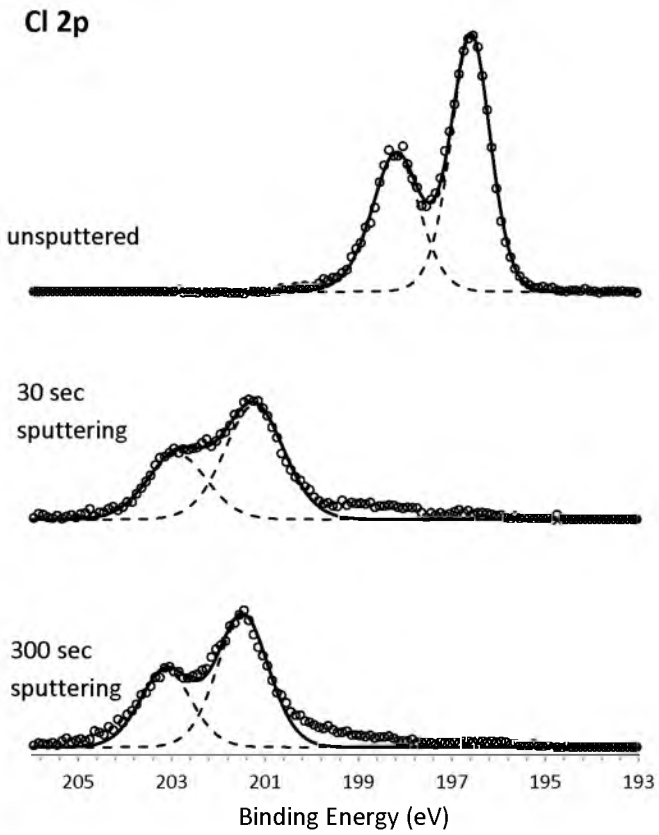

Figure B.9 [BMIM]Cl Cl 2p region scan showing effect of sputtering on surface.

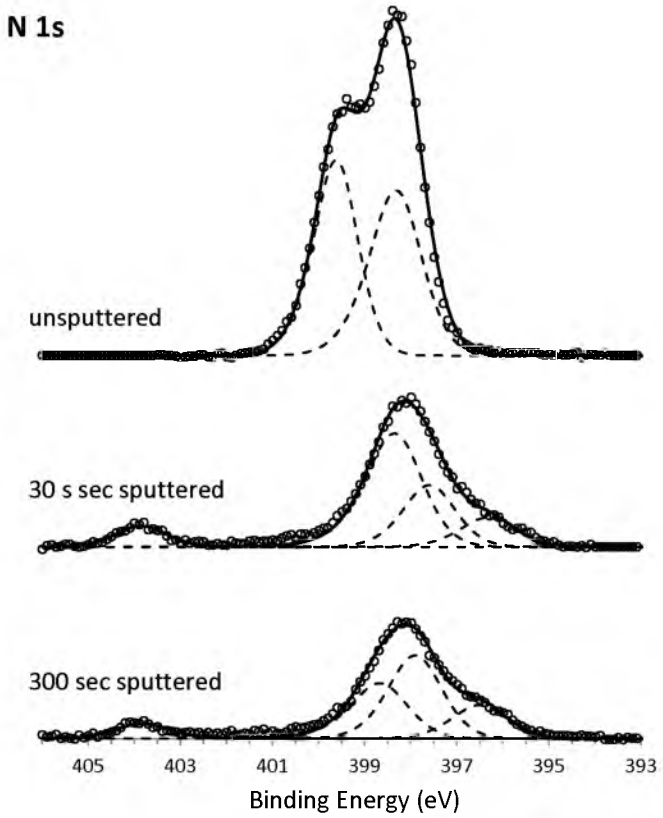

Figure B.10 N 1s high resolution XPS of Na[DCA] before and after sputtering. A noticeable shift in N 1s binding energy was observed after just 30 s of sputtering with Ar^+.

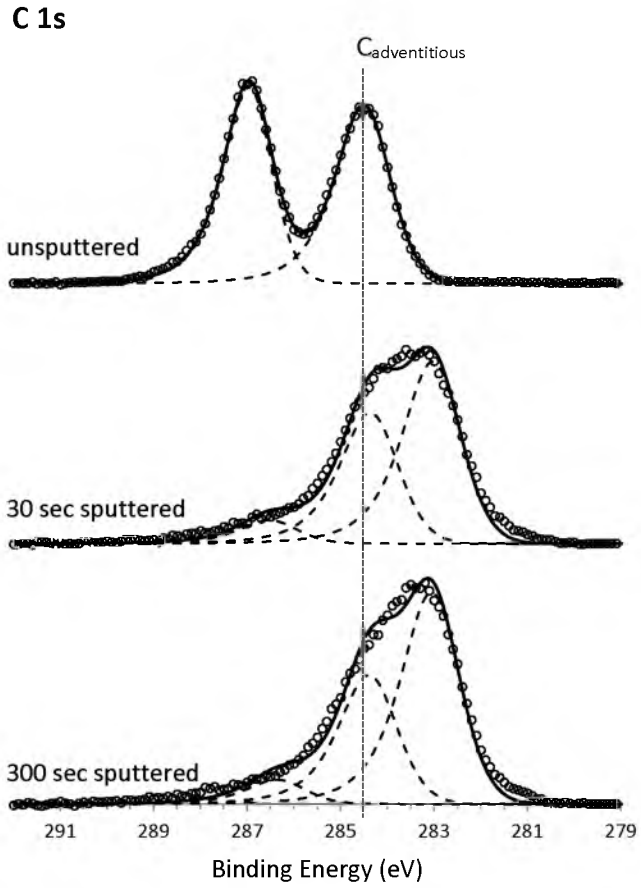

Figure B.11 C 1s high resolution XPS of Na[DCA] before and after sputtering. A noticeable shift in C 1s binding energy was observed after just 30 s of sputtering with Ar^+.

most cases, the effects are modest, apart from a significant decrease in the adventitious carbon peak in the C 1s spectra. For Na [DCA] and [BMIM]Cl, however, there are major changes in the spectra attributed to sputter-induced decomposition, as discussed in the main manuscript.

B.2 "Post-Milling IL-Capping" Experiments: Passivating Boron Nanoparticles After Milling

For these experiments, boron powder was milled with no capping agent, only acetonitrile as a dispersing agent to facilitate size reduction during milling was used. The particles were washed out of the milling jar using additional acetonitrile, collected by centrifugation, washed with ethanol, then vacuum dried. One portion of the boron powder was simply set aside as an uncapped control sample. Two other portions were mixed with either [MAT][DCA] or [BMIM][DCA], and ultrasonicated for 2 hours. Finally, the IL-capped particles were prepared for XPS analysis by the same repeated ultrasonic ethanol washing/centrifugation process that was used to generate the samples in Figure 3.5 in Chapter 3. The two IL-capped samples, together with the uncapped control sample were then removed from the nitrogen glove box, and air dried overnight before XPS analysis.

The B 1s XPS data (Figure B.12) show that the uncapped control sample oxidized extensively upon air exposure, very similar to the uncapped sample that was prepared in the course of the experiments reported in Figure 3.5 of the main manuscript. The two samples that were ultrasonicated with ILs show substantially less oxidation, indicating that the post-milling IL-capping procedure does result in formation of washing-resistant IL capping layers. Comparison with Figure 3.5 does show that the protection against air oxidation is not as good for the postmilling IL-capped samples as for the samples capped

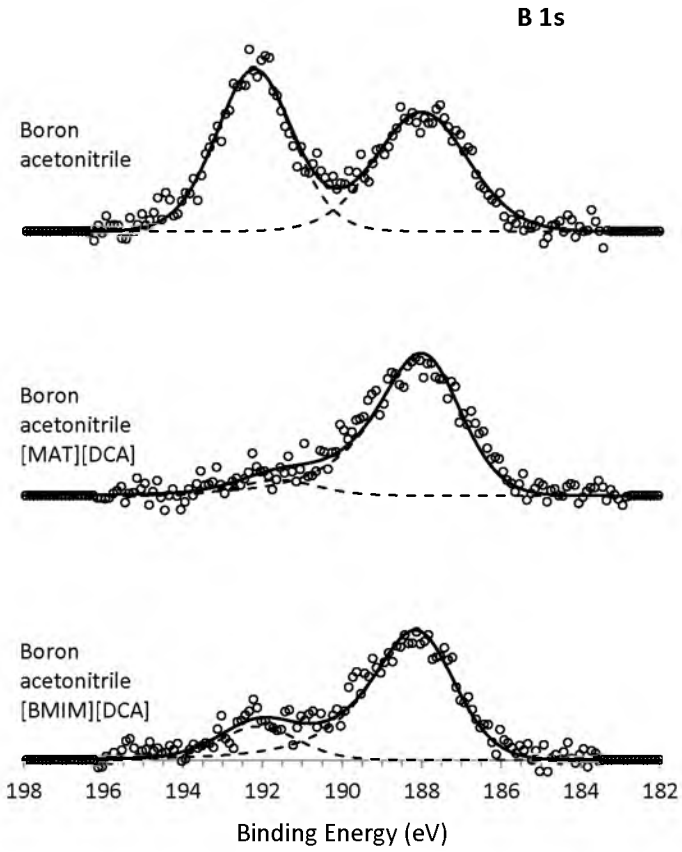

Figure B.12 High resolution B 1s XPS scan on boron milled in acetonitrile and reacted with [MAT][DCA] and [BMIM][DCA] ILs.

in the milling process. This difference might indicate better capping under milling conditions, but it may simply reflect the fact that the postmilling IL-capped samples have hours of exposure to the glove box atmosphere, and we cannot exclude oxidation by some contaminant. Clearly one advantage to combining milling and capping operations is that the surfaces are capped as they are formed.

Figure B.13 compares the N 1s XPS for the three samples from the postmilling IL-capping experiments. As with the samples prepared by milling with the ILs (Figure 3.6), the N 1s spectra are broad and featureless, and because there is little information to be gained from them, we did not analyze these further.

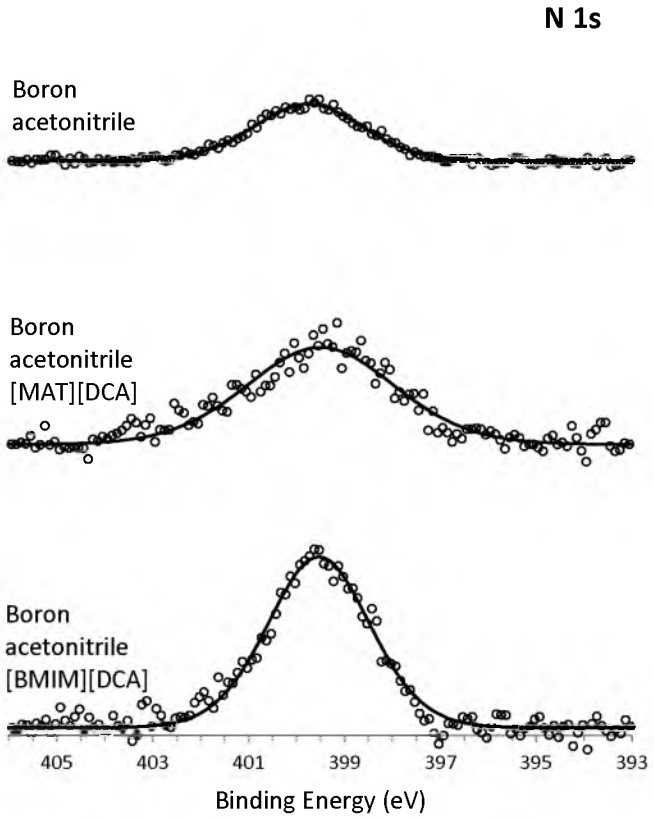

Figure B.13 High resolution N 1s XPS scan of boron milled in acetonitrile and then reacted with [MAT][DCA] and [BMIM][DCA] ILs.

B.3 XPS Evidence of Very Different IL Layer Thicknesses for [MAT][DCA] and [BMIM][DCA].

As discussed in the main manuscript, there are a number of pieces of information indicating that the thickness of the IL layer that remains on the boron particle surfaces is quite different for the two ILs examined here. Figure B.14 shows XPS survey spectra of boron nanoparticles functionalized with [MAT][DCA] and [BMIM][DCA] after they were washed ultrasonically three times with ethanol. Significant amounts of IL remain on the nanoparticles as can be deduced from the intense N 1s peaks in both spectra. Comparison of the spectra shows that there is ca. 10 times less B 1s and ca. 3 times more N 1s signal for [MAT][DCA] than for [BMIM][DCA]. Both changes are consistent with the [MAT][DCA] capping layer being substantially thicker than that for [BMIM][DCA], resulting in lower B

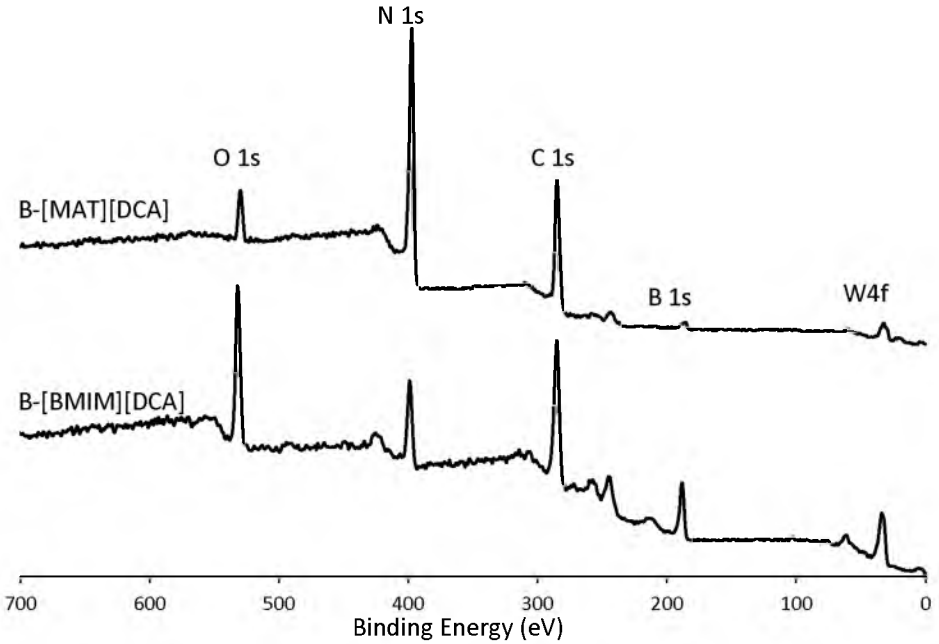

Figure B.14 XPS survey spectra of boron milled with [MAT][DCA] and [BMIM][DCA].

1s signal due to attention of those electrons in the thicker IL layer, and more N 1s signal because more of the nitrogen-containing IL is retained.

One point worth noting is the presence of significant O 1s peaks in Figure B.14. One source of oxygen signal might be boron oxide formed as the samples were air dried, however, if this were true, then oxidized boron would be also obvious in the high resolution B 1s spectra (Figure 3.5, main manuscript). In fact, the roughly 4-to-1 ratio of O 1s to B 1s intensity in Figure B.14, when corrected for the roughly 5 to 1 relative detection sensitivity, would imply that the corresponding B 1s spectra (Figure 3.5, spectra c and f) should be dominated by peaks for oxidized boron. Instead, there is virtually no oxidized boron signal for the IL-capped samples, in contrast to the spectrum for unprotected boron (Figure 3.5a) where there is indeed a large peak for B^{3+} at 193 eV.

Because the O 1s signals in Figure B.14 are clearly not associated with boron oxide formation, we attribute them to the presence of adventitious adsorbates, which tend to

contaminate any sample exposed to laboratory air, as these were during drying and transfer to the XPS instrument. Such adsorbates might include O_2 physisorbed in or on the IL capping layer, but it is also likely that the adventitious organic adsorbates (see Figures B.2, B.4, B.6, B.8, B.11) include species with some oxygen content.

B.4 Comparison of C 1s Spectra for Neat ILs and ILs Bound to Boron Surfaces

The main manuscript shows the effects on the N 1s spectra of the [MAT][DCA] and [BMIM][DCA] ILs from binding to the boron surface. Figure B.15 shows the analogous effects on the C 1s spectra. Because the C 1s spectra are less structured to begin with, it is not possible to interpret the spectral shifts with any confidence, beyond noting that binding to boron clearly results in broadening of the features.

B.5 XPS Probing of the Stability of ILs Under Milling Conditions

One point of interest is the extent to which these ILs tend to decompose under milling conditions. Obviously the IL molecules that are actually bound to the boron surfaces must undergo significant chemical changes, as shown in the XPS and IR data in Figures 3.6 and 3.8 of the main manuscript. In addition, however, it is possible that the milling process might lead to substantial decomposition of the free IL molecules. To test this possibility, Figure B.16 compares the N 1s spectra for the neat IL starting materials, with those for ILs recovered after milling. As discussed in the main manuscript, boron samples were prepared for XPS analysis by repeated ultrasonic washing and centrifugation in ethanol, in order to remove excess IL from the boron surfaces. The recovered ILs examined in Figure B.16 were obtained by simply allowing the ethanol used in the washing process to evaporate.

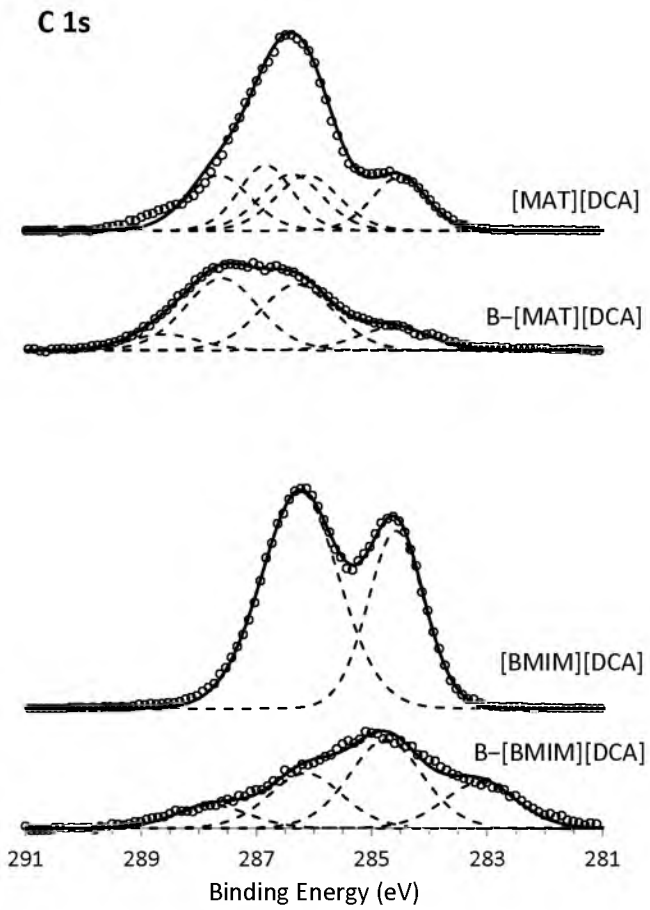

Figure B.15 C 1s XPS region scan of boron milled with [MAT][DCA] and [BMIM][DCA].

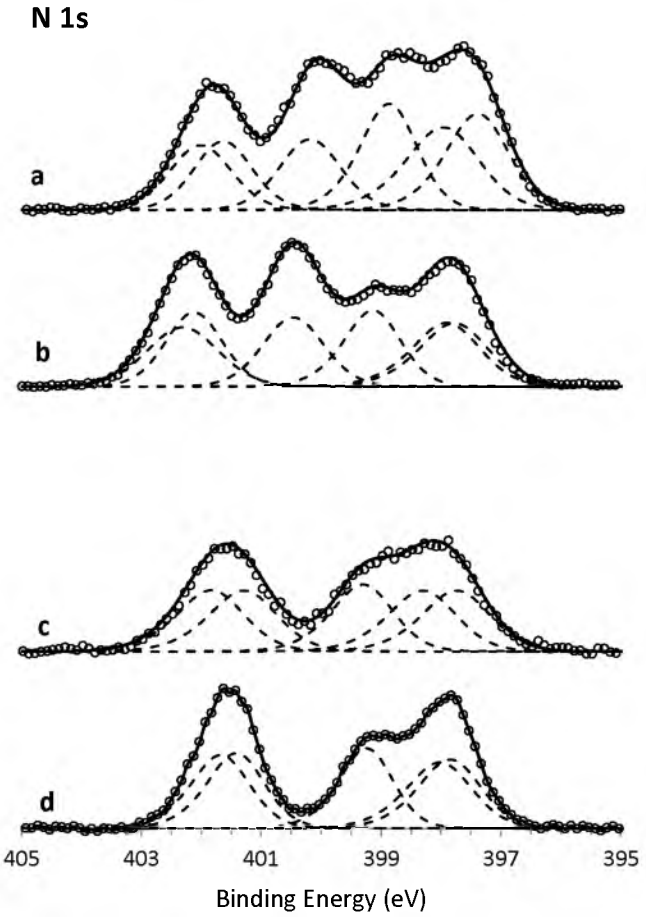

Figure B.16 N 1s survey spectra of **(a.)** [MAT][DCA] recovered from washed boron nanoparticles milled with [MAT][DCA], **(b.)** neat [MAT][DCA], **(c.)** [BMIM][DCA] recovered from washed boron nanoparticles milled with [BMIM][DCA], and **(d.)** neat [BMIM][DCA].

It can be seen that the spectra for the recovered ILs are similar to those for the starting materials, with the exception that there is additional broad signal at low binding energies, approximately centered about 399 eV. This additional signal might be taken as evidence of substantial IL decomposition, however, we note that the ILs recovered from the washings still contain some boron, as shown in spectra d and g of Figure 3.5, presumably reflecting the presence of very small boron particles that remained in suspension during centrifugation. As shown in Figure 3.6, the N 1s spectra of ILs bound to boron consist of broad features in just the low binding energy region where the additional signal is noted in the N 1s spectra for the recovered ILs. We conclude, therefore, that aside from some ILs that are bound to small boron particles, the ILs recovered after milling are essentially unchanged from the starting materials.

B.6 TGA Measurements

The main manuscript presents TGA data for the two ILs and for the IL capping layers on boron particles. Here, we present additional TGA data for some of the reference salts, which help identify which components of the ILs are responsible for the initial low temperature mass losses. Figure B.17 shows that the initial decomposition for [MAT][DCA] occurs at similar temperature to that for [MAT]I, suggesting that decomposition of the $[MAT]^+$ cation is responsible for the initial mass loss for [MAT][DCA]. Figure B.18 shows similar data for [BMIM][DCA] and [BMIM]Cl, and again suggests that decomposition of the cation is probably responsible for the initial mass loss in the [BMIM][DCA] IL.

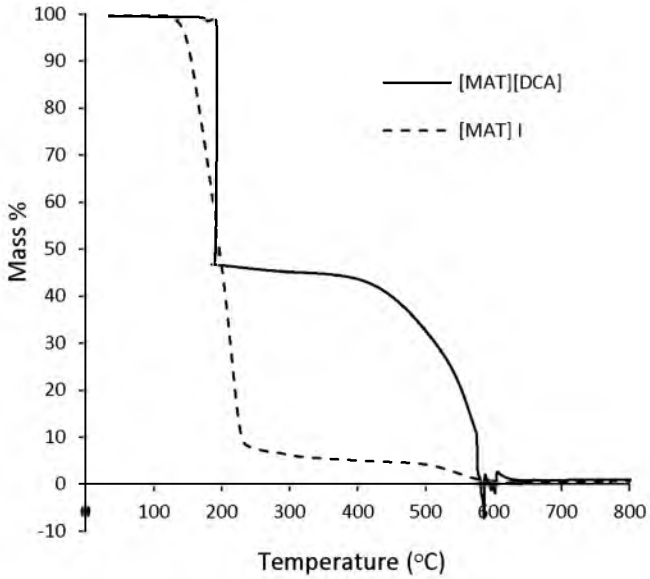

Figure B.17 TGA plot of [MAT][DCA] compared to [MAT]I.

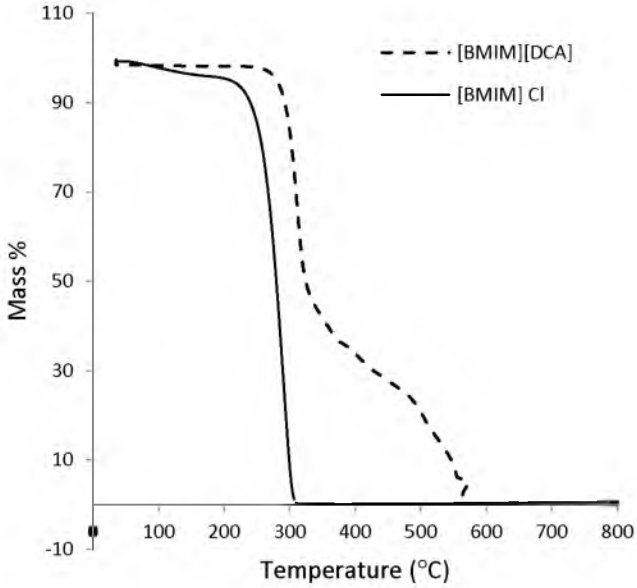

Figure B.18 TGA plot of [BMIM][DCA] compared to [BMIM]Cl.

B.7 Estimation of Solvent-Resistant IL Layer Thickness

XPS, IR, and TGA data all indicate that the thickness of the [MAT][DCA] layer left on the boron surface after thorough ethanol washing is greater than that for [BMIM][DCA]. With some reasonable assumptions, we can use the mass losses during TGA analysis to put limits on the thickness of these solvent-resistant layers. The assumptions used in the estimations are as follows. We assume that the particles have uniform size equal to the peak size in the distributions measured by DLS for each sample (30 ± 10 nm for [BMIM][DCA, 60 ± 20 nm for [MAT][DCA]). Furthermore, since we have no detailed shape information, we assume that the particles are spherical, i.e., have the minimum surface area/mass ratios. We also make use of the measurement that the thickness of the self-limiting oxide layer that forms on boron in air is 0.5 nm.[1]

The primary results from the TGA (Figure 3.10b) for this purpose are the initial mass losses that occur up to ~430°C, which is the temperature where large mass gains signal the onset of oxidation of the boron *bulk*. There may be oxidation of the boron surface layer at lower temperatures, but only bulk oxidation can result in the observed mass gains of 23% and 54%. The fact that this bulk oxidation has a sharp temperature dependence suggests that the self-limiting surface oxide is reasonably stable at lower temperature, presumably because diffusion is too slow to enable significant bulk oxidation. In this regard, it is interesting to note that the melting point of boron oxide is 450°C,[2] suggesting that the self-limiting oxide layer is stable to almost the bulk oxide melting point.

It is useful to consider several different assumptions about how boron begins to oxidize as the IL layer is lost.

B.7.1. Assumption I: Assume that there is no boron oxidation as the IL layer is decomposed up to 430°C. This assumption is not realistic, because we expect the boron

surface to form a self-limiting oxide layer as the IL layer is lost. Nevertheless, this assumption is interesting because it represents a lower limit on the amount of IL present in the samples. In this limiting case, the mass lost up to 430°C is just the mass of the IL layer, and given the assumption of spherical particles with known average size, we can convert the observed percent mass loss ("%mass IL") to the absolute IL mass loss as follows:

In Case 1 we assume that the observed mass loss up to 430 °C corresponds to the total IL mass that was initially on the boron (%mass loss = % IL contribution to the initial total mass).

For [BMIM][DCA] coated boron nanoparticles.

$$\text{Mass of boron/particle (fg)} = \left(\frac{4}{3}\pi r^3\right) \times \left(\rho_{\text{Boron}}\right)$$

$$= \left[\frac{4}{3}\,\pi\,(1.5 \times 10^{-6}\ \text{cm})^3\right] \times (2.34\ \text{g/cm}^3)$$

$$= 3.3 \times 10^{-17}\ \text{g}$$

$$= 0.033\ \text{fg}$$

$$\text{Error calculation} = \frac{4\pi\rho_B}{3} \times 3 \cdot dr \cdot (r)^2$$

$$= 3.3 \times 10^{-17}\ \text{g}$$

$$= 0.033\ \text{fg}$$

$$= \mathbf{0.033 \pm 0.033\ fg}$$

$$\text{Mass of IL/particle (fg)} = \left(\frac{\text{mass of B per particle}}{\text{mass \% B}}\right) \text{\% mass loss}$$

$$= \left(\frac{0.033\ \text{fg}}{95\ \%}\right) 5\ \%$$

$$= 0.0017\ \text{fg}$$

$$\text{Error calculation} = 0.0017 \times \sqrt{\left(\frac{0.033}{0.033}\right)^2 + \left(\frac{1}{5}\right)^2 + \left(\frac{1}{95}\right)^2}$$

$= 0.0017$ fg

$= \mathbf{0.0017 \pm 0.0017\ fg}$

$$\text{Mass of IL per nm}^2\text{ (fg)} = \frac{\text{mass of IL/particle}}{4\pi r^2}$$

$$= \frac{0.0017\text{ fg}}{4\pi(15\text{ nm})^2}$$

$= 6.0 \times 10^{-7}$ fg/nm^2

$$\text{Error calculation} = (6.0 \times 10^{-7}) \times \sqrt{\left(\frac{0.0017}{0.0017}\right)^2 + \left(\frac{2{\cdot}5(4\pi{\cdot}15\text{ nm})}{4\pi(15\text{ nm})^2}\right)^2}$$

$= 7.2 \times 10^{-7}$ fg/nm^2

$= \mathbf{(6.2 \pm 7.2) \times 10^{-7}\ fg/nm^2}$

Having determined the lower limit on the mass of IL/nm^2 initially, it is trivial to convert this to an estimate of the number of IL ion pairs/nm^2

$$\text{No. of IL ion pair/nm}^2 = \frac{\left(\text{mass of IL per particle (g)} \Big/ \text{FW IL (g/mol)}\right) \times N_A}{4\pi r^2}$$

$$= \frac{\left(1.7 \times 10^{-18}\text{ g} \Big/ 205.26\text{ g/mol}\right) \times 6.02 \times 10^{23}\text{ IL ion pairs/mol}}{4\pi(15\text{ nm})^2}$$

$= 1.8$ [BMIM][DCA] ion pairs/nm^2

$$\text{Error calculation} = 1.8 \times \sqrt{\left(\frac{0.0017}{0.0017}\right)^2 + \left(\frac{2{\cdot}5(4\pi{\cdot}15\text{ nm})}{4\pi(15\text{ nm})^2}\right)^2}$$

$= 2.1$ [BMIM][DCA] ion pairs/nm^2

$= \mathbf{1.8 \pm 2.1\ [BMIM][DCA]\ ion\ pairs\ /nm^2}$

To go from this lower limit on ion pair surface coverage, to the thickness of the IL layer, we need to know the footprint of the IL ion pairs on the surface. It seems reasonable to

assume that the layer is close packed because it is clearly dense enough to prevent O_2 oxidation of the boron surface. One limit would be if the $[BMIM]^+$ and $[DCA]^-$ both lie flat on the surface, but it is also possible that the IL binds standing on edge or in many other geometries. The area covered by each molecule is estimated by multiplying the length and the width of the ion pairs when they are positioned side by side, using molecular geometries from the *ab initio* calculations and an estimate of the van der Waals radii to determine the separation. The footprint per ion pair is thereby estimated to be ~0.71 nm^2 in the limit of lying flat on the surface, dropping to something more like 0.13 nm^2/ion pair, if the IL binds with the cation and anion both perpendicular to the surface (Figure B.19).

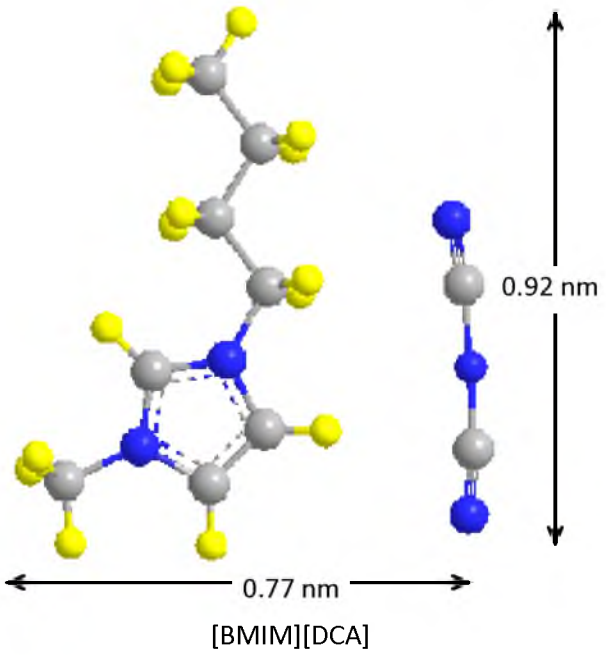

Figure B.19 Chemical structure of [BMIM][DCA] showing dimensions of a single ionic liquid ion pair.

Area of a single [BMIM][DCA] ion pair

1 monolayer (ML) coverage

Parallel to surface = 0.92 nm × 0.77 nm

= 0.71 nm^2

Perpendicular to surface

= 0.17 nm × 0.77 nm

= 0.13 nm^2

We can therefore estimate the number of IL monolayers in this limiting case as somewhere between 1.3 ML (lying flat), and 0.23 ML if binding perpendicularly:

Monolayer Coverage = (area covered by a single ion pair) × (no of ion pair/nm^2)

IL parallel to the surface = (0.71 nm^2/ion pair) × (1.8 ion pair/nm^2)

= 1.3 monolayer

Error calculation = 0.71 × 2.1

= 1.5 monolayers

IL perpendicular to the surface = (0.13 nm^2/ion pair) × (1.8 ion pair/nm^2)

= 0.24 monolayer

Error calculation = 0.13 × 2.1

= 0.27 monolayers

For [MAT][DCA] coated boron nanoparticles, using the same assumptions

$$\text{Mass of boron/particle (fg)} = \left(\frac{4}{3}\pi r^3\right) \times \left(\rho_{Boron}\right)$$

$$= \left[\frac{4}{3}\,\pi\left(3.0 \times 10^{-6}\ \text{cm}\right)^3\right] \times \left(2.34\ \text{g/cm}^3\right)$$

$$= 2.6 \times 10^{-16}\ \text{g}$$

$= 0.26$ fg

Error calculation $= \frac{4\pi\rho_B}{3} \times 3 \cdot dr \cdot (r)^2$

$= 0.26$ fg

$= \mathbf{0.26 \pm 0.26\ fg}$

Mass of IL/particle (fg) $= \left(\frac{\text{mass of B per particle}}{\%\ \text{mass B}}\right) \%$ mass loss

$= \left(\frac{0.26\ \text{fg}}{86\ \%}\right) \times 14\ \%$

$= 0.042$ fg

Error calculation $= 0.042 \times \sqrt{\left(\frac{0.26}{0.26}\right)^2 + \left(\frac{1}{14}\right)^2 + \left(\frac{1}{86}\right)^2}$

$= 0.042$ fg

$= \mathbf{0.042 \pm 0.042\ fg}$

Mass of IL/nm^2 (fg) $= \frac{\text{mass of IL/particle}}{4\pi r^2}$

$= \frac{0.042\ \text{fg}}{4\pi(30\ \text{nm})^2}$

$= 3.7 \times 10^{-6}$ fg/nm^2

Error calculation $= (3.7 \times 10^{-6}) \times \sqrt{\left(\frac{0.043}{0.043}\right)^2 + \left(\frac{2 \cdot 10(4\pi \cdot 30\ \text{nm})}{4\pi(30\ \text{nm})^2}\right)^2}$

$= 4.4 \times 10^{-6}$ fg/nm^2

$= \mathbf{(3.7 \pm 4.4) \times 10^{-6}\ fg/nm^2}$

No. of IL ion pair/nm^2 $= \frac{\left(\text{mass of IL per particle (g)} \,/\, \text{FW IL (g/mol)}\right) \times N_A}{4\pi r^2}$

$= \frac{\left(4.2 \times 10^{-17}\ \text{g} \,/\, 165.46\ \text{g/mol}\right) \times (6.02 \times 10^{23}\ \text{IL ion pairs/mol})}{4\ \pi\ (30\ \text{nm})^2}$

$= 14$ [MAT][DCA] ion pairs/nm^2

$$\text{Error calculation} = 14 \times \sqrt{\left(\frac{0.043}{0.043}\right)^2 + \left(\frac{2 \cdot 10(4\pi \cdot 30\ \text{nm})}{4\pi(30\ \text{nm})^2}\right)^2}$$

$= 17$ [BMIM][DCA] ion pairs/nm^2

$= 14 \pm 17$ [MAT][DCA] ion pairs /nm^2

Area of a single [MAT][DCA] ion pair (Figure B.20)

1 monolayer (ML) coverage

Parallel to surface = 0.60 nm × 0.70 nm

$= 0.42$ nm^2

Perpendicular to surface

$= 0.17$ nm × 0.70 nm

$= 0.12$ nm^2

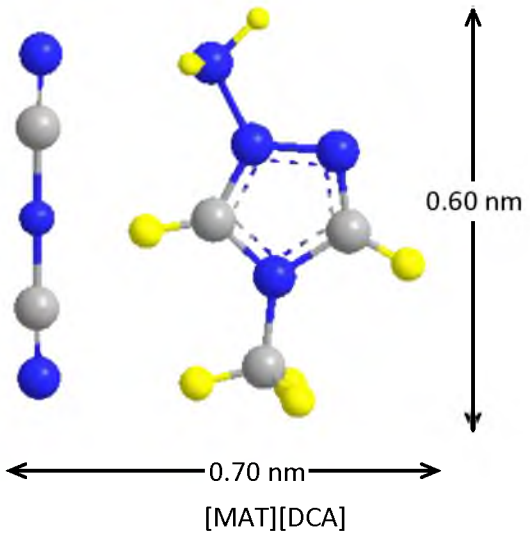

Figure B.20 Chemical structure of [MAT][DCA] showing dimensions of a single ionic liquid ion pair.

Monolayer Coverage = (area covered by a single ion pair) × (no of ion pair/nm^2)

IL parallel to the surface = (0.42 nm^2/ion pair) × (14 ion pair/nm^2)

= 5.9 ML

Error calculation = 0.42 × 17

= 7.1 monolayers

IL perpendicular to the surface = (0.12 nm^2/ion pair) × (14 ion pair/nm^2)

= 1.7 ML

Error calculation = 0.12 × 17

= 2.0 monolayers

Note that in this limiting case, where boron was assumed to remain unoxidized as the IL is removed, the IL mass per unit area is about 6.2 times greater for [MAT][DCA], than for [BMIM][DCA].

For case 2 we assume that the ILs on the particle surface decompose in the same manner as the free, uncoordinated IL (Figures B.15 and B.16). Hence, the mass loss observed up to 430 °C corresponds only to that fraction of the IL that decomposes below this temperature, taken from the TGA results for the neat ILs. In this scenario, we still assume that there is no boron oxidation below 430 °C. The analysis in this case is exactly the same as in Case 1, above, except that the IL mass loss is equated to the fraction of IL decomposed (70% for [BMIM][DCA], 60% for [MAT][DCA]), rather than to the total IL mass. The calculations are summarized.

For [BMIM][DCA] coated boron nanoparticles: particle diameter = 30 nm (15 nm radius)

Mass of B/particle (fg) = $\left(\frac{4}{3}\pi r^3\right) \times \left(\rho_{Boron}\right)$

$$= \left[\frac{4}{3}\pi\left(1.5 \times 10^{-6}\ \text{cm}\right)^3\right] \times (2.34\ \text{g/cm}^3)$$

$$= 3.3 \times 10^{-17}\ \text{g}$$

$$= 0.033\ \text{fg}$$

$$\text{Error calculation} = \frac{4\pi\rho_B}{3} \times 3 \cdot dr \cdot (r)^2$$

$$= 0.033\ \text{fg}$$

$$= \mathbf{0.033 \pm 0.033\ fg}$$

$$\%\ \text{mass total IL} = \left(\frac{\%\ \text{mass loss of B-[BMIM][DCA] sample at 450 °C}}{\%\ \text{mass loss of neat [BMIM][DCA] at 450 °C}}\right) \times 100\%$$

$$= \left(\frac{5\ \%}{70\ \%}\right) \times 100\%$$

$$= 7.1\ \%$$

$$\text{Error calculation} = 7.1\% \times \sqrt{\left(\frac{1}{5}\right)^2 + \left(\frac{1}{70}\right)^2}$$

$$= 1.4\ \%$$

$$= \mathbf{7.1 \pm 1.4\ \%}$$

$$\text{Mass of IL/particle (fg)} = \left(\frac{\text{mass of B per particle}}{\text{mass \% B}}\right) \%\ \text{mass total IL}$$

$$= \left(\frac{0.033\ \text{fg}}{92.9\ \%}\right) 7.1\ \%$$

$$= 0.0025\ \text{fg}$$

$$\text{Error calculation} = 0.0025 \times \sqrt{\left(\frac{0.033}{0.033}\right)^2 + \left(\frac{1.4}{92.9}\right)^2 + \left(\frac{1.4}{7.1}\right)^2}$$

$$= 0.0013\ \text{fg}$$

$$= \mathbf{0.0025 \pm 0.0025\ fg}$$

$$\text{Mass of IL/nm}^2\ (\text{fg/nm}^2) = \frac{\text{mass of IL/particle}}{4\pi r^2}$$

$$= \frac{0.0025 \text{ fg}}{4\pi(15 \text{ nm})^2}$$

$$= 8.8 \times 10^{-7} \text{ fg/nm}^2$$

$$\text{Error calculation} = (8.8 \times 10^{-7}) \times \sqrt{\left(\frac{0.0025}{0.0025}\right)^2 + \left(\frac{2 \cdot 5(4\pi \cdot 15 \text{ nm})}{4\pi(15 \text{ nm})^2}\right)^2}$$

$$= 1.1 \text{ x } 10^{-6} \text{ fg/nm}^2$$

$$= \mathbf{(8.8 \pm 11) \text{ x } 10^{-7} \text{ fg/nm}^2}$$

$$\text{No. of IL ion pair/nm}^2 = \frac{\left(\text{mass of IL per particle (g)} / \text{FW IL (g/mol)}\right) \times N_A}{4\pi r^2}$$

$$= \frac{\left(2.5 \times 10^{-18} \text{ g} / 205.26 \text{ g/mol}\right) \times (6.02 \times 10^{23} \text{ IL ion pairs/mol})}{4\pi(15 \text{ nm})^2}$$

$$= 2.6 \text{ [BMIM][DCA] ion pairs/nm}^2$$

$$\text{Error calculation} = 2.6 \times \sqrt{\left(\frac{0.0025}{0.0025}\right)^2 + \left(\frac{2 \cdot 5(4\pi \cdot 15 \text{ nm})}{4\pi(15 \text{ nm})^2}\right)^2}$$

$$= 3.1 \text{ [BMIM][DCA] ion pairs/nm}^2$$

$$\mathbf{= 2.6 \pm 3.1 \text{ [BMIM][DCA] ion pairs /nm}^2}$$

$$\text{Monolayer Coverage (ML)} = (\text{area covered by a single ion pair}) \times (\text{no. of ion pair/nm}^2)$$

$$\text{IL parallel to the surface} = (0.71 \text{ nm}^2/\text{ion pair}) \times (2.6 \text{ ion pair/nm}^2)$$

$$= 1.8 \text{ ML}$$

$$\text{Error calculation} = 0.71 \times 3.1$$

$$\mathbf{= 2.2 \text{ monolayers}}$$

$$\text{IL perpendicular to the surface} = (0.13 \text{ nm}^2/\text{ion pair}) \times (2.6 \text{ ion pair/nm}^2)$$

$$= 0.34 \text{ ML}$$

$$\text{Error calculation} = 0.13 \times 3.1$$

= 0.40 monolayers

Note that the mass of [BMIM][DCA]/nm^2 and the corresponding number of ion pairs/nm^2 are ~50% greater than when we assumed that all the IL was lost below 430 °C.

For [MAT][DCA] coated boron nanoparticles: particle diameter = 60 ± 20 nm (30 nm radius)

Mass of B/particle (fg) $= \left(\frac{4}{3}\pi r^3\right) \times \left(\rho_{Boron}\right)$

$= \left[\frac{4}{3}\pi\left(3.0 \times 10^{-6}\ cm\right)^3\right] \times (2.34\ g/cm^3)$

$= 2.6 \times 10^{-16}$ g

$= 0.26$ fg

Error calculation $= \frac{4\pi\rho_B}{3} \times 3 \cdot dr \cdot (r)^2$

$= 2.6 \times 10^{-16}$ g

$= 0.26$ fg

= 0.26 ± 0.26 fg

% mass total IL $= \left(\frac{\text{\% mass loss of B-[MAT][DCA] sample at 450 °C}}{\text{\% mass loss of neat [MAT][DCA] at 450 °C}}\right) \times 100\ \%$

$= \left(\frac{14\ \%}{60\ \%}\right) \times 100\ \%$

$= 23\ \%$

Error calculation $= 23\ \% \times \sqrt{\left(\frac{1}{14}\right)^2 + \left(\frac{1}{60}\right)^2}$

$= 1.7\ \%$

= 23.3 ± 1.7 %

Mass of IL/particle (fg) $= \left(\frac{\text{mass of B per particle}}{\text{mass \% B}}\right)$ % mass total IL

$$= \left(\frac{0.26 \text{ fg}}{76.7\ \%}\right) 23.3\ \%$$

$$= 0.079 \text{ fg}$$

$$\text{Error calculation} = 0.079 \times \sqrt{\left(\frac{0.26}{0.26}\right)^2 + \left(\frac{1.7}{76.7}\right)^2 + \left(\frac{1.7}{23.3}\right)^2}$$

$$= 0.079 \text{ fg}$$

$$= \mathbf{0.079 \pm 0.079\ fg}$$

$$\text{Mass of IL/nm}^2 \text{ (fg/nm}^2) = \frac{\text{mass of IL/particle}}{4\pi r^2}$$

$$= \frac{0.079 \text{ fg}}{4\pi(30 \text{ nm})^2}$$

$$= 7.0 \times 10^{-6} \text{ fg/nm}^2$$

$$\text{Error calculation} = (7.0 \times 10^{-6}) \times \sqrt{\left(\frac{0.081}{0.081}\right)^2 + \left(\frac{2 \cdot 10(4\pi \cdot 30 \text{ nm})}{4\pi(30 \text{ nm})^2}\right)^2}$$

$$= 8.4 \text{ x } 10^{-6} \text{ fg/nm}^2$$

$$= \mathbf{(7.1 \pm 8.4) \text{ x } 10^{-6}\ fg/nm^2}$$

$$\text{No. of IL ion pair/nm}^2 = \frac{\left(\text{mass of IL per particle (g)} \Big/ \text{FW IL (g/mol)}\right) \times N_A}{4\pi r^2}$$

$$= \frac{\left(7.9 \text{ x } 10^{-17} \text{ g} \Big/ 165.46 \text{ g/mol}\right) \times 6.02 \times 10^{23} \text{ IL ion pairs/mol}}{4\pi(30 \text{ nm})^2}$$

$$= 25 \text{ [MAT][DCA] ion pairs/nm}^2$$

$$\text{Error calculation} = 25 \times \sqrt{\left(\frac{0.081}{0.081}\right)^2 + \left(\frac{2 \cdot 5(4\pi \cdot 15 \text{ nm})}{4\pi(15 \text{ nm})^2}\right)^2}$$

$$= 31 \text{ [BMIM][DCA] ion pairs/nm}^2$$

$$= \mathbf{25 \pm 31\ [BMIM][DCA]\ ion\ pairs/nm^2}$$

$$\text{Monolayer Coverage (ML)} = \text{(area covered by a single ion pair)} \times \text{(no of ion pair/nm}^2)$$

IL parallel to the surface = (0.42 nm^2/ion pair) × (25 ion pair/nm^2)

= 11 ML

Error calculation = 0.42 × 31

= 13 monolayers

IL perpendicular to the surface = (0.12 nm^2/ion pair) × (25 ion pair/nm^2)

= 3.0 ML

Error calculation = 0.12 × 31

= 3.7 monolayers

Note that for [MAT][DCA], the increase in estimated mass or number of IL ion pairs/nm^2 is ~85% greater than when all the IL was assumed to have decomposed below 430 °C.

B.7.2 Assumption II: Assume that boron oxidizes to form a self-limiting oxide layer as the IL is leaving the surface. We believe this to be a much more realistic assumption than that discussed above, given boron's high oxygen affinity. We assume here that the initial oxide layer is self-limiting, preventing bulk oxidation up to 430 °C. Furthermore, we assume that thickness of this layer is identical to what forms on boron in air at room temperature (0.5 nm^1), because we have no way of measuring this thickness independently. As the IL decomposes, the mass loss from this process is offset by the mass gain due to oxygen incorporation into the surface layer. Given the assumption that the self-limiting oxide layer is indeed stable up to 430°C, we should obtain upper limits on the amount of IL initially present in the capping layer on the boron surface. Because we are looking for upper limits, we show the calculation only for the case where the fraction of IL lost up to 430°C is assumed to be the same for IL on boron, as for neat IL (i.e., Case 2 above). Other than including the mass of the oxide layer, the calculations are identical to those above.

Assume mass loss by 430 °C = fraction of mass loss by neat ILs by 430 °C;

$$\% \text{ mass IL} = \left(\frac{\% \text{ mass loss of B-[BMIM][DCA] sample at 430 °C}}{\% \text{ mass loss of neat [BMIM][DCA] at 430 °C}}\right) \times 100\%$$

For [BMIM][DCA] coated boron nanoparticles: particle diameter = 30 nm (15 nm radius)

Mass of B_2O_3 formed/particle (fg) = (volume of B_2O_3 in particle)× (B_2O_3 mass density)

= (total volume of particle − volume of boron core) × (B_2O_3 mass density)

$$= \left\{\frac{4}{3}\pi[(r+t)^3 - r^3]\right\} \times \left(\rho_{B_2O_3}\right)$$

where r = radius of the boron core, and

t = thickness of the boron oxide layer, 0.5 nm[1]

$$= \left\{\frac{4}{3}\pi\left[(1.5\times10^{-6}\text{ cm} + 0.05\times10^{-6}\text{ cm})^3 - (1.5\times10^{-6}\text{ cm})^3\right]\right\} \times (2.46\text{ g/cm}^3)$$

$$= 3.6 \times 10^{-18}\text{ g}$$

$$= 0.0036\text{ fg}$$

$$\text{Error calculation} = 3.6 \times 10^{-18}\text{ g} \sqrt{\left(\frac{3\cdot d(r+t)\cdot(r+t)^2}{(r+t)^3}\right)^2 + \left(\frac{3\cdot dr\cdot r^2}{r^3}\right)^2}$$

$$= 5.0 \times 10^{-17}\text{ g}$$

$$= 0.005\text{ fg}$$

$$\text{Mass of O gained/particle (fg)} = \text{mass } B_2O_3 \times \left(\frac{3\text{ FW O}}{\text{FW } B_2O_3}\right)$$

$$= 0.0036\text{ fg} \times \left(\frac{3\ (15.999\text{ g/mol})}{69.618\text{ g/mol}}\right)$$

$$= 0.0025\text{ fg}$$

$$\text{Error calculation} = 0.005\text{ fg} \times \left(\frac{3\ (15.999\text{ g/mol})}{69.618\text{ g/mol}}\right)$$

$$= 0.0034\text{ fg}$$

$$= \mathbf{0.0025 \pm 0.0034\text{ fg}}$$

$$\text{Mass of B/particle (fg)} = \left(\frac{4}{3}\pi r^3\right) \times \left(\rho_{\text{Boron}}\right)$$

$$= \left[\frac{4}{3}\pi(1.5 \times 10^{-6}\ \text{cm})^3\right] \times (2.34\ \text{g/cm}^3)$$

$$= 3.3 \times 10^{-17}\ \text{g}$$

$$= 0.033\ \text{fg}$$

$$\text{Error calculation} = \frac{4\pi\rho_B}{3} \times 3 \cdot dr \cdot (r)^2$$

$$= 0.033\ \text{fg}$$

$$= \mathbf{0.033 \pm 0.033\ fg}$$

$$\%\ \text{mass IL} = \left(\frac{\%\ \text{mass loss of B-[BMIM][DCA] sample at 450 °C}}{\%\ \text{mass loss of neat [BMIM][DCA] at 450 °C}}\right) \times 100\%$$

$$= \left(\frac{5\ \%}{70\ \%}\right) \times 100\ \%$$

$$= 7.1\ \%$$

$$\text{Error calculation} = 7.1\% \times \sqrt{\left(\frac{1}{5}\right)^2 + \left(\frac{1}{70}\right)^2}$$

$$= 1.4\%$$

$$= \mathbf{7.1 \pm 1.4\ \%}$$

$$\text{Mass of IL/particle (fg)} = \left(\frac{\text{mass of B per particle}}{\text{mass \% B}}\right) \%\ \text{mass IL}$$

$$= \left(\frac{0.033\ \text{fg}}{92.9\ \%}\right) 7.1\ \%$$

$$= 0.0025\ \text{fg}$$

$$\text{Error calculation} = 0.0025 \times \sqrt{\left(\frac{0.033}{0.033}\right)^2 + \left(\frac{1.4}{7.1}\right)^2 + \left(\frac{1.4}{92.9}\right)^2}$$

$$= 0.0025\ \text{fg}$$

$$= \mathbf{0.0025 \pm 0.0025\ fg}$$

Total Mass of IL/particle (fg) = mass O gained + mass IL from TGA mass loss

$= 0.0025 \text{ fg} + 0.0025 \text{ fg}$

$= 0.0050 \text{ fg}$

Error calculation $= \sqrt{(0.0034)^2+(0.0025)^2}$

$= 0.0042 \text{ fg}$

$= \mathbf{0.0050 \pm 0.0042 \text{ fg}}$

$$\text{Mass of IL/nm}^2 \text{ (fg/nm}^2) = \frac{\text{Total mass of IL/particle}}{4\pi r^2}$$

$$= \frac{0.0050 \text{ fg}}{4\pi(15 \text{ nm})^2}$$

$= 1.8 \times 10^{-6} \text{ fg/nm}^2$

$$\text{Error calculation} = (1.8\times10^{-6}) \times \sqrt{\left(\frac{0.0042}{0.0050}\right)^2 + \left(\frac{2\cdot5(4\pi\cdot15 \text{ nm})}{4\pi(15 \text{ nm})^2}\right)^2}$$

$= 1.8 \text{ x } 10^{-6} \text{ fg/nm}^2$

$= \mathbf{(1.8 \pm 1.8) \text{ x } 10^{-6} \text{ fg/nm}^2}$

$$\text{No. of IL ion pair/nm}^2 = \frac{\left(\text{total mass of IL per particle (g)} \Big/ \text{FW IL (g/mol)}\right) \times N_A}{4\pi r^2}$$

$$= \frac{\left(5.0 \text{ x } 10^{-18} \text{ g} \Big/ 205.26 \text{ g/mol}\right) \times 6.02 \times 10^{23} \text{ IL ion pairs/mol}}{4\pi(15 \text{ nm})^2}$$

$= 5.2$ [BMIM][DCA] ion pairs/nm^2

$$\text{Error calculation} = 5.2 \times \sqrt{\left(\frac{0.0042}{0.0050}\right)^2 + \left(\frac{2\cdot5(4\pi\cdot15 \text{ nm})}{4\pi(15 \text{ nm})^2}\right)^2}$$

$= 5.6$ [BMIM][DCA] ion pairs/nm^2

$= \mathbf{5.2 \pm 5.6}$ **[BMIM][DCA] ion pairs/nm^2**

Monolayer Coverage = (area covered by a single ion pair) × (no of ion pair/nm^2)

IL parallel to the surface = (0.71 nm^2/ion pair) × (5.2 ion pair/nm^2)

= 3.7 ML

Error calculation = 0.71 × 5.6

= 4.0 monolayers

IL perpendicular to the surface = (0.13 nm^2/ion pair) × (5.2 ion pair/nm^2)

= 0.68 ML

Error calculation = 0.13 × 5.6

= 0.73 monolayers

It can be seen that our estimated upper limit on the IL mass or number of ion pairs per nm^2 is only about 2.5 times greater than the lower limit estimate (Assumption I, Case 1).

For [MAT][DCA] coated boron nanoparticles: particle diameter = 60±20 nm (30±10 nm radius)

Mass of B_2O_3 formed/particle (fg) = (volume of B_2O_3 in particle) × (B_2O_3 mass density)

= (total volume of particle − volume of boron core) × (B_2O_3 mass density)

$$= \left\{\frac{4}{3}\pi[(r+t)^3 - r^3]\right\} \times \left(\rho_{B_2O_3}\right)$$

where r = radius of the boron core, and

t = thickness of the boron oxide layer, 0.5 nm[1]

$$= \left\{\frac{4}{3}\pi\left[(3.0\times10^{-6}\ \text{cm} + 0.05\times10^{-6}\ \text{cm})^3 - (3.0\times10^{-6}\ \text{cm})^3\right]\right\} \times (2.46\ \text{g/cm}^3)$$

$$= 1.4 \times 10^{-17}\ \text{g}$$

= 0.014 fg

$$\text{Error calculation} = 1.4\times10^{-17}\ \text{g} \sqrt{\left(\frac{3\cdot d(r+t)\cdot(r+t)^2}{(r+t)^3}\right)^2 + \left(\frac{3\cdot dr\cdot r^2}{r^3}\right)^2}$$

$$= 2.0 \times 10^{-17}\ \text{g}$$

= 0.02 fg

$= 0.014 \pm 0.020$ fg

Mass of O gained/particle (fg) $= \text{mass } B_2O_3 \times \left(\frac{3 \text{ FW O}}{\text{FW } B_2O_3}\right)$

$= 0.014 \text{ fg} \times \left(\frac{3\ (15.999 \text{ g/mol})}{69.618 \text{ g/mol}}\right)$

$= 0.0097$ fg

Error calculation $= 0.020 \text{ fg} \times \left(\frac{3\ (15.999 \text{ g/mol})}{69.618 \text{ g/mol}}\right)$

$= 0.013$ fg

$= \mathbf{0.0097 \pm 0.013\ fg}$

Mass of B/particle (fg) $= \left(\frac{4}{3}\pi r^3\right) \times \left(\rho_{Boron}\right)$

$= \left[\frac{4}{3}\pi(3.0 \times 10^{-6} \text{ cm})^3\right] \times (2.34 \text{ g/cm}^3)$

$= 2.6 \times 10^{-16}$ g

$= 0.26$ fg

Error calculation $= \frac{4\pi\rho_B}{3} \times 3 \cdot dr \cdot (r)^2$

$= 0.26$ fg

$= \mathbf{0.26 \pm 0.26\ fg}$

% mass IL $= \left(\frac{\text{\% mass loss of B-[MAT][DCA] sample at 450 °C}}{\text{\% mass loss of neat [MAT][DCA] at 450 °C}}\right) \times 100\%$

$= \left(\frac{14\ \%}{60\ \%}\right) \times 100\ \%$

$= 23.3\ \%$

Error calculation $= 23.3\% \times \sqrt{\left(\frac{1}{14}\right)^2 + \left(\frac{1}{60}\right)^2}$

$= 1.7\%$

$= \mathbf{7.1 \pm 1.7\ \%}$

Mass of IL/particle from TGA mass loss data (fg) =

$$\left(\frac{\text{mass of B per particle}}{\text{mass \% B}}\right) \%\ \text{mass loss}$$

$$= \left(\frac{0.26\ \text{fg}}{76.7\ \%}\right) 23.3\ \%$$

$$= 0.081\ \text{fg}$$

$$\text{Error calculation} = 0.081\ \text{fg} \times \sqrt{\left(\frac{0.26}{0.26}\right)^2 + \left(\frac{1.7}{23.3}\right)^2 + \left(\frac{1.7}{76.7}\right)^2}$$

$$= 0.081\ \text{fg}$$

$$= \mathbf{0.081 \pm 0.081\ fg}$$

Total Mass of IL/particle (fg) = mass O gained + mass IL from TGA mass loss

$$= 0.0097\ \text{fg} + 0.081\ \text{fg}$$

$$= 0.091\ \text{fg}$$

$$\text{Error calculation} = \sqrt{(0.013)^2 + (0.081)^2}$$

$$= 0.082\ \text{fg}$$

$$= \mathbf{0.091 \pm 0.082\ fg}$$

$$\text{Mass of IL/nm}^2\ (\text{fg/nm}^2) = \frac{\text{total mass of IL/particle (fg)}}{4\pi r^2}$$

$$= \frac{0.091\ \text{fg}}{4\pi(30\ \text{nm})^2}$$

$$= 8.0 \times 10^{-6}\ \text{fg/nm}^2$$

$$\text{Error calculation} = (8.0 \times 10^{-6}) \times \sqrt{\left(\frac{0.082}{0.091}\right)^2 + \left(\frac{2 \cdot 5(4\pi \cdot 15\ \text{nm})}{4\pi(15\ \text{nm})^2}\right)^2}$$

$$= 9.0 \times 10^{-6}\ \text{fg/nm}^2$$

= **(8.0 ± 9.0) x 10^{-6} fg/nm^2**

$$\text{No. of IL ion pair/nm}^2 = \frac{\left(\text{total mass of IL per particle(g)} \Big/ \text{FW IL(g/mol)}\right) \times N_A}{4\pi r^2}$$

$$= \frac{\left(9.1 \times 10^{-17}\ \text{g} \Big/ 165.46\ \text{g/mol}\right) \times (6.02 \times 10^{23}\ \text{IL ion pairs/mol})}{4\pi(30\ \text{nm})^2}$$

= 29 [MAT][DCA] ion pairs/nm^2

$$\text{Error calculation} = 29 \times \sqrt{\left(\frac{0.082}{0.091}\right)^2 + \left(\frac{2 \cdot 5(4\pi \cdot 15\ \text{nm})}{4\pi(15\ \text{nm})^2}\right)^2}$$

= 33 [MAT][DCA] ion pairs/nm^2

= **29 ± 33 [MAT][DCA] ion pairs/nm^2**

Monolayer Coverage = (area covered by a single ion pair) × (no of ion pair/nm^2)

IL parallel to the surface = (0.42 nm^2/ion pair) × (29 ion pair/nm^2)

= 12 ML

Error calculation = 0.42 × 33

= 14 monolayers

IL perpendicular to the surface = (0.12 nm^2/ion pair) × (29 ion pair/nm^2)

= 3.5 ML

Error calculation = 0.12 × 33

= 4.0 monolayers

It can be seen that our estimated upper limit on the IL mass or number of ion pairs per nm^2 is only about 2 times greater than the lower limit estimate (Assumption I, Case 1).

B.8 References

(1) Van Devener, B.; Perez, J. P. L.; Jankovich, J.; Anderson, S. L. Oxide-Free, Catalyst-Coated, Fuel-Soluble, Air-Stable Boron Nanopowder as Combined Combustion Catalyst and High Energy Density Fuel. *Energy Fuels* **2009,** *23*, 6111-6120.

(2) Weast, R. C.; Astle, M., J.; Beyer, W. H. *Crc Handbook of Chemistry and Physics*. 66 ed.; CRC Press: Boca Raton, 1985.

APPENDIX C

ADDITIONAL DATA FOR CHAPTER 4

C.1 Considerations Regarding Boron Surface Sites as a Function of Particle Size

The 5 wt% boron loading calculated from the measured 40 psi H_2 pressure drop during milling yields a B:H atom ratio of ~1.8:1, i.e., more than one H atom for every two boron atoms in the sample. In boranes, stoichiometries vary from 1:3 for diborane, to 1:1.4 for decaborane.[1] The larger boranes tend to be cage-like, with a single H atom per B atom, except at edges, where there can be two H/B. Therefore, it seems reasonable to assume that boron atoms on the surface of boron nanoparticles might accommodate one H atom. In that case, 1.8:1 B:H ratio implies that ~56 % of the boron atoms are bonded to H.

If we further assume that only B atoms on the surface bind H, then 56% of the B atoms are on the surface. As shown in Figure 4.4 the boron particles have a large size distribution and are rough, but because boron is difficult to image in TEM, we cannot quantitatively characterize the particles in such detail. Here, we estimate the size that would be required to give 56 % surface atoms if the particles were uniform spheres, with density equal to the density of bulk amorphous boron (2.37 g/cm^3),[2] equivalent to 132 B atoms/nm^3. If we consider the particles as spheres with a 1-atom thick surface layer, where H can bind, surrounding a core of pure boron, and further assume atomic layer thickness of ~0.19 nm, also estimated from the bulk density, then the total number of boron atoms, and number in the surface layer, are easily calculated. Figure C.1 shows the percent of the boron atoms in the particle that are in the surface layer, as a function of the particle diameter. Figure C.1 plots the percentage of boron atoms on the surface of a particle as the diameter decreases, and it can be seen that for spherical particles, the diameter would need to be ~2 nm to account for the fraction of boron in the surface layer. Of course, in reality, the particles are larger, but also quite rough. Furthermore, the particles may be able to bind hydrogen interstitially or in internal spaces in the boron bulk.

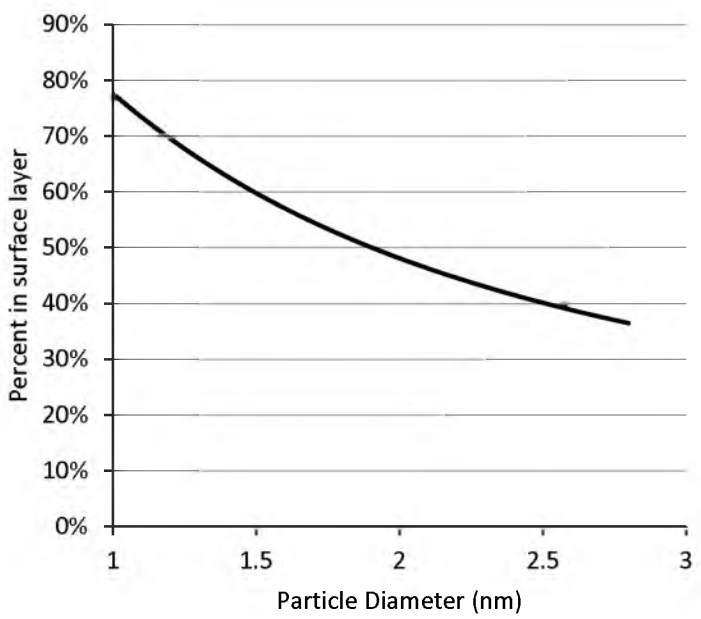

Figure C.1 Plot of the percentage of boron atoms present on the surface as the particle size decreases.

C.2 Sampling depth of XPS

The extent of boron oxidation when samples were exposed to air was tested by X-ray photoelectron spectroscopy (XPS). Figure 4.3 of the main manuscript shows the B 1s region scan of boron nanoparticle samples produced from dry milling in either H_2 or Ar atmospheres. The peak at 188 eV is due to elemental boron in the core of the particles, and the peaks at 193 eV or 192.5 eV are due to oxidized boron on the surface of the samples. The B^{3+}/B^0 ratio is ~4 % for the Ar-milled sample, and is ~20 % in the H_2-milled sample. The effective attenuation length (EAL) for ~190 eV photoelectrons in solid boron is ~3 nm, and the EAL in boron oxide is similar.[3] The probability (P_{detect}) of detecting a photoelectron emitted at depth = z, is given by $P_{detect} = \exp(-z/EAL)$, thus most of the XPS signal comes from the top ~6 nm of the sample.

C.3 **Detection and Removal of Contaminants from Boron Feedstock**

As shown in Figure 4.5 and 4.6 of the paper, milled boron nanoparticles heated under vacuum evolved significant amounts of water and hydrocarbons. To see if these contaminants originated from the boron feedstock, or were somehow introduced in the milling/handling process, we did similar mass spectrometry experiments on the unmilled feedstock. Ninety-five percent purity boron powder is usually obtained from the reduction of B_2O_3 using magnesium metal. Excess magnesium is removed from the reduced boron by dissolving with a strong acid, usually HCl.[4] Figure C.2 displays the mass spectrum of the gases evolved from the feedstock as its temperature was slowly ramped to 400 °C, while continuously leaking the gases into the mass spectrometer, and taking periodic spectra. It can be seen that water, hydrocarbon and other organic compounds are clearly evolved in significant quantities from the feedstock. In addition, signal for H_2^+ is observed, which may include contributions from H_2 evolving from the sample, but also includes contributions from dissociative ionization of water and the hydrocarbons.

One obvious question is whether vacuum heating might be an efficient means to decrease the contaminant level in the feedstock. Figure C.3 compares mass spectra obtained from the same sample at 400 °C during the initial heat ramp (i.e., the final spectrum in Figure C.2), and after heating under vacuum at 400 °C for 12 hours, followed by cooling to room temperature and then heating back to 400 °C. It can be seen that the water and organic ion signals are essentially absent in the spectrum of the degassed sample. Curiously, there is still substantial H_2^+ signal after degassing, raising the possibility that there is some background source of hydrogen in the experiment at high temperature, such as diffusion of hydrogen through the wall of the glass sample tube.

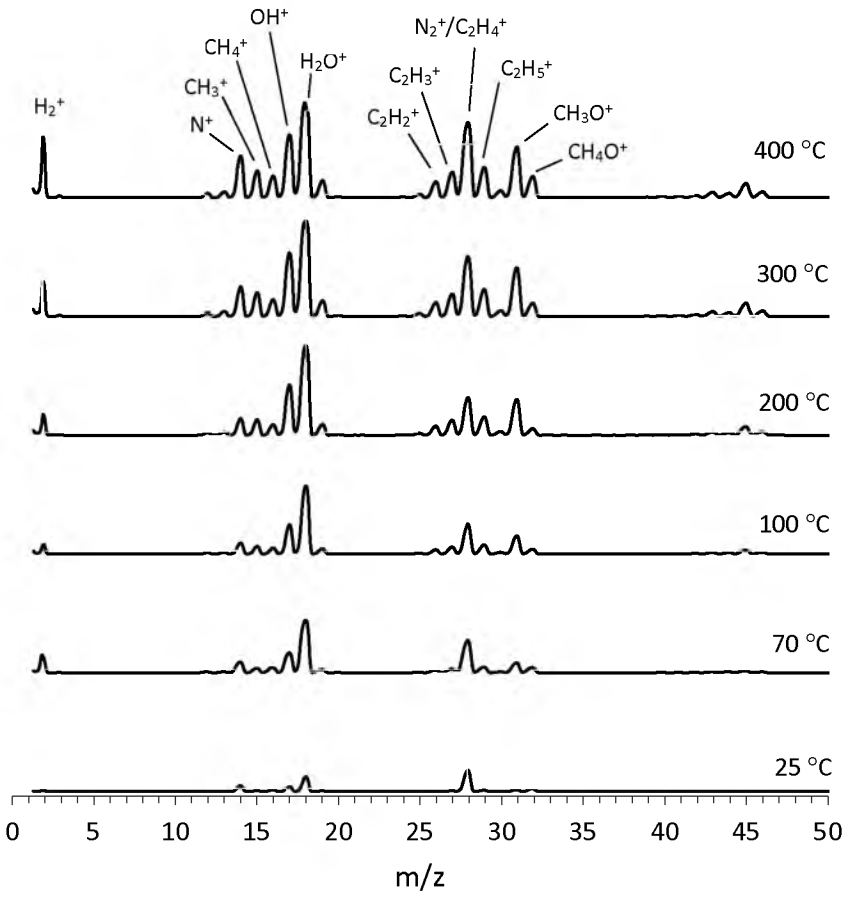

Figure C.2 Mass spectra of evolved gases from boron feedstock heated to 400 °C.

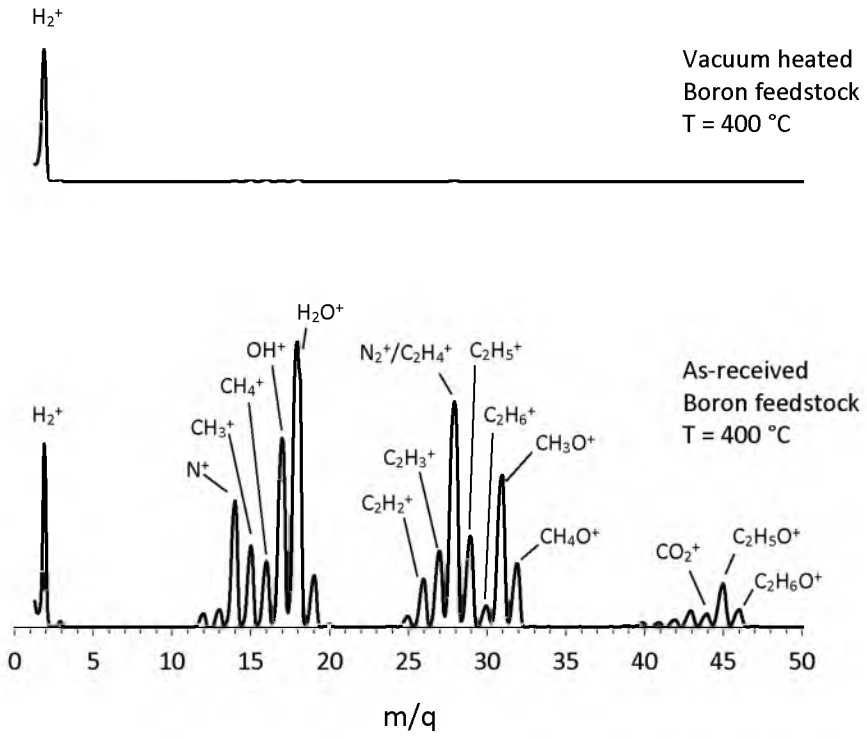

Figure C.3 Mass spectrum of gases evolved from 95 % boron feedstock after cleaning overnight via heating under vacuum (top). Mass spectrum of as received boron 95 % boron feedstock (bottom). Samples were heated at 400 °C to enhance gas desorption.

C.4 References

(1) Linstrom, P. J.; Mallard, W. G. *Nist Chemistry Webbook, Nist Standard Reference Database Number 69*. National Institute of Standards and Technology: Gaithersburg MD, 20899, 2011.

(2) Haynes, W. M. *Crc Handbook of Chemistry and Physics*. 94th ed.; CRC Press Taylor and Francis Group: Boca Raton, FL, 2013.

(3) Powell, C. J.; Jablonski, A. *Nist Electron Effective Attenuation Length Database Version 1.3*. Gaithersburg, MD, 2003.

(4) Markovskii, L. Y. Chemistry of Magnesiothermal Preparation of Boron. *Electron Technol.* **1970,** *3*, 95-102.